Design and Thermal Analysis of a Solar Thermal Thruster

Krishti Das

Technische Universiteit Delft

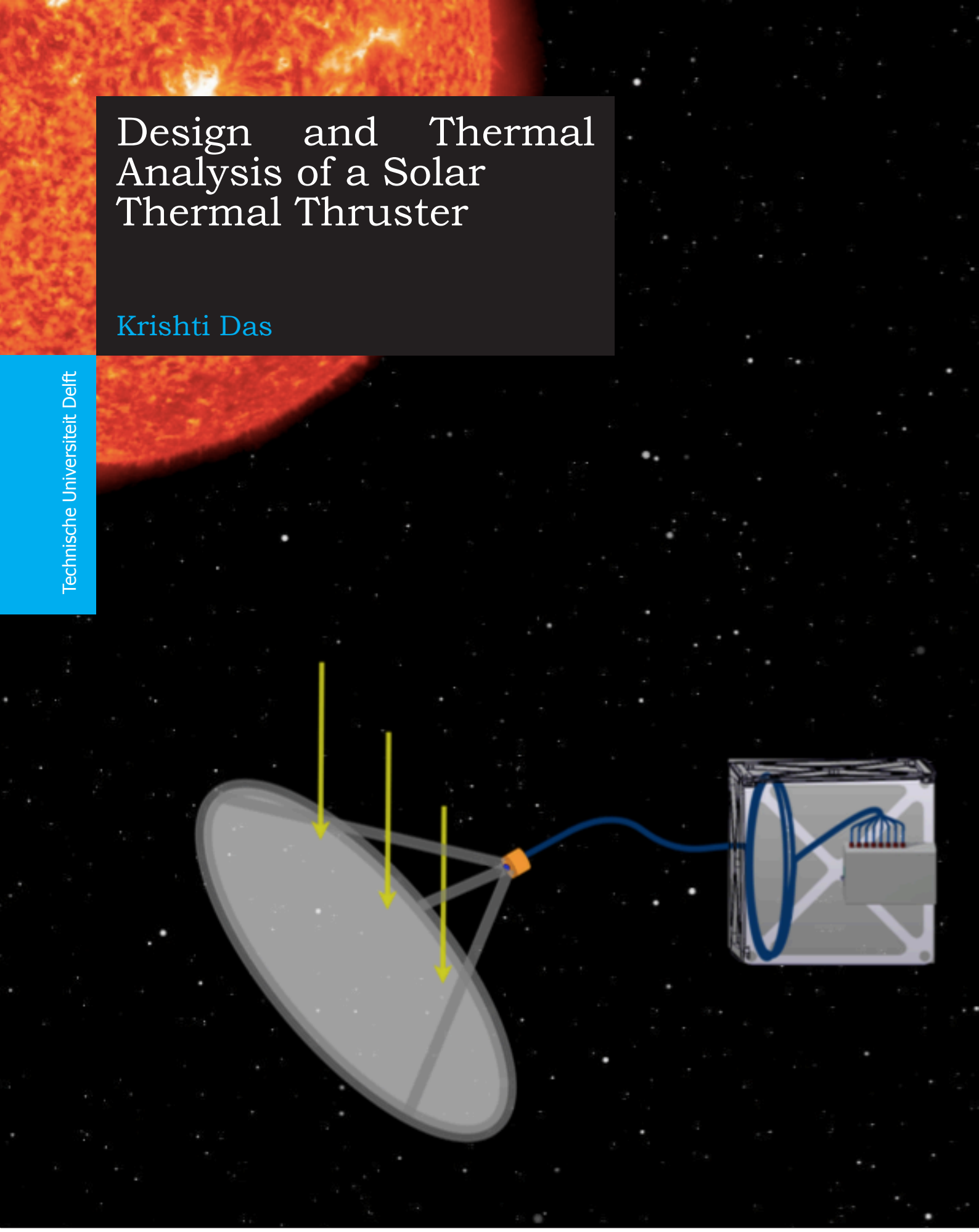

TU Delft Delft University of Technology

Challenge the future

Design and Thermal Analysis of a Solar Thermal Thruster

by

Krishti Das

in partial fulfillment of the requirements for the degree of

Master of Science
in Aerospace Engineering

at the Delft University of Technology,
to be defended publicly on Wednesday 28th of November, 2018 at 9:00 AM

Student number:	4624408	
Supervisor:	Dr. Angelo Cervone	
Daily Supervisor :	Fiona Leverone	
Thesis committee:	Prof. dr. E.K.A Gill,	TU Delft
	Dr. Angelo Cervone,	TU Delft
	Fiona Leverone,	TU Delft
	Dr. M.J Heiligers,	TU Delft

TU Delft Delft University of Technology

Acknowledgement

I would like to start with expressing my deepest gratitude and regard to Dr. Angelo Cervone for his constant guidance, support and answering my silly doubts throughout. At this point, I am genuinely grateful to have had Fiona Leverone as my daily supervisor. She not only supervised me during my thesis and encouraged me to work better but she has helped me become a better researcher. Though I have a long way to go, I have been really fortunate to study at TU Delft and working with professors and students of great caliber.

Last but not least, I would like to thank my mom, dad, and sister who have been my backbone throughout from the other side of the world. I am extremely grateful for the friends I have made during my studies and I would thank Maria, Shreyas, and Amantrita. Their unconditional help and support in my life and studies, in general, has been remarkable. I am also deeply grateful to Stanislaus and Jayraj for their critical and supportive feedback on my work. Finally, I owe it to the boys in the MSc student room, especially Mathijs Van de Poel and Sean Pepper, and to our countless late night conversations about space news and sharing ideas with each other. I would also like to thank Samiksha for her constant encouragement and tea breaks.

Contents

Nomenclature

α	Absorption coefficient of the cavity material
ΔV	Velocity change
$\dot{m}$	Mass flow rate
ϵ	Emissivity of a surface
$\eta_{receiver}$	Receiver efficiency
Γ	Vandenkerckhove constant
γ	Specific heat ratio
μ	Dynamic viscosity at a propellant temperature
ϕ_{solar}	Solar flux at LEO
ρ	Reflectivity Factor
A_2/A_1	Cavity opening area to internal area Ratio
A_e	Nozzle exit area
A_e/A_t	Expansion ratio
A_{throat}, A_t	Throat area of the nozzle
B_{ij}	Gebhart Factor
C	Concentration ratio
C_{ij}	Conductive Coupling
D_t	Throat diameter of the nozzle
e_1	Cavity internal surface emissivity
e_w	Cavity external surface emissivity
F	Thrust
F_{ij}	View Factor
g_0	Gravitational Acceleration
I_{sp}	Specific Impulse
k	Thermal Conductivity
M_p	Propellant Mass
$M_{initial}$	Satellite Wet Mass

P	Power collected
P_c	Chamber pressure
P_e/P_c	Pressure ratio
P_{conc}	Power collected by Concentrator
Q	Incoming solar energy
Q_{prop}	Heat flow to the propellant
Q_{r_1}	Hear lost through re-radiation
Q_{r_2}	Heat lost from the cavity external surface
$Q_{r_{refl}}$	Heat lost by reflection
Q_s	Solar radiation absorbed by the absorber cavity
R	Specific gas constant
R_{ij}	Radiative Coupling
Re_{throat}	Reynolds number at nozzle throat
S_{conc}	Cross-sectional area of the concentrator
T	Temperature
T_1	Internal surface temperature of cavity
T_c	Chamber temperature
T_w	External surface temperature of cavity

Glossary

AFRPL Air Force Rocket Propulsion Laboratory. 4

CSF Conduction Shape Factor. 69

LEO Low Earth Orbit. 1
LUMIO Lunar Meteoroid Impact Observer. 9

MEMS Micro-Electro-Mechanical-Systems. 2

OH Hydroxyl Ion. 52
OW Optical Wave. xiii, xvii, 15, 17

STP Solar Thermal Propulsion. 2
STS Space Transportation System. 5

List of Figures

List of Tables

1

Introduction

Lately, an area of research that has received significant attention is the miniaturization and standardization of satellites. Several articles have pointed out that the trend in satellites is moving towards miniaturization, as it not only offers low production and launch costs but also allows a company/organization to launch multiple small satellites simultaneously. A smaller revisit time and higher coverage as compared to traditional satellites also adds to their advantage. Unlike conventional satellites, micro/small satellites adopt new technologies rapidly, they have an ever-increasing functionality per unit mass, and a larger flexibility and response to new science and its applications [10].

Nano-satellites or CubeSats are a class of satellites that weigh between 1 and 10 kg. These have limited mission capabilities due to their limited micro-propulsion systems. For these systems to be capable of drag compensation, orbit maintenance, formation flying and attitude control, they require a low change in velocity (ΔV) value. In the current scenario, CubeSats are mainly used for communications, space weather research, amateur radio missions and technology demonstrations that are inserted in the low earth orbit (LEO). This thesis aims at broadening the mission capabilities of a CubeSat, while keeping in mind the limitations imposed by a CubeSat itself. Certainly, such satellites require miniaturized space sub-systems and this research will focus on the propulsion subsystem for CubeSats. Besides miniaturization, there is a growing need for clean and safe propulsion systems along with the inclination to reduce the launch and operational costs in the space industry for satellites, especially for small satellites [11].

One way to ensure this is by using a propulsion system that uses a green propellant. Solar thermal propulsion (STP) is a form of space propulsion that utilizes solar energy to heat the propellant which in turn is expanded in a thruster [12]. Previous studies conducted by researchers at the department of Space Systems Engineering at TU Delft, have established that water is a good candidate to be used as a propellant as it is green, and is capable of offering a specific impulse of 372 s at 2500 K [13].

Keeping the above points in mind, it can be established that micro-propulsion systems are needed for micro-satellites and nano-satellites to perform attitude control, formation movements and maintenance, all of which require maneuverability of the satellites. Also, the idea is to broaden the range of applications of a CubeSat for orbital transfer and deep space missions, which is usually constrained due to the lack of strong propulsion systems. These nano-satellites or CubeSats pose several limitations and constraints on the design of a micro-propulsion system such as mass, power,

maximum voltage and volume [14]. STP, along with being a clean and safe propulsion system, is a promising concept that will address these limitations in beneficial ways.

Diving into the production of micro-propulsion systems, microelectromechanical systems (MEMS) manufacturing technology can be adopted for this purpose. MEMS manufacturing technology has been classified as one of the most promising technologies that can be used to fabricate devices or systems that combine electrical and mechanical components [15]. This technology uses integrated circuit processing techniques and produces devices in the range of a few micrometers to millimeters with precision, and these devices have the ability to sense, control and actuate on a micro scale [15]. In regard to the research done in the field of STP thrusters, there is evidence to suggest that several theoretical designs have been developed for small satellites but there is a dearth of information in literature with respect to designs of a MEMS STP thruster. Hence, the objective of this research is to commit to the designing of MEMS solar thermal thruster and investigating its performance for flight on-board a CubeSat.

After a thorough study of existing propulsion systems and possible missions that can benefit from a solar thermal propulsion system, the LUMIO (Lunar Meteoroid Impacts Observer) project has been selected as the candidate for which an STP system will be designed and analyzed. This is a 12U CubeSat mission to the halo orbit at the Earth-Moon Lagrangian point L2 which shall observe, quantify, and characterize meteoroid impacts on the lunar far-side by detecting their impact flashes using optical instruments. (CubeSats are miniaturized satellites that have a dimension of 10cm x 10cm x 10cm per unit, denoted as 1U, and each unit has a mass no more than 1.33 kg [14]).

This thesis begins with a brief background research on previous solar thermal propulsion systems, followed by the system requirement and research framework for the new system being designed, outlined in chapter 2. Chapter 3 discusses three conceptual designs for the heat exchanger and thruster system, and at the conclusion, one of these concepts is selected for further modelling and analysis based on a graphical trade-off. Chapter 4 then deals with the detailed designing of the thruster-receiver system, concentrating system and heat exchanger. This is followed by the thermal modelling and analysis of the heat exchanger and optical system in chapter 5 and then a verification of the thermal model is done before discussing the final results obtained in chapter 6.

2

Research Framework

The solar thermal propulsion system is one that works by concentrating solar energy using a reflector/concentrator that focuses the energy into the receiver cavity, which in turn heats up the propellant. The heated propellant is then expelled through a nozzle, generating thrust. Therefore, as is clear from the mechanism, this system does not require an electric generator for the thrust generation, and the main components of the STP system are the concentrator, a receiver-absorber cavity, a concentrator - receiver interface system (if applicable), a propellant feed system and the thruster. Figure 2.1 shows a schematic diagram of the STP mechanism.

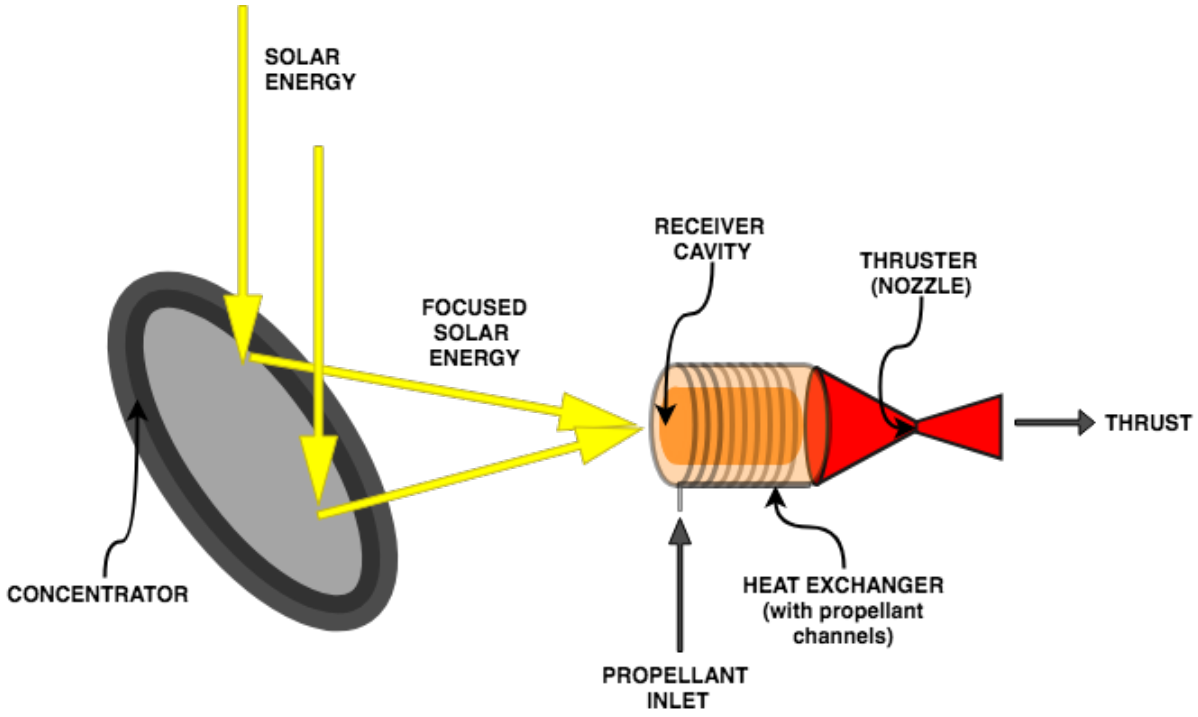

Figure 2.1: Solar thermal propulsion mechanism

2.1. Literature Study

Since its conception 62 years ago in 1956 by Krafft Ehricke, the concept of solar thermal propulsion has been widely researched [16]. This section will throw some light on the position of STP engine

as compared to other propulsion systems in terms of performance as well as its evolution over the years. The performance of the STP system greatly depends on the choice of propellant, as well as the receiver cavity material and its capability to efficiently transfer heat to the propellant. An initial survey on known propulsion systems has been conducted to review where solar thermal propulsion lies in terms of its performance.

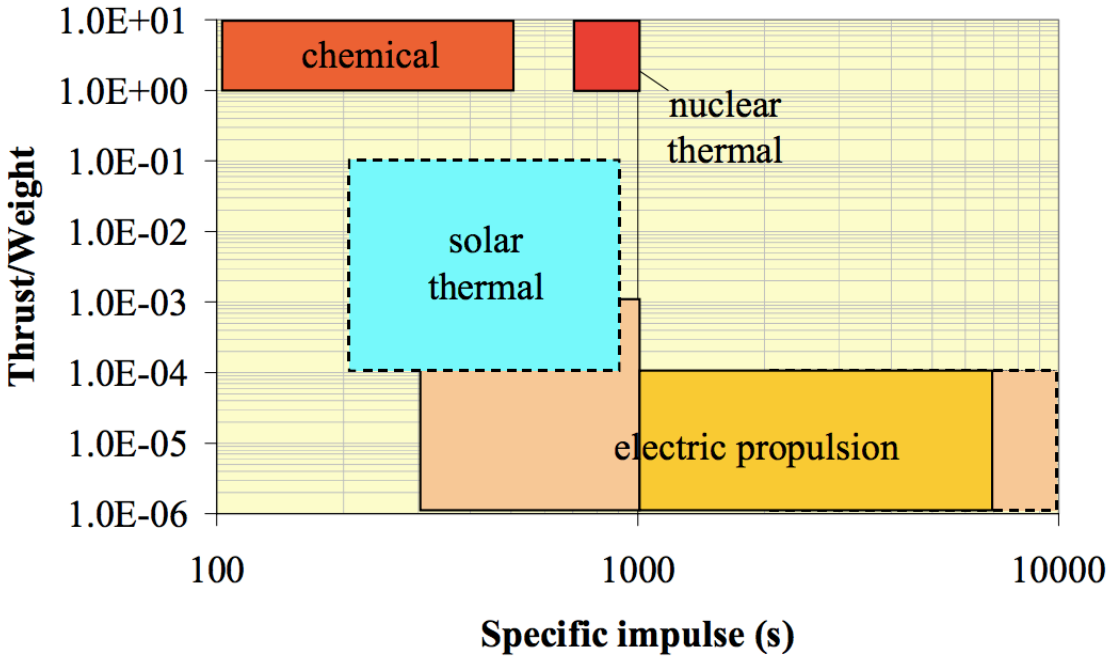

Figure 2.2: Performance of solar thermal propulsion systems vs chemical, electric, and nuclear thermal propulsion options [13].The graph is plotted between thrust/system wet weight and specific impulse.

From the above plot, it can be observed that the STP system lies in between the most commonly used chemical propulsion system and electric propulsion systems. A chemical propulsion system is characterized by a high thrust to weight ratio, which implies that high propellant mass is required for higher thrust, providing low transfer times, and low specific impulse. Whereas, the electric propulsion is identified by high specific impulse and the lowest thrust to weight ratio, which means that the transfer time for a deep space mission would range from several months to years. Based on this comparison graph, the STP system seems to offer an intermediate performance by providing a higher specific impulse and lower propulsion system mass than the chemical propulsion and higher thrust and transfer times compared to electric propulsion.

2.2. Existing STP Engine Concepts and Designs

To have an idea of the existing STP engine designs and their evolution, we need to delve into the previous phases of research done. Over the years, the receiver design has evolved. Some of the most notable conceptual and experimented designs are described here.

In 1962, one of the first STP experimental and analytical studies was funded by AFRPL which presented a typical system with large concentrators as shown in figure 2.3.

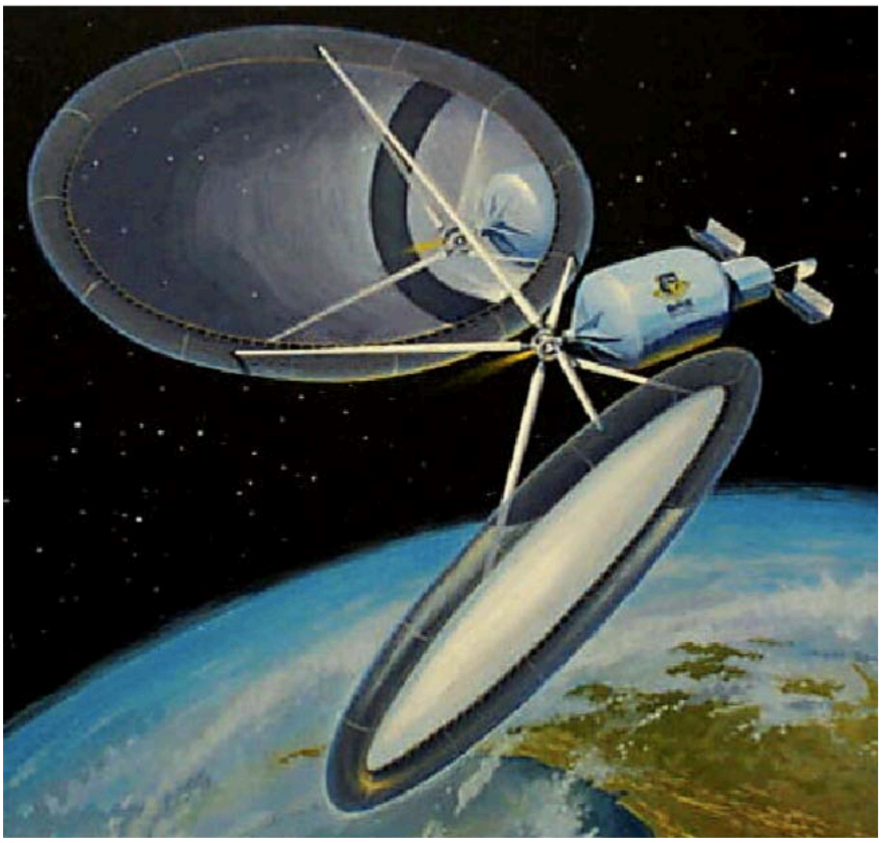

Figure 2.3: Conceptual design of a solar thermal propulsion system [17]

This STP system used hydrogen as its propellant and a specific impulse of 680 seconds was attained. However, the project was not continued due to the lack of recognition of the potential of solar thermal propulsion for the launch vehicles that existed in the early 60s and the inclination towards highly funded research in chemical, electric and nuclear thermal propulsion systems [18]. Etheridge [18] presents the evaluation of an STP system relative to conventional systems for the STS, selected as a launch vehicle. The report includes an in-depth study of the collector concept, as well as performance based on its deployability, high concentration ratio, and low specific mass. It has also presented an investigation of the thruster/ absorber performance. Etheridge conducted a thorough comparison between an STP system, a chemical system, and an ion propulsion system, and concluded that an STP system with a heat exchanger thruster design (with operating temperatures of up to 2500 K), inflatable collector and using hydrogen as the propellant, offers a viable option for deep space missions [18].

In 1999, Morio Shimizu et al. presented a paper on the design, fabrication and test results of a single crystal molybdenum solar thermal thruster with a windowless cylindrical cavity, having an inner and outer diameter of 20 mm and 30 mm respectively, for a 50 kg micro-satellite. A schematic diagram of the thruster design can be seen in figure 2.4.

The absorber/receiver has adopted the principle of indirect heating of the propellants through pipes surrounding the outer chamber of the thruster. The propellant is fed through the propellant supply pipes on each side as shown in the figure 2.4. The experimental testing was done for both N_2 gas and He gas as propellants. For a thruster chamber temperature of 1600 K, a specific impulse of

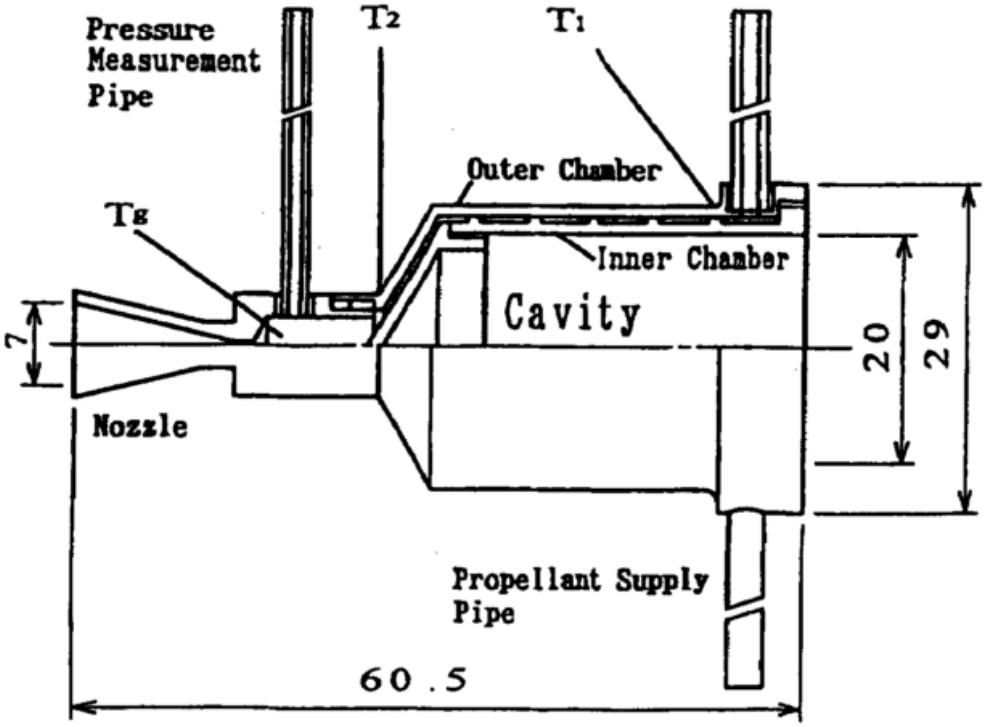

Figure 2.4: Single crystal molybdenum solar thermal thruster sketch [19]

about 650 seconds was attained, using N_2 gas as the propellant, at a maximum chamber pressure of 1.0 MPa. The experiment incorporated a parabolic concentrator of diameter 1.6 m with a focal length of 65 cm. Similar results were observed for He gas [19].

In 2004, F.G. Kennedy presented two designs of solar thermal engines for micro-satellites of mass no more than 100 kg, with the objective of expanding the mission options available for small satellites. The mission capabilities of micro-satellites are generally constrained and limited by the launch opportunities available as they are mainly intended for large (host) satellites, and the micro-satellites are usually inserted in non-optimal orbits. A number of missions for the application of STP has been investigated and the following missions were selected: 1) Near earth objects / Near escape flybys which need a delta V of 770 m/s with short firings at perigee, 2) GEO insertion mission which requires a delta V of about 1700 m/s and 3) Other body (capture) missions, requiring a delta V in the range of 1100 m/s - 4000 m/s [17]. The system requirements for the design of the STP engine was developed based on these.

Kennedy describes two micro-scale thrusters with solar receivers, namely, Mk.I and Mk.II. The Mk.I solar receiver incorporates a particle bed concept for a high wall to propellant heat transfer efficiency, whereas, the Mk.II. receiver integrates a single channel heat exchanger for simplicity. Figure 2.5 shows the Mk.I design depicting a particle bed receiver concept. The propellant selected for the purpose of the above-mentioned mission and design is hydrazine (N_2H_4). After a thorough test conducted on the two designs, it was concluded that the Mk.I has a higher heat transfer efficiency and is characterized to be heavier and more complex with respect to Mk. II. The author proceeds with the Mk.I design for the purpose of his study, as priority is given to the heat transfer efficiency of the system.

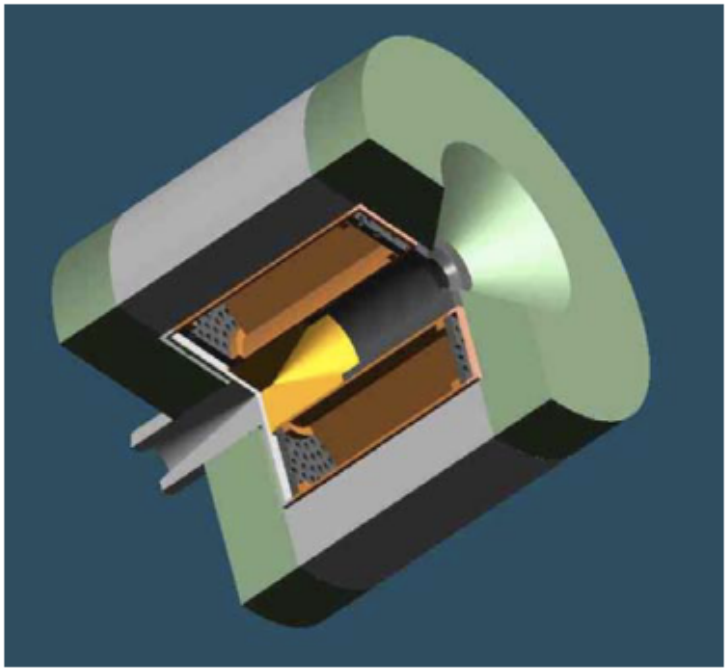

Figure 2.5: Mk.I thruster design [13]

There have been several works of research conducted on propulsion systems at the Department of Aerospace engineering in TU Delft, and especially focusing on micro-propulsion systems in recent years. In one of the studies done at TU Delft, a prototype of a solar thermal thruster was developed, and its ability to generate thrust utilizing thermal energy was studied. Building upon the system requirements for TU- Delft's CubeSat (Delfi-n3Xt), the final design was tested and concluded to be identified as a system that provides a high specific impulse for its dimensions and generates thrust in the range of 20-100 mN with an effective exhaust velocity of 500 m/s [12]. The final design of the thruster demonstrated in the department is shown in figure 2.6.

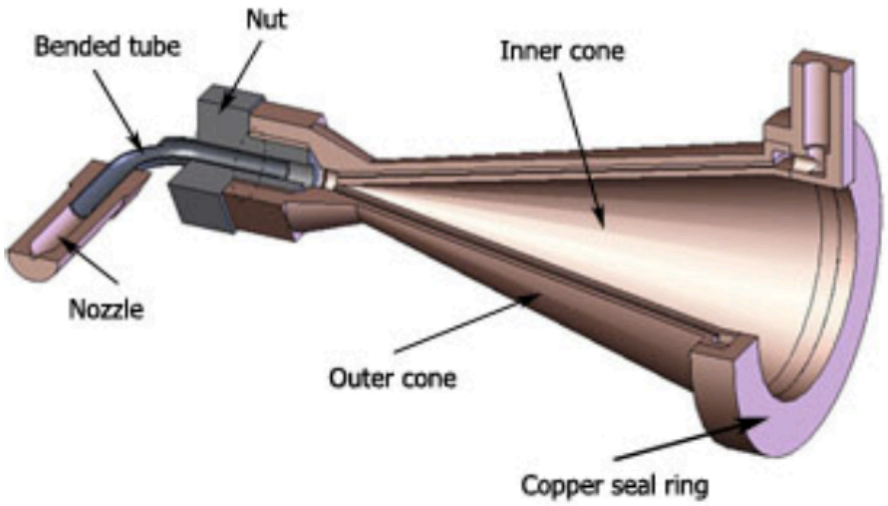

Figure 2.6: Final RAC design with nozzle[12]

Another research work done on solar thermal propulsion by [20] has demonstrated a concentrator design along with a preliminary design of a solar thermal propulsion engine for PocketQubes, which have a dimension of 5 cm x 5 cm x 5 cm. The aim of the research was to develop a concentrator that could be integrated with a possible solar thermal thruster to set up an STP system. The small-scale STP thruster design presented in this paper may be viewed as a reference point to study the MEMS solar thermal thruster. The author presents a simple concept of an STP engine which is compact and has a low system mass. The design incorporates a flat heat exchanger with multiple rectangular channels for the transfer of heat energy to the propellant. The wall of the flat heat exchanger acts as a receiver. The figure 2.7 shows the conceptual design of the STP engine [20]. Using ammonia as the propellant, the design provides a thrust of 162.4 mN and a specific impulse of 200 s assuming 222.76 W as the received input power from the inflatable concentrator.

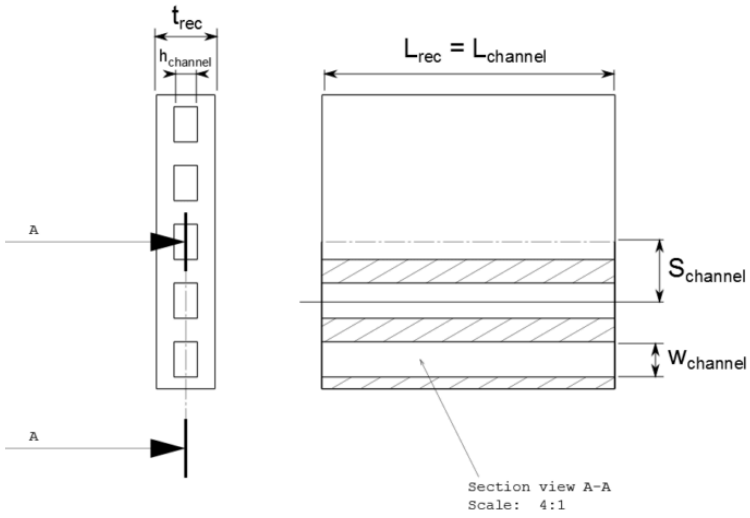

Figure 2.7: STP engine concept for PocketQubes [20]

To conclude, the STP has been characterized as a good intermediate between chemical and electrical propulsion systems. It is observed that most of the available STP designs are for small satellites and micro-satellites, but none for nano-satellites. Designing an STP engine which can be integrated into a CubeSat would not only allow nano-satellites to perform formation flying but also expand the possibility of deep space missions with its higher specific impulse and shorter transfer time compared to the existing chemical and electrical propulsion systems respectively, and thus has great potential. The design of solar thermal thruster can, therefore, be a key component for the on-going project at the TU Delft which deals with the Solar Thermal Propulsion engine and the Power System for Small Spacecraft.

2.3. Preliminary Mission Analysis

This section briefly explains the study of nano-satellite and micro-satellite missions including all past, present and future missions that could be a potential mission that may benefit from the solar thermal propulsion system. A comprehensive study of the application of solar thermal propulsion was carried out for satellites varying from 3U CubeSats to those of 100 kg mass in [21]. The aim of the mission analysis was to select three mission concepts that will be studied in detail and to evaluate whether an STP thruster system would benefit any mission in comparison to the existing propulsion systems.

The process of selection of a suitable mission or application involved a preliminary calculation of thruster performance that STP can offer for the particular satellite mass. The assumed input parameters were the propellant mass, ΔV and the specific impulse required for a mission, and subsequently, a comparison between the existing propulsion systems found in literature and the STP system was executed. The eventual trade-off between the missions ended up to be between DelFFI (TU Delft), the proposed LUMIO mission and the GTO-GEO Mission. A detailed STP performance table for each mission can be found in the literature study report [21].

The outcome of the thorough analytical analysis of the three mission concepts was that the lunar mission, LUMIO to be specific, was found to be the most suitable mission and benefiting from an STP system. LUMIO is a proposed 12U CubeSat mission to a halo orbit at Earth-Moon L2 that will mainly observe, quantify, and characterize the meteoroid impacts on the far side of the moon. The main propulsion system for the lunar mission must be capable of station keeping and executing the orbital transfer from the low inclination orbit of the moon to a halo orbit. Some of the main requirements for the mission require the propulsion system to have the capacity to generate a minimum ΔV of 154.39 m/s from the primary propulsion system and a minimum total impulse of 72.91 Ns from the RCS thrusters. The primary propulsion system shall produce thrust in the range of 500 mN to 1 N and shall have a maximum thrusting time of 8 hours per orbital transfer manoeuvre [22]. Hence, this mission has been carried forward to investigate further in this thesis.

2.4. System Requirements

Based on the above-mentioned objective and information, in order to achieve a combination of a clean and safe propulsion system along with miniaturization of an STP engine for the selected 12U CubeSat, MEMS technology seems to be a fitting process for the purpose of this study. Hence, it is important to delve deeper into the designing of a MEMS solar thruster for the CubeSat. The solar thruster must be designed in a way such that it can be coupled with a concentrator/STP system. Based on the available test set-up for a micro-propulsion system at the Department of Aerospace engineering, TU Delft, any possibility to develop from existing testing practices needs to be looked into in order to reduce the time and cost aspects of the project. This section describes the design parameters and system requirements of the selected mission.

Table 2.1: System requirements for an STP system for LUMIO mission

ID	Requirement	Lunar mission	Rationale
REQ-STP-01	Operating pressure	System operating pressure shall be below 5 bar	The CubeSat regulations state that "No pressure vessels over 1.2 standard atmosphere shall be permitted." [14], however, the maximum operating pressures for micro-propulsion systems have been seen to be between 1-5 bar [23][11] .
REQ-STP-02	Propulsion sub-system volume	The subsystem shall not exceed 4U of CubeSat volume	The limits are generated based on the survey done on existing propulsion systems and system volume. The reference volume for lunar mission is 4U [22].

Table 2.1: System requirements for an STP system for LUMIO mission

ID	Requirement	Lunar mission	Rationale
REQ-STP-03	Propellant mass	The propellant mass shall not exceed 15 % of the satellite mass	The limits have been implied based on available propulsion systems and from proposed mission data.
REQ-STP-04	Thrust Range	The system shall have a thrust range of 0.4 mN to 1N	The thrust range for lunar mission has been taken from the CDF study of LUMIO.
REQ-STP-05	ΔV	The system shall generate a total budget of 160 m/s	The reference ΔV value for Lunar mission is 154.39 m/s [22].
REQ-STP-06	Propellant temperature	The propellant temperature shall be limited to 1000 K	The preliminary critical nozzle design analysis defines the values based on Reynolds number to check the feasibility of the design. The initial values have been also taken from literature [12] [13]. This parameter is directly related to the concentrator dimensions and/or thermal storage.
REQ-STP-07	Wet mass	The wet system mass shall take up a maximum of 40 % of the total S/C mass budget [24]	In case of deep space and orbital transfer missions.
REQ-STP-08	Total Impulse	The min total impulse shall be 3.908 kNs	The requirements are calculated for proposed designs for the missions. The reference total impulse value for Lunar mission is 5162 Ns.
REQ-STP-09	Power Required (Electrical)	The power consumption shall not be greater than 15 W	Given power consumption for proposed design for the missions from literature.
REQ-STP-10	Mission Duration	The system shall provide at least 1 year of mission	Given mission durations for proposed designs for the missions from literature.

2.5. Research Question, Aims, and Objectives

2.5.1. Research Objective

The objective of this research is to design a MEMS solar thermal propulsion thruster that can fit in one CubeSat unit and analyze its performance by developing a thermal model. It must also be possible to integrate the design with a concentrator of the STP system developed by TU Delft.

As this research will mainly focus on designing and investigating the performance of a MEMS solar thermal engine for flight on board a CubeSat, the sub-goals listed will be studied and executed in order to accomplish this objective.

Objectives:

1. A trade-off between the range of 3U CubeSats to 50 kg CubeSats for deep space missions such as the Lunar mission, Asteroid fly-by mission, and GTO to GEO orbit transfer mission has been conducted to identify the most suitable and benefiting mission type for STP system application during the literature study. The conceptual design chosen from the trade-off will be investigated further to see whether the limitations can be eliminated.
2. From the system requirement table generated for the suitable mission using a systems engineering approach, a detailed STP thruster design will be accomplished.
3. The various design parameters that affect the performance of the STP thruster will be identified and modeled. Selection of the most suited material for the receiver cavity and insulation around the heat exchanger will be finalized. Selection of insulation and receiver cavity materials that will be used for the designing of a MEMS STP thruster will also be performed.
4. Development of a thermal model of the design to get a comprehensive idea of the heat distribution through the thruster design and study of the flow through the channels will be done. The outcome of this task and the one above would be most important as it would provide insight into how the heat can be prevented from entering other components on-board the CubeSat, as well as provide information on the efficiency of heating the propellant and performance of the system.
5. A system requirements compliance study will be carried out at the end of the thesis based on the final performance of the system.

The framework is limited to a theoretical design of the thruster. Manufacturing, integration, and testing of the component fall out of the scope of this research and will be considered only if time and funding permits.

2.5.2. Research Question

In this section, a research question has been formulated based on the description of the problem given above and the trade-off between systems that will be considered during the thesis.

How can a MEMS solar thermal thruster be designed such that it fits within a 1U CubeSat volume and offers proper integration for a concentrator/STP system aboard a 12U CubeSat?

In order to achieve an answer to the main research question, the following sub-questions are proposed to be studied:

Q. 1. Can the STP thruster for the selected mission be integrated with the system based on MEMS?

   (a) What are the difficulties and limitations of such a design?

Q. 2. What are the performance parameters, geometrical and material characteristics of the proposed design?

   (a) What is the power needed to heat the mass flow rate considering a power input efficiency?

(b) How does the cavity shape affect the performance in terms of radiation loss, mass and temperature distribution?

(c) How does the propellant temperature affect the Cavity diameter and length?

Q. 3. What are the challenges and design constraints with developing a MEMS solar thermal thruster especially at the thruster nozzle?

(a) What is the applicability of the ideal rocket theory for micro-propulsion thrusters?

(b) What are the assumptions to be considered for characterizing thruster design?

(c) What are the limitations of nozzle sizing with respect to propellant flow parameters.?

(d) What is the maximum temperature the Receiver cavity can sustain with respect to satellite and materials used?

(e) What are the effects of temperature on the nozzle dimensions?

Q. 4. What is the most efficient method of heat transfer to the propellant?

(a) How would the dimensions of flow channels affect heat transfer between the cavity and channels?

(b) What are the heat transfer losses associated with the flow and receiver cavity?

(c) How can the thermal modeling and analysis of a MEMS solar thermal engine be executed?

(d) How can the thermal model and analysis tool be validated apart from testing?

2.6. Design Methodology

The design process for the STP thruster is illustrated in this section. After a thorough study of the working of solar thermal propulsion its component's design parameters i.e, concentrator, receiver-absorber cavity, the interface between concentrator and receiver cavity, conceptual designs are presented. Furthermore, an insight of CubeSat design specification and operational requirements and regulations are kept in mind before finalizing the conceptual thruster model as a CubeSat imposes a restriction on acceptable mass, volume, and power. This is followed by defining a baseline model based on preliminary calculations of the ideal thrust performance and channel flow properties. Subsequently, for a selected channel length (from the baseline model), the parametric study of the channel flow properties and the attainable temperature is carried out.

Parallel to the thermal model of the flow and channel wall, the optical model comprising the optical fibers and concentrator runs to determine the power required for the heat exchanger system, the mass of the system and the efficiency. The output of the optical system model is then given as an input to the thermal model of the heat exchanger to determine the stored energy and the heat loss associated with the design. The ray tracing model in Comsol is included in the iterative design process to investigate the intensity and power deposited on the inner cavity surface. The expected outcome of this model is a beneficial cavity height dimension of the heat exchanger. Once the channel dimensions are estimated, the pressure drop in the channel is determined. This is then given as an input to the thruster model where the thrust performance, losses, and engine efficiency is computed.

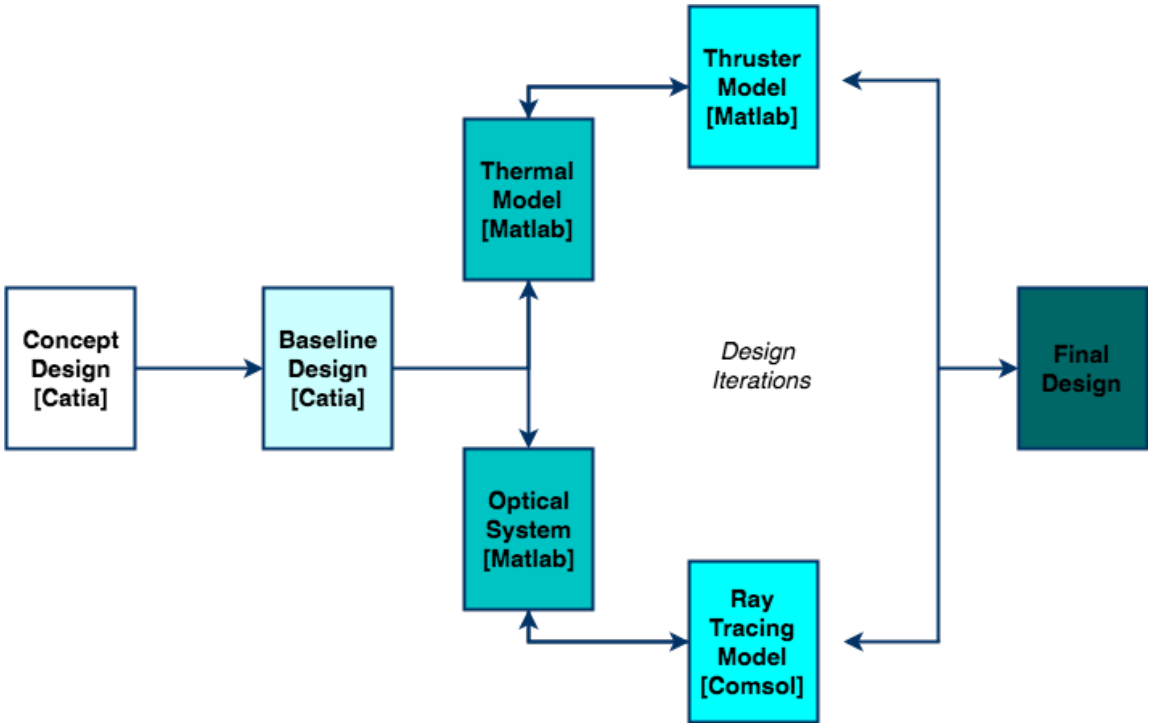

Figure 2.8: Design methodology

The final design generated from the iterative process in Matlab is subsequently verified with the ray heating numerical model and conjugate heat transfer model in Comsol.

3

Conceptual Designs

The chapter deals with the selection of sub-components of the STP system which is illustrated through a design option tree in section 3.1. In order to proceed with the selection of a promising heat exchanger design, the STP system design has been divided into the heating method, cavity shape (that defines the contact and surface area for heating), channel geometry and dimension, nozzle shape, and concentrator - receiver interface. Each of these sub-components is studied and described in the following sub-sections. The chapter then progresses with presenting three conceptual designs in section 3.2. This is followed by concept selection based on a graphical trade-off. The thruster performance is assumed to be the same for all three concepts and, therefore, the trade-off criteria is mainly derived from the system requirements for a heat exchanger as defined in section 3.3.

3.1. Design Option Tree

The first step towards selecting the sub-components of the STP system is generating a design option tree. All options for each sub-system are presented in the figure 3.1 shown in the next page and based on preliminary calculations and trade-offs, a final concept is selected.

3.1.1. Concentrator - Receiver Interface

The interface between receiver and concentrator is an essential system configuration that needs to be taken into account for the STP system design. In this section, two methods of directing sunlight to the receiver have been studied.

1. **Conventional system integration**
   The conventional fixed and on-axis concentrator focuses the concentrated solar energy on the focal spot of the receiver.

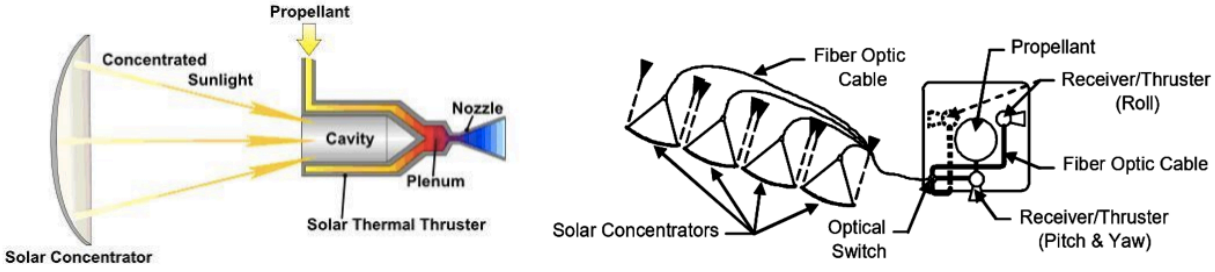

Figure 3.2: Left: Schematic of conventional solar thermal propulsion [1]; Right: Optical wave (OW) guide solar thermal propulsion system with integrated optical wave guide ACS [2]

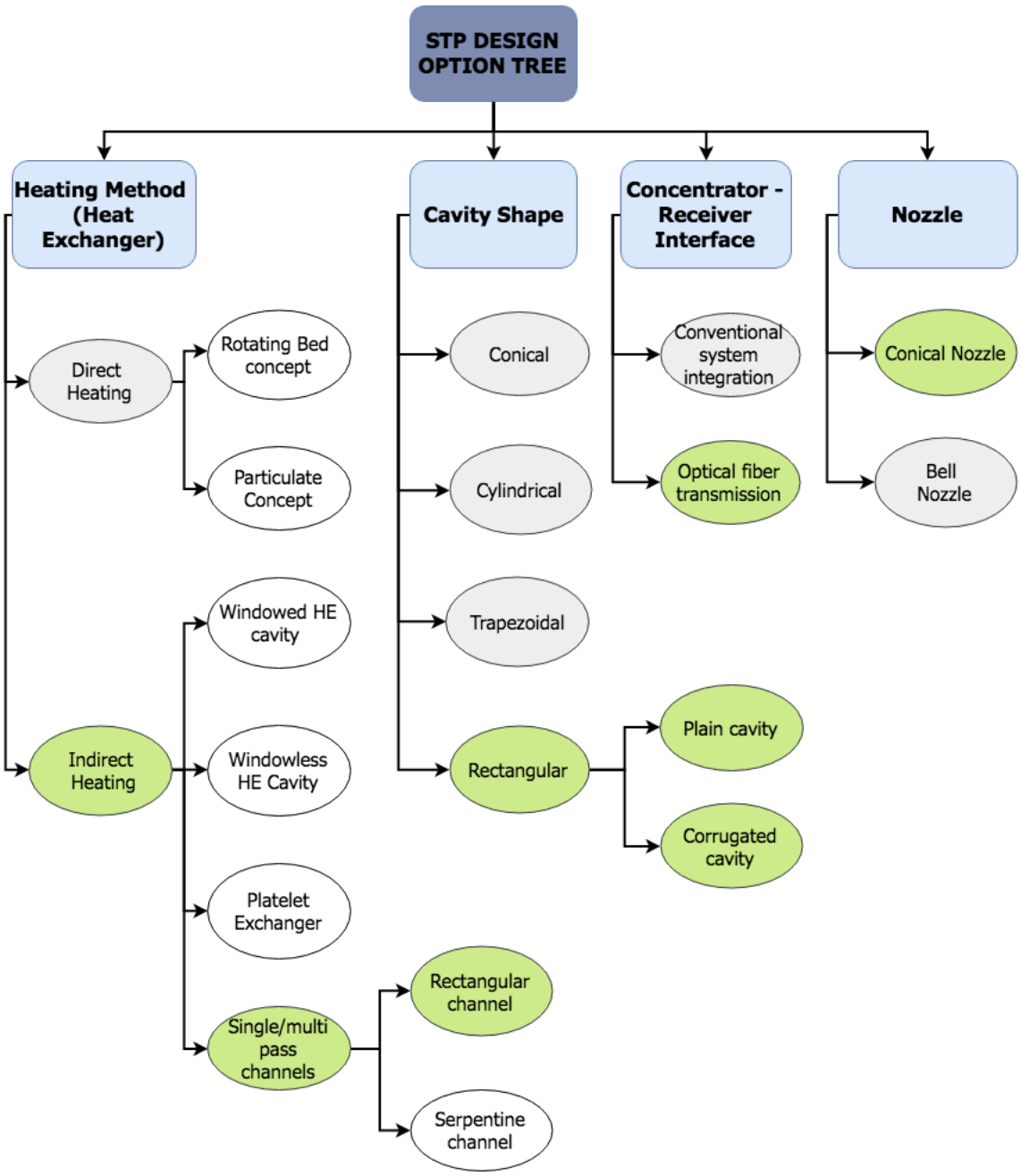

Figure 3.1: Design option tree

2. **Optical fiber transmission**
   The optical fiber cables are used to pass sunlight from the concentrator focal point to the propellant heating cavity. This concept has existed since the 1970s and was first proposed for small satellites by the University of Surrey in 2004 [2] [17]. In 2005 the application of fiber optics in STP systems was studied by Paul R. Henshall et al. and it was observed that its application in small satellites offers a degree of flexibility as it decouples the thruster from the concentrator, eliminating design constraints imposed by conventional systems as the concentrator can remain pointed at sun at all times. Also, fiber optics facilitates replacement of large concentrators with multiple small concentrators, thus lowering the system mass as a lower

support structural mass is needed [2].

The table below points out the advantages and limitations of both the conventional solar thermal propulsion system and the optical fiber solar thermal propulsion system.

Table 3.1: The potential benefits and limitations of the OW solar thermal propulsion system compared to a conventional solar thermal propulsion system

	Conventional system	**Optical Fiber system**
Advantages	Lower system mass (depends on the launch mass /mission type) - Higher efficiency compared to optical fibers	- Solar radiation can be switched to different receivers (Multiple thruster systems). - The heat energy can be guided to the ACS too (switch). - High system flexibility as it de-couples the concentrator from the RAC- thruster providing freedom from any imposed constraints.
Disadvantages	- Low system flexibility - Orientation of concentrators are RAC dependent - Multiple to one large concentrators. Increases complexity in case of multiple mirror system.	- Adds several grams to system mass. - The energy is attenuated and reduces the end-to-end efficiency [25]. - The optical fiber imposes limitations on concentrator diameter leading to either a multiple mirrors system or one large mirror using bundled optical fibers. In either case the mass of the optical system can either be advantageous or disadvantageous depending on the power requirement and support structure mass.

From the literature study it was concluded that for the concentrator-receiver interface, optical fibers are more advantageous compared to the direct focusing of concentrated solar energy, as can be seen in the table 3.1 below. A detailed analysis of the benefits of the optical fiber system for the selected mission will be executed later during the thesis.

3.1.2. Heating Method

The receiver is the most important sub-component of the STP system since it absorbs the heat flux directed from the concentrator and transfers the heat to the propellant. For an STP engine to operate at high temperatures and for it to be competent amidst other propulsion systems, the receiver must have the ability to transfer the heat efficiently to the propellant either directly or indirectly. This section will deal with the study of existing receiver concepts and their efficiencies, benefits, and limitations.

In the indirect method of heating, the receiver can either be an open cavity or windowed. The solar energy is absorbed by the walls of the receiver and the heat is transmitted to the propellant via conduction. Whereas in the direct heating method, the receiver is always windowed or has a closed

cavity design in which the propellant enters the chamber through porous walls and gets heated by the solar flux impingement through the window. A detailed description of all types of direct and indirect heating concepts can be found in the literature study report [21]. For the propellant heating method and type of heat exchanger feasible for a nano-satellite, the indirect heating system is favored because of the reasons listed below in table 3.2.

Table 3.2: The potential benefits and limitations of direct and indirect heating method

	Direct Heating (Particle beds & Rotating bed)	**Indirect Heating (Single/multi pass channels /Platelet)**
Advantages	Receiver is surrounded by heat transfer particles/ materials which increases the rate of heat transfer.	Flow experiences low pressure drop.
		Lower complexity compared to particle beds.
		Receivers are less massive.
Disadvantages	High complexity	Moderate heat transfer (limited heat exchanger temperature)
	Particle bed receivers are more massive	
	The bed is required to be kept in place during thrusting.	
	Risk of material clogging the nozzle or mesh.	
	Flow experiences a high -pressure drop.	

3.1.3. Cavity Shape

Since the goal of this thesis is to develop a MEMS thruster, all options that are difficult to manufacture are eliminated. Therefore, only the rectangular and trapezoidal cavity geometries will be considered for the design. In the case of a rectangular receiver shape, two geometries, namely, plain and corrugated inner surface, will be investigated during the thermal analysis of the system. Research done by Clifford K. Ho et al. for the macro-scale to micro-scale receivers showed that both tests and simulations of the irradiance distribution on corrugated samples produced greater irradiance in the valleys of the corrugations that promoted higher solar absorptance relative to the flat samples [3]. One of the most important advantage of corrugated sample is that it offers more surface area, hence more heat flux.

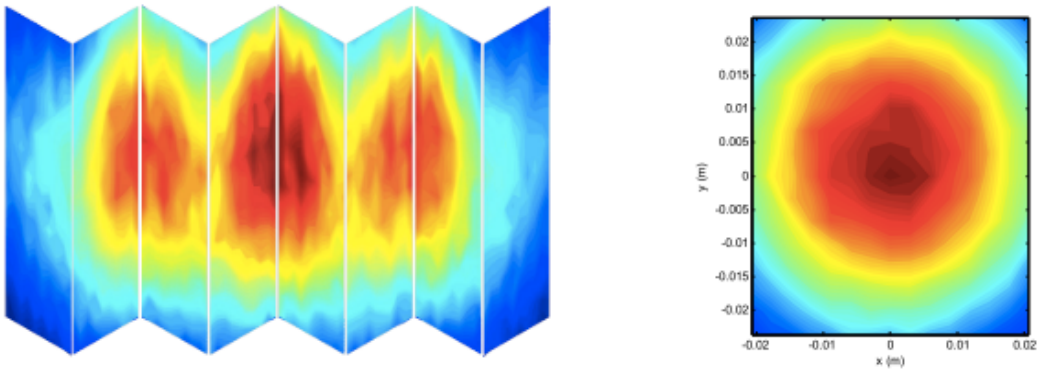

Figure 3.3: Net irradiance distributions on corrugated and flat samples [3]

The results of this paper concluded that corrugation improves solar absorptance, especially for lower absorptance materials like alumina, due to reduced emittance as the concentrated sunlight permeates further at the valley. A 30 % increase in absorbed solar power is observed in corrugated surfaces over the plain one. While corrugated surfaces do add to the mass budget of the system and a homogeneously heated heat exchanger is expected, it will be explored further for enclosed cavities and its influence on the thermal performance of the system.

3.1.4. Nozzle Shape

An ideal nozzle shape can be defined as the passage that offers an expansion area for the supersonic flow and simultaneously minimizes losses due to transverse velocity components by facilitating flow alignment in the axial direction at the nozzle exit. The bell-shaped nozzle is known to be the most ideal shape since it has a high expansion angle behind the throat section and maintains isentropic flow conditions throughout the nozzle section [26].

However, the bell-shaped nozzle has two major difficulties when it comes to the micro-scale design. Firstly, MEMS manufacturing of the contour of the bell nozzles require high precision and since this fabrication precision is not readily available, this becomes one of the major reasons why this type of nozzle is not considered as a suitable micro-nozzle shape. Secondly, the theoretical nozzle profile is determined using inviscid flow theory as it cannot be obtained by quasi-1D theory, and it ignores the effect viscous boundary layers [27]. Adding nozzle corrections for this profile becomes more complicated and it becomes dependent on the Reynolds number through the nozzle.

The alternative to the bell nozzle is the conical nozzle. The simple design of this nozzle makes it one of the most widely used and easily fabricated micro-scale nozzles.

3.2. Conceptual Designs

To begin with the thruster design, three conceptual designs are presented with different HE and cavity concepts. It must be noted that the nozzle dimensions would remain identical for all concepts since it is dependent on the required thrust for the selected mission. The propellant inlet manifold is going to be the same for concepts 1 and 2 and differs completely from concept 3. Evidently, the ratio of the chamber inlet area to the nozzle throat area must be at least 3 to reduce the losses due to flow velocity of the gases in the chamber [26]. Therefore, concepts 1 and 2 have the same inlet area ratio (Ai/At) and it is different for concept 3, but all are ≥ 3. All concepts have an expansion

area ratio (Ae/At) equal to 25. This was followed by a trade-off of the heat exchanger concepts to select the most suitable design based on qualitative reasoning.

3.2.1. Heat Exchanger Concept 1

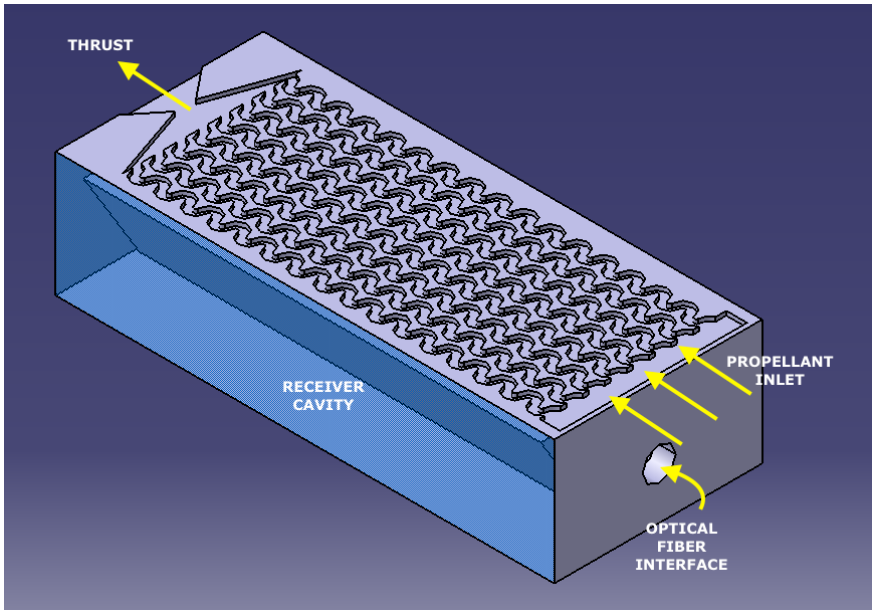

Figure 3.4: Concept 1 - trapezoidal cavity and serpentine channels

In this concept, a combination of a trapezoidal receiver cavity and semi-circular serpentine micro-channels have been presented as can be seen in the figure below. The cavity walls can be coated with IR coatings. In this design concept, the solar energy is transmitted into the cavity using a single optical fibre or the entire bundle depending on the concentrator design and requirement. The heated cavity then transfers the heat to the base of the channels via conduction and subsequently the heat is transmitted to water (propellant) via convection. The design represents a three-sided wall fin system. The phase change takes place over the length of the micro-channel leading to the vaporization and exit of the propellant through the nozzle. The design is similar to the micro-resistojet design developed at the space engineering department at TU Delft, where the heater chip used in the propulsion system has been replaced by a receiver cavity.

3.2.2. Heat Exchanger Concept 2

The following concept incorporates rectangular micro-channels etched below a corrugated cavity as shown below. The figure shows a corrugated cavity receiving heat energy transmitted by three optical fibres (assumed to be split from the optical bundle attached to the concentrator). Such a design is preferred over a flat surface, as in one of the research works done on cavities it showed that heat energy concentrated at the troughs were higher [3]. Manufacturing of the corrugated cavity (triangular) can be done using plasma etching. Also, a novel technique seems promising for such cavities - forced modulated indention process.

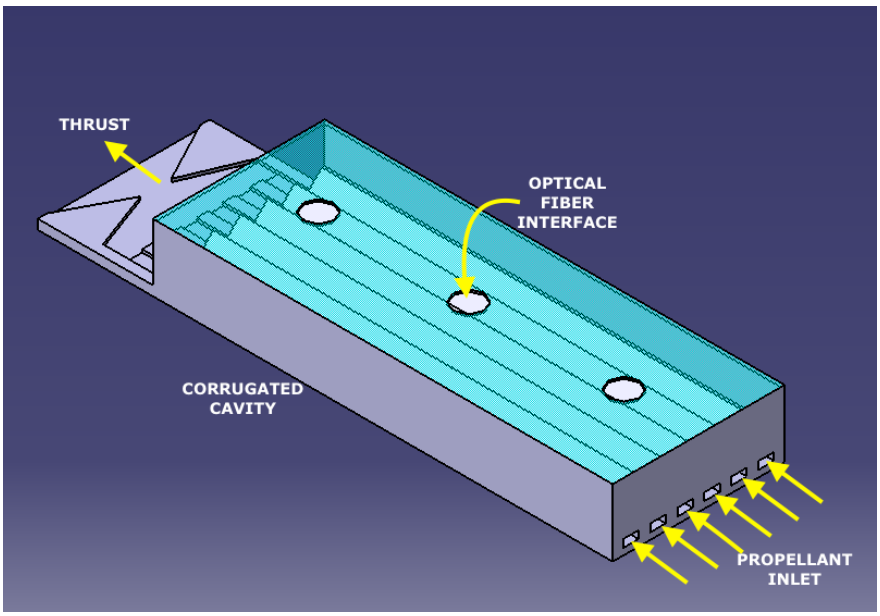

Figure 3.5: Concept 2 - rectangular corrugated cavity and rectangular channels

3.2.3. Heat Exchanger Concept 3

This concept presents the combination of the platelet heat exchanger concept along with rectangular dual cavities. This concept of indirect heating of the propellant is based on the novel platelet heat exchanger proposed by Y. F. Hou et al. in 2011 [28]. This receiver design, as shown in figure 3.6, consists of 20 layers of plates, where the thickness of each plate is 1 mm, the radial length is 9 mm and the metering passage is 0.1 mm. In this concept, the propellant flows from the cold wall outside to the hot wall.

In the case of a platelet heat transfer, the propellant uniformly flows into the heated passage of the heat exchanger (heated wall region) and during this flow path, the heat transfer between the propellant and the heated passage is maximum and enhanced. The efficiency and heat transfer coefficient of this system depends on the metering passage between the inlet of the cold propellant and the heating passage of the receiver wall. The platelet heat exchanger design shows high efficiency due to the large surface (contact) area for heat transfer as compared to spiral or rectangular channels. In the paper [29], the formed platelet heat exchanger was analyzed by simplifying the model to characterize the heat transfer taking place between the platelet and propellant. The following assumptions/theory was taken into account to proceed with the thermal model:

- One-dimensional and non-equilibrium model
- No phase change takes place in the passage

Further, calculations and experiments done by Yong Fa et al. [30] during the analysis of the platelet concluded that the wall temperature is directly proportional to the thickness of the platelet, i.e., the thinner the platelet, the lower is the wall temperature.

This following concept incorporates a dual cavity system with the linear concept of platelet heat exchanger. As can be seen in the figure 3.7, the propellant enters at the center of the heat exchanger and branches out toward the cavity outer wall through the metering passage. The propellant then

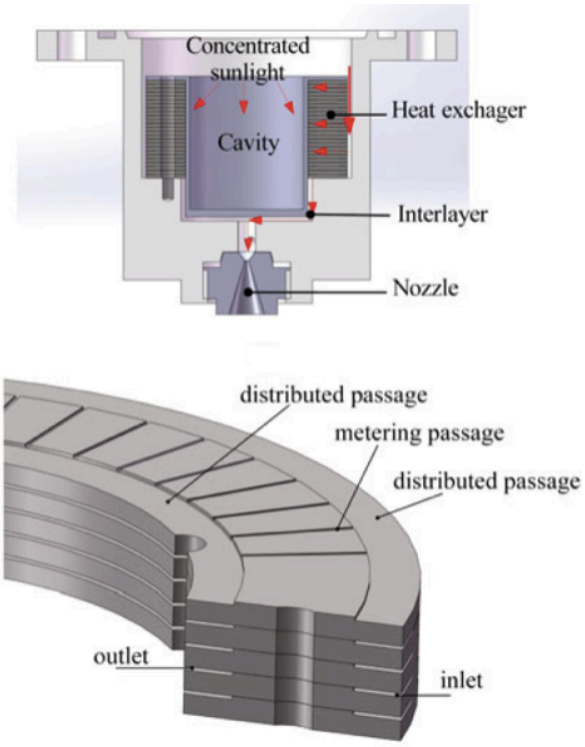

Figure 3.6: Platelet heat exchanger [28]

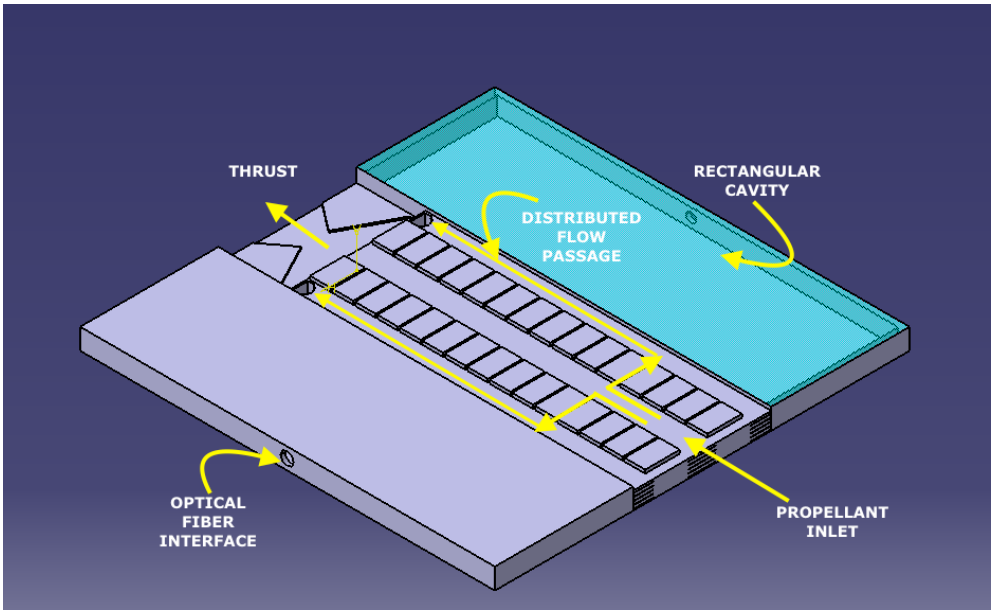

Figure 3.7: Concept 3 - platelet heat exchanger

exits through two 90 degree bends in the channel path to enter the nozzle section and subsequently be ejected through the nozzle. The heat exchanger, in this case, can be manufactured simply by complete removal of material followed by the deposition process and then etching layer by layer.

3.3. Concept Trade-off

This section discusses the selection of a concept based on system requirements defined for an efficient heat exchanger and trade-off criteria. A trade-off process helps in eliminating concepts that are not feasible based on qualitative and quantitative reasoning. In the table below, the system and performance requirements of a heat exchanger have been defined based on restrictions imposed by the available volume and general characteristics of an efficient system.

Table 3.3: Heat exchanger system requirement

ID	Requirement	Rationale
REQ-HE-01	The system shall have low mass and shall be reliable.	The requirement is imposed keeping the available volume for the entire system and total mass margin.
REQ-HE-02	The system shall have low pressure drop over the channels.	As increase in pressure drop is directly proportional to the pumping power required to drive the flow, a lower pressure drop is preferred.
REQ-HE-03	The system shall have a thermal efficiency of at least 70%.	The heat exchanger efficiency is defined as the ratio of the actual rate of heat transfer in the heat exchanger to the optimum rate of heat transfer. Value taken from [21]
REQ-HE-04	The system shall be simple and modular.	This criteria considers the manufacturability of the design as well as the interchangeability of the concepts.
REQ-HE-05	The system shall have total length less than or equal to 4 cm.	The criteria has been imposed keeping the volume available in mind. The aim is to fit the entire system (except propellant tank) within 1U volume of CubeSat.
REQ-HE-06	The system shall be able to attain at least 1000 K final propellant temperature.	The heating of propellant to 1000 K is required to satisfy the main system requirement.

3.3.1. Trade-off Criteria

The trade-off table given in figure 3.8 at the end of this chapter, is characterized by the criteria in the top row and concepts in the left column. For each concept, a reasonable justification is provided in the box with respect to the criteria which fall in either of the following categories: Exceeds requirements (in green), meets the requirement (in blue), adjustable (in yellow) and unacceptable/not allowable (in red). The trade-off criteria selected for concept selection are:

- *Pressure drop through the channels*
  Smaller pressure drop through the channels is preferred due to its proportional relation to the pumping power needed to inject the propellant into the heat exchanger.
- *Efficiency of the heat exchanger*
  System efficiency of the system, at a high level, can be defined as the ratio of the power transferred to the propellant to the input power. This factor is directly related to the surface area available for heating.
- *Mass of the heat exchanger*

The mass of the system is taken into account as it is one of the critical parameters when it comes to nano- or micro-satellites.

- *Manufacturability*
  This criterion focuses on the simplicity of the design and to evaluate whether the heat exchanger can be easily manufactured.

- *Channel length*
  Finally, the channel length needed to ensure heating of the propellant up to 1000 K is investigated and compared.

3.3.2. Preliminary Channel Length

In order to proceed with the trade-off of the conceptual designs, the length of the micro-channel is required to be determined and, in turn, the pressure losses associated with the channel geometry and configuration. Before moving ahead with channel length calculations, the flow regime expected through the micro-channel will be discussed.

Assumptions, Parameters and Equations

This section will explain the preliminary calculation of the minimum channel length required to vaporize the propellant and the assumptions and equations used. For a channel capable of heating the propellant from its inlet temperature to an end temperature of 1000 K, the channel wall (T_{wall}) is assumed to be at 1100 K, water inlet temperature ($T_{flow,initial}$) is at 298.15 K and the end temperature ($T_{flow,final}$) is considered to be 1000 K. Besides, constant convective heat flux is taken into account based on the equations described below. Mass flow rate ($\dot{m}$) has been estimated from the critical nozzle design calculations done during the literature study and has been computed to be 0.2529e-04 Kg/s. The boundary condition considered for the purpose of the initial calculation is stated below.

- Uniform wall temperature, where the calculation of the heat flux is based on the logarithmic mean temperature difference.

Equations

Newton's law of cooling is used to determine the heat exchanged between the receiver wall and propellant, given by

$$Q = h_c * A_{cs-channel} * \frac{(T_{flow,final} - T_{flow,initial})}{log\frac{T_{wall}-T_{flow,initial}}{T_{wall}-T_{flow,final}}} \tag{3.1}$$

Here, h_c is the convective heat transfer co-efficient and T_f represents the fluid reference temperature, which is given by

$$T_f = \frac{T_{flow,initial} + T_{flow,final}}{2} \tag{3.2}$$

The convective heat transfer coefficient can be calculated using the Nusselt number:

$$h_c = \frac{Nu * k}{D_h} \tag{3.3}$$

In the above equation, k is the thermal conductivity of the fluid [W/m K] and D_h is the hydraulic diameter of the channel. The D_h varies with the channel geometry can be computed with a simple equation depending on cross-sectional area and perimeter of the channel.

$$D_h = \frac{4 * A}{P} \tag{3.4}$$

The flow regime classification of the flow is required to be aware of its laminar or turbulent state. The characterization of the flow regime, based on the Reynolds number, can be expressed by the following equation:

$$Re = \frac{\rho U D_h}{\mu} \tag{3.5}$$

The Reynolds number depends on the flow velocity U and the density ρ. The Nusselt number (Nu) relation depends on the boundary condition considered. For laminar flow, Stephan's expression is used to determine the Nusselt number:

$$Nu = 3.657 + \frac{0.067 * (Re * Pr * D/L)^{1.33}}{1 + 0.1 * Pr * (Re * D/L)^{0.3}} \tag{3.6}$$

$$f = 64 * \left[\frac{1}{Re}\right] \tag{3.7}$$

The Nusselt number for turbulent flow has been calculated using the Gnielinski correlation [26]

$$Nu = \frac{\frac{f}{8} * (Re - 1000) * Pr}{1 + 12.7 * \left(\frac{f}{8}\right)^{1/2} * \left(Pr^{2/3} - 1\right)} \tag{3.8}$$

$$f = 0.316 * \left[\frac{1}{Re}\right]^{1/4} \tag{3.9}$$

The power required to heat up the propellant to 1000 K can be obtained using the following equation

$$Q = \dot{m} * \Delta H = \dot{m} * (H(T_{final}) - H(T_{room}))[W] \tag{3.10}$$

Using the above equations the length of the flow channel can be determined as follows

$$L_c = \frac{Q}{h_c * 2(h + w) * \Delta T_{lm}} \tag{3.11}$$

The flow velocity of the propellant through the channel can be mathematically expressed as follows:

$$U = \frac{\dot{m}}{\rho * A} \tag{3.12}$$

The non-dimensional Prandtl number is defined as the ratio of the momentum diffusivity to the thermal diffusivity, which fundamentally represents the relation of the heat transfer to the fluid flow. It can be expressed as:

$$Pr = \frac{\mu * C_p}{k} \tag{3.13}$$

The flow properties are determined for liquid water and water vapor by considering single phase flow, and the total length is obtained by adding the length required to heat up liquid water from room temperature to the boiling temperature at 5 bar plus the length required to reach 1000 K from the boiling temperature in the gas phase. Two-phase flow properties are not taken into account in this calculation but instead a margin of 2% for total length is considered. For the purpose of this trade-off, an arbitrary test case is considered with channel width and height for a rectangular channel of a 0.4 mm, an equivalent channel depth for a serpentine channel and a low aspect ratio channel for the platelet channels with the width being the same as 0.4 mm. The length of the rectangular channel was obtained to be about 0.03287 m and that of a serpentine channel was 0.0295 m. The total length in the axial direction of the flow for the platelet heated side was determined to be 0.0175 m.

Pressure Drop

The pressure losses due to frictional flow in the channels for single phase can be determined using the Darcy-Weisbach equation as follows,

$$\Delta P_f = \frac{1}{2}\frac{L}{D_h}\rho\, V^2 \tag{3.14}$$

In the above equation, L is the length of the channel. The velocity and temperature dependent density of the flow is denoted by V and ρ respectively. f is the friction factor which is related to the flow regime and depends on the channel parameters.

The losses due to bends in the channel path adds to the minor losses in pressure drop. Since the concept 3 incorporates channels with 90° bends, the pressure drop due to bend loss can be estimated using the following equation:

$$\Delta P_b = \frac{Re^2\mu^2 A_1 K_b}{2\rho}\left(\frac{A_1}{A_2}\right)^2 \tag{3.15}$$

In the above equation, K_b is the coefficient of loss due to bend, A_1 and A_2 are the cross-sectional areas of the channel and connecting channel post bend respectively and μ is the fluid viscosity (dynamic). For a 90° bend in rectangular micro-channels, K_b has been approximated to be 1.2 [31].

3.3.3. Graphical Trade-off

The first criterion, pressure drop, shows quite some variation between the three concepts. With the rectangular channel having the least pressure drop, it proves to be better than serpentine channels which experience a slightly higher pressure drop due to turns in the flow path or the multi-platelet channels which have the highest pressure drop as two 90 degree bends contribute to the drop in pressure. The mass of the stacked platelet concept is definitely higher than that of the concepts 1 and 2. Moreover, stacked layers in the concept 3 are not particularly beneficial as the heat transfer coefficient decreases with the increase in layers for the materials silicon and silicon carbide along with an increase in thermal resistance.

For this study, pressure drop is given the most importance as it determines the pumping power required for the system. A high pressure drop will lead to higher pumping power which in turn will increase the operational costs and mass of the system. Evidently, the concept 2 with rectangular channels seem to be feasible with the most ”exceeds requirements” category for the criteria and thus the detailed designing and analysis of this concept will be executed.

Heat Exchanger	Pressure drop	Efficiency	Mass	Manufacturability	Channel length
Concept 1 : Semi-circular Serpentine/wavy channel	Higher pressure drop than straight but better heat transfer co-efficient	Larger surface area w.r.t to straight channels and offers slightly higher final temperature	Low mass	Etching process (silicon carbide)	10% shorter than rectangular channels (in terms of total length of the heat)
Concept 2 : Rectangular channel	Lowest pressure drop	Small Losses due to lower flow velocity at the corners	Low mass	Etching process (silicon carbide)	
Concept 3 : Multi-platelet	Pressure drop decreases with increase in no.of layers depending on material but includes high pressure drop at 90 degree turns	Highest efficiency due to highest surface area	High mass (Depending on no.of layers)	Deposition and Etching. Involves bonding of Cavity side walls with HE	Due to metering channels, smaller channel length along the cavity is needed but much wider

Figure 3.8: Graphical trade-off between conceptual designs

4

Baseline Design

This chapter presents the baseline design of the selected heat exchanger and thruster concept. A preliminary design of the nozzle, heat exchanger and channels are obtained at the end of this chapter. The outcomes of the preliminary design are the power requirement for heating the propellant and the potential optical fiber-receiver interface position, thrust efficiency of the thruster, as well as mass and volume of the system. This is followed by the selection of an optical fiber and concentrator type suited for the application based on the power required for the process. The final optical system, comprising of the optical fibers and concentrator, is chosen based on the available volume and mass budget for the entire STP system. Some of the design parameters of the baseline design are assumed values taken from the literature as will be explained in the upcoming sections.

Section 4.1 discusses the fundamental properties of propulsion and studies the effect of nozzle geometry and flow losses on the thruster performance. Section 4.2 presents the materials list for the heat exchanger, insulation and optical fiber-receiver coupling interface. It is followed by section 4.3 which elaborates on the channel and cavity dimensions. Subsequently, the section defines and delves deeper into the flow regimes through the channels. Sections 4.4 to 4.7 focus on the optical system selection and parametric study.

4.1. Micro-nozzle Design

One of the constraints concluded from chapter 3 is that any section in the system allowing the total mass flow rate must be at least three times that of the nozzle throat. In the case where it is smaller than the nozzle throat, the section would act as a nozzle itself and makes the flow sonic. This leads to a high pressure drop over the channels. Therefore, the width of the convergent section at the channel outlet must be designed taking this constraint into account.

The preliminary nozzle dimensioning is based on the thrust required for the LUMIO mission. Referring to the system requirements table 2.1, the thrust needed for the mission is a maximum of 500 mN. As the maximum pressure within the system must not exceed 5 bar (**REQ-STP-01**), the preliminary design has assumed the stagnation pressure at the nozzle entry to be 5 bar (maximum limit). At this point, the pressure drop in the feed system and the heat exchanger has not been considered, but will later be taken into account once the heat exchanger dimensioning and thermal model of the system is accomplished in chapter 6 based on sub-section 4.3.2. Also, as listed in the table 2.1, the chamber temperature (T_c) or the temperature of the gas at the end of the heat exchanger channel is aimed to reach a temperature of 1000 K and hence this value will be treated to be the stagnation temperature at the nozzle entry.

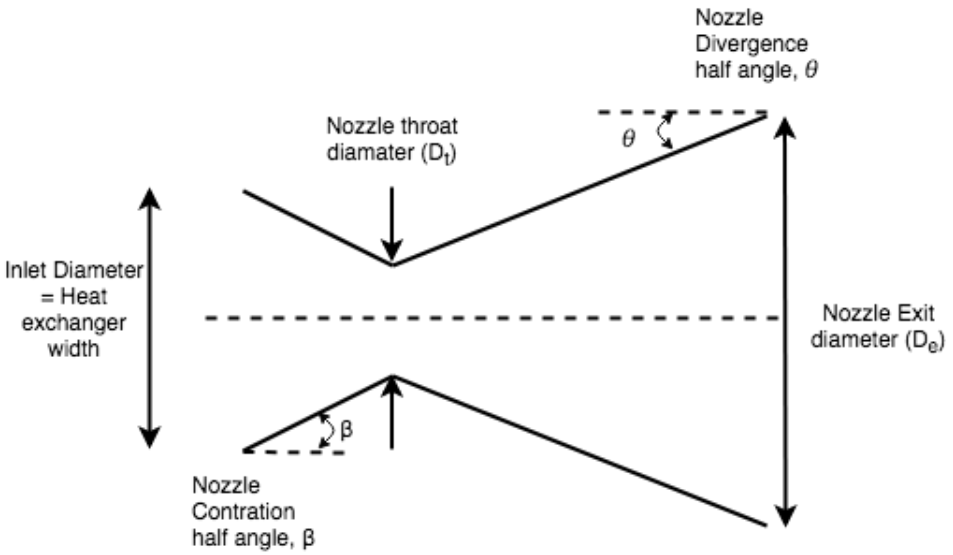

Figure 4.1: Conical nozzle configuration

The figure 4.1 shows the nozzle parameters and the shape considered as mentioned above.

4.1.1. Rocket Propulsion Fundamentals

The determination of the STP thruster performance is based on the Ideal Rocket Theory (IRT). While the ideal rocket theory is a good starting point for the preliminary design and is often near accurate for macroscopic nozzles, when it comes to micro-nozzles, there are several invalid assumptions that IRT considers. These invalid assumptions will be dealt with in the later part of this section in order to determine the real thrust performance. However, the following are the most important assumptions in this theory [12]:

- The expelled gases have a homogeneous composition.
- The behaviour of the exhaust gases is defined by the ideal gas law.
- The exhaust gases have a constant heat capacity.
- The flow through the nozzle is assumed to be one-dimensional, steady and isentropic.
- Flow discontinuities and shock waves do not occur.

One of the crucial performance parameters of a propulsion system is the thrust generated by a nozzle, and it can be expressed as [26]:

$$F = \dot{m}U_e + (P_e - P_a)A_e \tag{4.1}$$

The two components that affect the thrust produced are the momentum component, which is the first part of the equation, and the latter is the pressure component. Here, the mass flow rate of the gas is denoted as $\dot{m}$, U_e is the gas velocity at the nozzle exit, the stagnation pressure at the nozzle exit and ambient pressure are expressed as P_e and P_a respectively, and A_e is the exit area of the nozzle. The thrust equation can be simplified by assuming that the nozzle design will be able to achieve optimum expansion where ideally the stagnation pressure at the exit is equal to the ambient pressure. Hence the pressure component of the thrust equation can be eliminated.

The change in velocity ΔV needed to perform maneuvers can be calculated using the Tsiolkovsky rocket equation or ideal rocket equation:

$$\Delta V = I_{sp} g_0 \ln\left(\frac{M_{initial}}{M_{initial} - M_p}\right) \tag{4.2}$$

where g_0 is the gravitational acceleration at sea level, ΔV represents the change in velocity, $M_{initial}$ is the satellite wet mass and M_p is the propellant mass. For a given ΔV, satellite wet mass and an assumed propellant mass for the system, the specific impulse achievable can be determined.

The ideal specific impulse can be calculated using the equation 4.3. For a given value of thrust (F) and specific impulse, the mass flow rate can be estimated with equation 4.4.

$$I_{sp_{ideal}} = \frac{1}{g}\sqrt{\frac{2\gamma}{\gamma - 1} R\, T_c} \tag{4.3}$$

$$\dot{m}_{ideal} = \frac{F}{I_{sp} * g_0} \tag{4.4}$$

One of the most important design parameters of a propulsion system is the nozzle dimension. To calculate the nozzle throat area, the following equation in terms of mass flow rate can be used assuming choked flow at the nozzle throat:

$$\dot{m}_{ideal} = \frac{\Gamma\, P_c\, A_{throat}}{\sqrt{R\, T_c}} \tag{4.5}$$

Here P_c is the chamber pressure, T_c is the chamber temperature, Γ is the Vandenkerckhove function, R is the specific gas constant and A_{throat} is the throat area of the nozzle. From this equation, it can be noted that the throat area is directly proportional to the mass flow rate and the square root of chamber temperature and inversely proportional to the chamber pressure. The Vandenkerckhove function is defined as:

$$\Gamma = \sqrt{\gamma}\left(\frac{2}{\gamma + 1}\right)^{\left(\frac{\gamma+1}{2(\gamma+1)}\right)} \tag{4.6}$$

Further, the calculation of the exit area of the nozzle can be determined using a relation between the pressure ratio (P_e/P_c) and expansion ratio (A_e/A_t).

$$\frac{A_e}{A_t} = \frac{\Gamma}{\sqrt{\frac{2\gamma}{\gamma-1}\left(\frac{P_e}{P_c}\right)^{\frac{2}{\gamma}}\left(1 - \left(\frac{P_e}{P_c}\right)^{\frac{\gamma-1}{\gamma}}\right)}} \tag{4.7}$$

For the purpose of initial thruster performance estimation, the expansion ratio was assumed to be 25 after a thorough research done during the literature study [21]. For a given expansion ratio and throat area, the exit area can be directly calculated.

A fluid flow can be characterized into laminar flow, transition phase, and turbulent flow. These regions can be distinguished by the Reynolds number, a dimensionless number which is defined as the ratio of inertial forces to viscous forces within a fluid. The following equation is used for the determination of the Reynolds number for a specific throat diameter:

$$Re_{t_{ideal}} = \frac{4\ \dot{m}}{\pi\ D_t\ \mu} \tag{4.8}$$

where μ is the dynamic viscosity at the given propellant temperature and D_t is the throat diameter of the nozzle. Using the parameters in table 4.2 and the above mentioned equations, the nozzle throat area has been calculated to be 0.5282 mm² for a mass flow rate of 239.34 mg/s to produce a thrust of 500 mN.

Another important factor to consider is the Knudsen number. It is a dimensionless number that defines whether the gas flow is rarefied or is in continuum. The Knudsen number depends on the gas properties at the throat of the nozzle and can be mathematically expressed as a function of the mean free path of the gas molecules (λ) and the characteristic dimension of flow, which in this case is the hydraulic diameter of the nozzle (D_h) [32].

$$Kn = \frac{\lambda}{D_h} = \frac{\mu\sqrt{\frac{\pi}{2\rho P_c}}}{D_h} \tag{4.9}$$

The fluid properties used to calculate the Knudsen number is listed in table 4.2.The flow regime is determined by the value of Kn and can be characterized as: continuum flow regime with slip flow (0.1 > K n > 0.01); transitional flow regime (10 > K n > 0.1); and free-molecular flow regime (K n > 10) [33][34]. The table below shows the calculated Reynolds number and Knudsen number for a chamber pressure (stagnation pressure at the nozzle entry) of 5 bar, and constant nozzle area. The minimum value of the nozzle width is set to 0.5 mm as that would mean a depth of 1.0076 mm and the thickest wafer available for etching is 1.5 mm (considering a required base thickness of 0.5 mm).

Table 4.1: Flow properties at throat conditions

Nozzle throat area - 0.5282 [mm^2] Chamber pressure - 5 [bar]				
Nozzle Throat Width W_n [mm]	**Throat Height H_n [mm]**	**Aspect Ratio H_n/W_n [-]**	**Reynolds number at throat [-]**	**Knudsen number at throat [-]**
0.5	1.00	2.00	9.7821 E+03	3.6545 E-06
0.6	0.84	1.40	9.4019 E+03	3.5125 E-06
0.7	0.72	1.03	9.3046 E+03	3.4761 E-06
0.7098	0.744	1.00	9.3067 E+03	3.4769 E-06
0.8	0.63	0.79	9.0310 E+03	3.5844 E-06
0.9	0.56	0.62	9.2206 E+03	3.6597 E-06
1.0	0.51	0.51	9.4988 E+03	3.7701 E-06

According to the values in the table 4.1 and the study conducted in [35], it can be concluded that for a thrust level of 500 mN and above, the rarefaction and wall slip effects are negligible because of the considerably low values of Knudsen number. The Reynolds number at the throat for the nozzle dimensions presented in table 4.1 and using gas properties from table 4.2 indicate a turbulent flow.

The Knudsen number can be seen to decrease with a decrease in aspect ratio up until AR 1 and then increases thereafter. Clearly, the nozzle width and throat height reverse after aspect ratio 1 is crossed. The effect of Reynolds number on the nozzle performance will be discussed further in 4.1.2 but as explained above and proven empirically, at low Reynolds numbers, the loss in nozzle performance would escalate.

Table 4.2: Initial input parameters and fluid properties

Parameter	Requirement	Unit	Criterion/ Equation
Thrust	500	mN	Maximum thrust needed for the LUMIO mission.
ΔV	169.82	m/s	REQ-STP-05, (with 10% margin)
Chamber Pressure P_c	5	bar	REQ-STP-01
Chamber Temperature T_c	1200	K	REQ-STP-06
Gas Constant R (water)	461.376	J/Kg K	$R = \frac{R_c}{M}$
Specific gas ratio γ	1.34	-	$\gamma = C_p/C_v$
Dynamic viscosity μ	4.5069 × 10 5	Kg/m-s	NIST
Satellite initial mass, $m_{initial}$	24	Kg	12 U cubesat mass considering maximum allowable mass per unit.

4.1.2. Actual Performance

The real or actual performance of the thruster is in comparison to the ideal thruster performance that is obtained based on several assumptions derived from the ideal rocket theory explained in sub-section 4.1.1. The real performance of a micro-nozzle will vary from the ideal performance due to the effect of physical processes such as heat transfer, wall-gas interaction, flow rarefaction, flow separation, micro-nozzle geometry, etc., [26], these effects will be taken into account to indicate a more accurate nozzle performance. For instance, for systems with low Reynolds number flows, thick viscous layers are formed and they inevitably occupy a portion of the nozzle and affect the nozzle performance. The actual losses and impact on the flow behaviour due to the viscous layers, heat transfer and gas kinetics will be treated by incorporating correction factors that will be multiplied with the estimated ideal performance of the thruster and its efficiency [27]. The following losses need to be taken into account.

Low nozzle contraction ratios

Conventional nozzle theory states that for a chamber cross-section three times larger than the throat area, the losses due to the flow velocity at the inlet of the nozzle can be neglected [26]. Following the above mentioned condition, for a nozzle throat having a cross-sectional area of 0.5282 mm^2, the chamber cross-sectional area must be greater than or equal to 1.5846 mm^2. This limits

the flow velocity in the chamber to 0.0963 Mach.

Loss due to divergence of the flow

Generally, reduction in the thrust output is mainly caused due to undesirable velocity components in the transverse direction which is induced due to the flow alignment or the amount of displacement from the axial direction. These flow losses are directly dependent on the nozzle profile and hence, a brief study of the losses involved with the geometry has been done. In the case of an ideal nozzle profile, it is assumed to generate supersonic flow along the axial direction to deliver thrust with minimum losses. Since the nozzle profile selected for the purpose of this propulsion system is a convergent-divergent conical nozzle, a theoretical correction factor λ needs to be applied to account for the losses involved due to the divergence angle.

$$\lambda = \frac{(1 + cos\alpha)}{2} \tag{4.10}$$

The divergence loss factor will be multiplied only to the momentum component of the thrust equation.

$$F = \lambda \dot{m} U_e + (P_e - P_a)A_e \tag{4.11}$$

This factor can be defined as the ratio of the gas momentum at the nozzle exit (with a nozzle angle of α) to the momentum of ideal gases flowing in the axial direction [36]. For a conical nozzle with a divergence angle of 30° and an expansion area ratio of 25, the correction factor has been estimated to be 0.9829 [36].

Loss due to pressure ratio

As it was initially assumed that the stagnant pressure at the exit is equal to the ambient pressure in the ideal case for thrust produced, a high difference in the pressure values will induce flow discontinuities such as shock formation or flow separation at the nozzle. To prevent these discontinuities from taking place, the following condition must be regarded [32]:

$$0.35 < \frac{P_e}{P_a} < 0.45 \tag{4.12}$$

$$\frac{P_e}{P_a} = (1.88M_e - 1)^{-0.64} \tag{4.13}$$

However, since the thruster will be operated in the vacuum conditions of space, the ambient pressure will be zero and the losses generated due to the pressure ratio can, therefore, be neglected. For future testing of the thruster in the vacuum chamber at the Department of Space Systems Engineering of TU Delft, the minimum chamber pressure needs to be calculated to prevent flow separation within the nozzle.

$$\epsilon = \frac{A_e}{A_t} = \left(\frac{\gamma + 1}{2}\right)^{\frac{-(\gamma+1)}{2*(\gamma+1)}} \left(1 + \frac{\gamma - 1}{M_e^2}\right)^{\frac{\gamma+1}{2(\gamma-1)}} \frac{1}{M_e} \tag{4.14}$$

In order to determine the exit to chamber pressure ratio P_e/P_a, the exit Mach number is needed (M_e), which has been estimated from the above equation to be 4.3605 for an area expansion ratio of 25. The pressure ratio is then determined using the equation 4.13 and found to be 0.2827. Since the vacuum chamber facility is limited to a pressure of 0.21 mbar, the exit pressure must not be below 0.059367 mbar. Alongside this, the exit to chamber pressure ratio determined from equation 4.7 is 0.0027725. The minimum chamber pressure required to avoid flow separation would then be 0.0214 bar. Since the thruster nozzle has been designed to be working at 5 bar, the pressure criterion is well within the limit.

Throat radius sharpness

Miniaturization of nozzle dimension causes gas rarefaction leading to slip flow at the wall and alters the core of expansion flow from the sonic to the supersonic region. But for nozzles generating thrust higher than 1 mN the effects of rarefaction and slip flow can be neglected as also discussed in section 4.1.1. During the study of varying thrust range nozzles in [35], it has been established that in the thrust range of μN to mN, the boundary layer thickness increases with increase in the throat curvature (R_c) as the divergent length becomes longer. However, sharp throat curvature ($R_c = 0$) also can lead to the formation of a weak shock along the axial direction of the flow especially when the convergent angle is large which leads to strong deflection at the throat. The geometry of the nozzle can be determined by considering the throat curvature to be sharp and keeping the convergent angle comparatively small. A convergent angle of 15 degrees has been observed to offer high thrust efficiency for micronozzles [35]. The divergent angle will be determined depending upon the divergence loss and the effect of different angles on thrust efficiency in 4.1.3.

Loss due to boundary layers

The lower velocities at the wall boundary layers reduce the effective average exhaust velocity by 0.5 to 1.5% [36].

Loss due to Reynolds number

In micro-propulsion systems for small satellites, the Reynolds number at the throat for a flow through the micro-nozzle must be between $10^2 < Re < 10^4$ [24]. Ketsdever concluded that thick viscous boundary layers develop at Reynolds numbers below 1000, indicating poor nozzle efficiencies. The main cause of this inefficiency is due to the interaction of the subsonic boundary layer with the core of supersonic flow causing the flow to not expand fully in the diverging section [24].

The viscosity of a fluid flow is inversely proportional to the Reynolds number according to its definition. The lower the Reynolds number, the higher is the viscosity of the flow, which in turn contributes to the thickness of the boundary layer formed at the walls of the divergent section of micro-nozzles. Formation of these boundary layers causes a reduction in effective nozzle throat width and therefore the nozzle expansion area ratio. Consecutively, this lowers the mass flow rate through the nozzle throat affecting the thrust deliverable.

Therefore, to predict the real performance of the thruster, the discharge coefficient of the system needs to be determined. Since the Reynolds number at the nozzle (listed in table 4.1) is less than 2.2E+04, the nozzle will have a boundary layer of thickness significant enough to affect the throat width [26]. The discharge coefficient can be mathematically expressed as

$$C_d = \frac{\dot{m}_{viscous\ loss}}{\dot{m}_{ideal}} \tag{4.15}$$

Here $\dot{m}_{viscous\ loss}$ is the reduced mass flow rate due to the viscous flow. The ideal mass flow rate can be determined from the equation 4.5. The discharge coefficient (C_d) can be expressed as a function of Reynolds number and coefficients of nozzle function α and β.

$$C_d = \alpha - \frac{\beta}{\sqrt{Re}} \tag{4.16}$$

The discharge coefficient of steam or water vapour at the nozzle throat can be either determined by conducting experiments or by performing numerical simulations of the effect of boundary layers at the nozzle throat. The coefficient of the nozzle is a function of the specific heat ratio (γ) and for gases having γ between 1.3 to 1.4, the coefficient varies only by 0.1%. As there is a lack of

experimental and numerical data to characterize the discharge coefficient in critical nozzle using steam, the C_d data available for CO_2 will be used instead, since the specific heat ratio of CO_2 is 1.3 and that of steam is 1.34 [37]. The values of the coefficients α and β for CO_2 that were determined experimentally, numerically and analytically can be seen below.

Table 4.3: The values for α and β for CO_2 [9]

Gas	γ	α_{exp}	α_{num}	α_{diff}	β_{exp}	β_{num}	β_{diff}
CO_2	1.3	1.0168	0.9989	-1.76	3.077	3.370	+9.52

A numerical analysis was conducted for a critical Reynolds number range from 2000 to 22000 to match with the results obtained from experiments and the difference found was below 0.5 % which is considered acceptable. The experimental values of the coefficient will used to generate realistic answers. Subsequently, the actual throat area and effective velocity at the throat can be calculated as follows:

$$C_d = \frac{A_{t_{actual}}}{A_{t_{ideal}}} \tag{4.17}$$

For the varying Reynolds number for different throat width shown in table 4.1, it can be concluded that no significant losses are present due to viscous flow for the given throat area. As the depth of the nozzle will also be equal to the depth of the micro-channel, the dimension of the nozzle preferred for this study is with an aspect ration of 1 and throat width of 0.7098 mm, since it will later be established that it offers better heat transfer through the micro-channels for the given height. The C_d determined for the gas flow is 0.9842 for a nozzle width of 0.7098 mm. The final dimension of the nozzle will be determined after a brief analysis of the heat exchanger and its channels.

4.1.3. Effect of Nozzle Geometry on Nozzle Efficiency

Having determined the discharge coefficient, the nozzle efficiency/ nozzle quality can consequently be estimated. Since no experiment is conducted, the correction factors will be defined based on losses predicted in the nozzle. Below are the nozzle correction factors for different cases of varying nozzle aspect ratio.

Thrust efficiency

The thrust efficiency (η_F) is defined as the ratio of the real thrust, i.e including losses due to the flow, to the ideal thrust.

$$\eta_F = \frac{F_{viscous\ loss}}{F_{ideal}} \tag{4.18}$$

Here $F_{viscous\ loss}$ is the actual thrust and this can be determined by substituting the actual throat area and mass flow rate due to viscous loss into equation 4.11.

Nozzle quality

The nozzle quality, also known as the correction factor for thrust coefficient, is defined as the ratio of the thrust coefficient due to losses to the ideal thrust coefficient.

$$\xi_F = \frac{C_{F_{viscous\ loss}}}{C_{F_{ideal}}} \tag{4.19}$$

Here the thrust coefficient can be obtained using the relations:

$$C_{F_{viscous\ loss}} = \frac{F_{viscous\ loss}}{P_c\ A_{t_{actual}}} \tag{4.20}$$

$$C_{F_{ideal}} = \sqrt{\frac{2\gamma}{\gamma-1}\left(1-\left(\frac{P_e}{P_c}\right)^{\frac{\gamma-1}{\gamma}}\right)} + \frac{(P_e - P_a)}{P_c}\frac{A_e}{A_t} \tag{4.21}$$

Correction factor for specific impulse

The correction factor for specific impulse, also known as motor quality, is the defined as the ratio of the specific impulse delivered due to losses to the ideal specific impulse.

$$\eta_{I_{sp}} = \frac{I_{sp_{viscous\ loss}}}{I_{sp_{ideal}}} \tag{4.22}$$

The actual specific impulse can be determined by using 4.4 and substituting the ideal exhaust velocity with the exit velocity due to losses considered. The table below lists the quality factors for varying nozzle depth.

Table 4.4: Nozzle quality factors

Nozzle Throat Width W_n **[mm]**	**Reynolds number at throat** Re_{throat}	**Discharge coefficient** C_d	**Viscous mass flow rate** $\dot{m}_{viscous\ loss}$	**Thrust efficiency** η_F	**Specific impulse efficiency** $\eta_{I_{sp}}$	**Nozzle quality factor** ξ_F
0.5	9.9623e+03	0.9860	2.3599e-04	84.792	88.6718	85.9981
0.6	9.4755e+03	0.9852	2.3580e-04	84.724	88.6718	85.9981
0.7	9.3107e+03	0.9850	2.3574e-04	84.70	88.6718	85.9981
0.7098	9.3067e+03	0.9849	2.3572e-04	84.69	88.6718	85.9981

The thrust efficiency of the thruster is more or less same for different nozzle width at constant chamber pressure of 5 bar and throat area. Since there is no major change in thruster performance with respect to nozzle dimension (< 0.12%), the final selection will depend on the performance of the heat exchanger which is controlled by the channel height. Going by the trend, at larger drops in Reynolds number at the throat, the thrust efficiency will drop significantly.

Divergence angle of the nozzle versus thrust efficiency has been plotted as shown below in figure 4.2. It is obvious that the thrust efficiency decreases with increase in divergence angle but it must also be noted from the above calculations that at lower divergence angles, which means a longer divergent length, the loss due to viscous flow increases at the boundary walls. An optimum divergence angle of 20.42 degrees has been obtained by differentiating the thrust efficiency with respect to the divergence angle to determine the maxima. The thrust efficiency term includes the angle dependent Reynolds number over the divergent length and the reduction in nozzle exit area, i.e., including the effect of viscous and nozzle divergence losses. This value will be considered for the nozzle geometry.

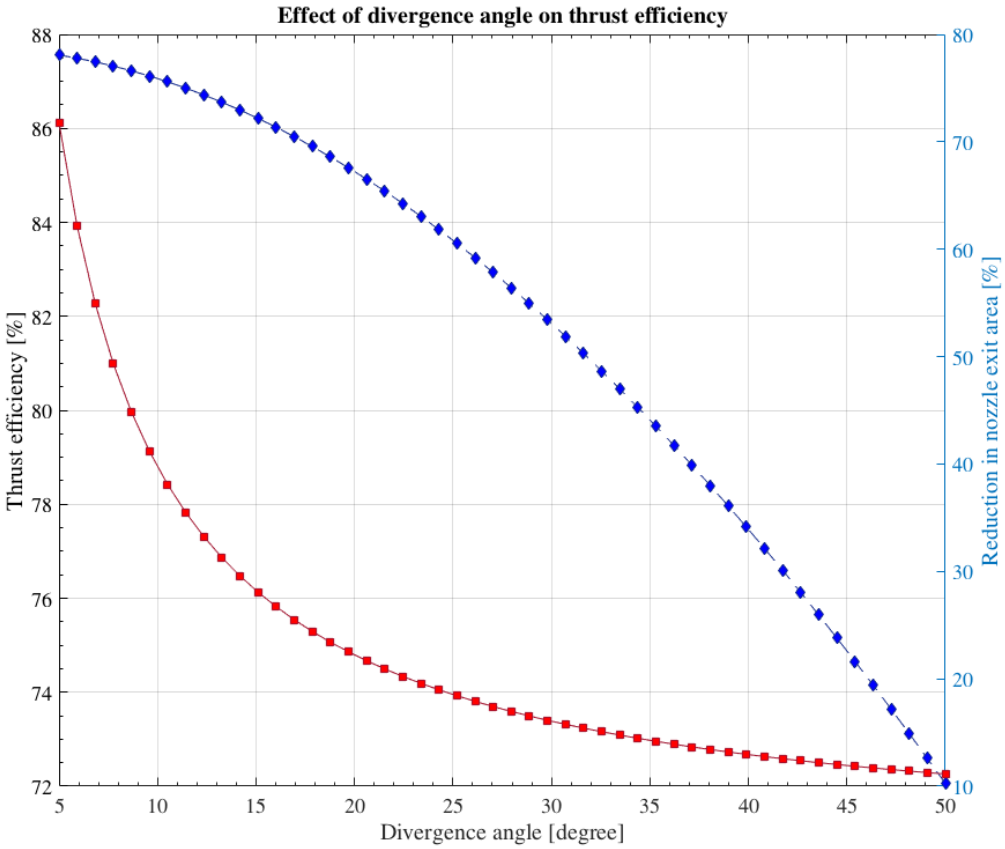

Figure 4.2: Effect of divergence angle on thrust efficiency

4.1.4. Thruster Performance at High Chamber Temperatures

The objective of the design is to ensure that the propellant gets heated up to 1000 K, the chamber temperature will be naturally maintained at a higher temperature. In case of the heat exchanger's incapability to heat up to the desired temperature, its effect on the thruster performance and efficiency must be known. Thus, this subsection will briefly deal with the thruster performance at temperatures between 500 K to 1500 K. To understand the effect of temperature, only one case of the nozzle geometry is considered, i.e., nozzle with a throat width of 0.7098 mm, constant chamber temperature of 5 bar and for an ideal thrust of 500 mN.

Table 4.5: Temperature dependent thruster performance

Sr. No	Chamber Temp [K]	Reynolds number at throat[-]	Ideal Specific Impulse [s]	Thrust Efficiency [%]	Mass flow rate [Kg/s]	Enthalpy Change [KJ/Kg]	Power [W]
1	500	3.410e+04	137.46	86.009	3.708e-04	2807.41	1.041e+03
2	600	2.340e+04	156.73	85.713	3.385e-04	3014.81	1.021e+03
3	1000	1.222e+04	194.39	85.049	2.622e-04	3883.21	1.018e+03
4	1200	9.307e+03	212.95	84.699	2.393e-04	4356.41	1.043e+03
5	1500	6.246e+03	238.09	84.095	2.141e-04	5106.32	1.093e+03

Looking at the Reynolds number values in the table 4.5, it can be inferred that with the drop in Reynolds number, the viscous losses in the flow increases with the increase in chamber temperature. Thus, a reduction in the thrust efficiency is observed. However, a drastic increment in the specific impulse is witnessed which implies a reduction in the mass flow rate required to generate the given amount of thrust. The lower the mass flow rate, the lower will be the power required for the propellant to reach the desired temperature. However, it can be observed in table 4.5 that with an increase in temperature, the change in enthalpy increases as well. Hence, it can concluded that a higher chamber temperature is preferred due to the lower power required to heat up the propellant even though the thrust efficiency decreases due to viscous losses until 1100 K. Beyond this temperature the change in enthalpy drastically begins to increase which implies higher power required to be transferred to heat up water. The drop is no more than 2.3 % between the lowest and highest temperatures in the table.

4.2. Materials

From the materials survey done in [21], it was determined that molybdenum is the most suitable material for the heat exchanger cavity. The major concern regarding the design of a heat exchanger is insulation. It will be seen later that insulation of the heat exchanger is not the only component to be taken into account but also insulating the optical fiber at the receiver interface is critical. Therefore, the properties of the materials considered for the heat exchanger and insulation are listed in the table below.

Material	**Density [Kg /m3]**	**Thermal conductivity [W/m K]**	**Specific heat [J/Kg.K]**	**Emiss-ivity [-]**	**Tensile Strength [MPa]**	**Refractive Index**
Cavity Material						
Molybdenum [38]	10300	107	277.16616	0.271	324	-
Silicon Carbide [21]	3210	60	670	0.83-0.96 (422.15 K -922.15 K)	540	-
Cavity - Insulation Material						
Fibermax Blanket @ 1873 K [39]	130	0.25	1246	-	0.06	-
Pyrogel XT @ 923 K [40]	200	0.014	1000	-		-
Phenolic Foam	35	3.80	-	-	80	-
Optical Fiber Material						
Silica (core) [21]	2203	1.38	703	0.88 (1366.15 K)	155	1.458965
Hard polymer (cladding) [4]	2200	0.25	1256	-		1.3651
Tefzel (Buffer) [41]	1700	0.238	1172	0.3	830	1.398
Fiber - Receiver Coupling Material						
Quartz (collet)[42]	2200	1.4	720	0.93	67	1.5

Table 4.6 continued from previous page

Material	Density [Kg /m3]	Thermal conductivity [W/m K]	Specific heat [J/Kg.K]	Emiss-ivity [-]	Tensile Strength [MPa]	Refractive Index
SiO2-TiO2 glass [43]	2200			0.081		
Alumina [7]	3600	8	750	0.69-0.45 (700.15 K - 1366.15 K)	120	-
Zirconia [7]	5600	3	460	0.62-0.45 (700.15 K- 1366.15 K)	750	-

Table 4.6: Material properties

The thickness of the insulating material (Pyrogel) required to insulate the heat exchanger from the surrounding components can be seen below in the plot. The following plot has been generated by thermally modelling a block of pyrogel in Abaqus. The material properties were given as input as listed in table 4.6 and surface temperature on one side was maintained at 1100 K. As can be seen in plot above, a thickness of 1.2 cm would be needed to insulate a heated body at 1100 K to 300 K which is within the working condition of the fibers and keeps it well insulated from the rest of the sub-systems and components.

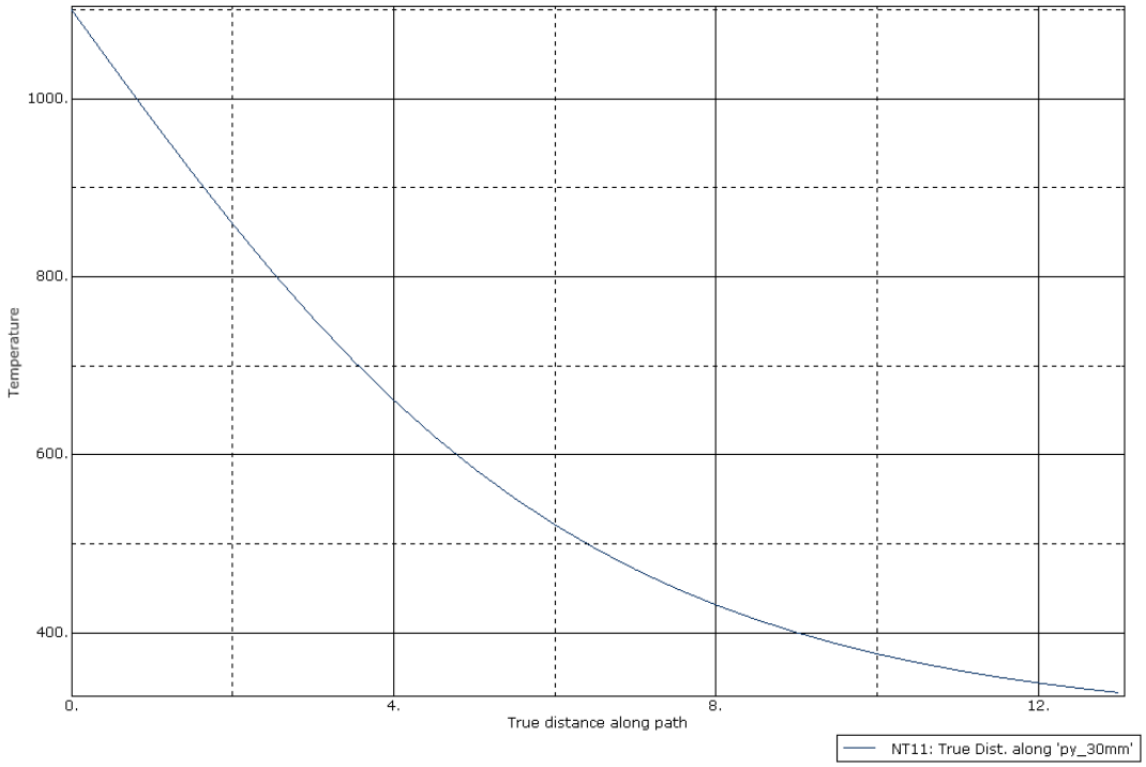

Figure 4.3: The insulation thickness vs temperature for Pyrogel

4.3. Heat Exchanger

Before diving into the preliminary design of the heat exchanger, it is important to state that the dimensioning of the propellant channels of the heat exchanger are dependent on the following parameters:

1. The nozzle height of the thruster. This adds a geometrical constraint on the flow channel height throughout.
2. Propellant properties during phase change with respect to temperature.
3. Convective heat transfer coefficient and its dependency on cavity and channel wall temperature.

One of the main geometrical constraints on the heat exchanger and variables is the nozzle depth which ideally must be same as the channel height.

Heat Exchanger dimension parameters			
Sr. No	**Symbol**	**Variable Parameter**	**Criterion**
1	HE_h	Heat exchanger height	This parameter will vary depending on the cavity height and wall thickness.
2	HE_w	Heat exchanger width	The HE width also depends on the number of flow channels used but must also be greater than 3 times of the nozzle width.
3	HE_l	Heat exchanger Length	The heat exchanger (excluding the thruster) length will be dependent on the channel length required to get heated.
4	C_h	Inner cavity height	The cavity height is a variable and depends on the intensity of rays received from the optical fibers. The starting height value will be taken from literature.
5	C_w	Inner cavity width	The cavity width is constrained to be atleast 3 times greater or equal to the nozzle throat width to ensure that the flow remains subsonic before it reaches the nozzle throat.
6	C_l	Inner cavity length	The length.
7	t	Wall thickness	The thickness of the wall is dependent on the ultimate stress of the material and chamber pressure.
Channel dimensions			
8	L_{ch}	Propellant channel length	This parameter will be constant throughout to compare thermal performance.
9	H_{ch}	Propellant channel height	The channel height and nozzle height must be constant and hence an iterative process will be followed this parameter.
10	W_{ch}	Propellant channel width	This parameter will be estimated depending on the aspect ratio and affect of hydraulic diameter of the channel on the flow.
11	H_l	Propellant channel length	The length required to heat up the propellant to a 1000 K. The requirements from the table number states that the length must not exceed 5 cm.

Table 4.7: Heat Exchanger dimension parameters

4.3.1. Flow Regime in Rectangular Micro-channel

Several papers [44][45] elaborate on the experimental results of heat transfer and pressure drop through micro-channels. It has been concluded that the convective heat transfer in micro-channels is comparatively more complex than for large sized channels and the conventional theory is not valid for channels with hydraulic diameters less than 1 mm as the Reynolds number and the friction factors for the transition from laminar flow to turbulent flow was found to be much lower than the conventional theory for a large channel. The Reynolds number for the flow through the channels are computed using the equation 3.5.

When considering heat transfer in a microchannel, we should not only consider laminar or turbulent flow but also whether the boundary layer is fully developed or whether we are dealing with the entrance region of the tube. In the latter case, we should take into account that the Nusselt number varies with the distance travelled in the microchannel. The Nusselt number depends on several factors namely: channel geometry, boundary conditions considered (either uniform wall temperature or constant heat flux), and the flow regime (fully developed flow, simultaneously developing flow, thermally developing flow, transitional flow). There are several correlations available for rectangular microchannels in literature but the following are used for a four-sided heated wall.

- **Fully developed laminar flow**
  Poh-Seng, et al. [46] investigated a four-sided heated rectangular channel for aspect ratios from 1 to 10 assuming constant heat flux and laminar flow of water. The proposed correlations in the above mentioned paper have shown comparisons with past experimental and computational results and confirm accurate predictions of the thermal performance for the given microchannel geometry. The Nusselt number for a fully developed laminar flow can be expressed as

$$Nu = 8.235\left(1 - \frac{2.0421}{\alpha} + \frac{3.0853}{\alpha^2} - \frac{2.4765}{\alpha^3} + \frac{1.0578}{\alpha^4} - \frac{0.1861}{\alpha^5}\right) \tag{4.23}$$

$$Z^*_{th} = -1.275 \times 10^{-6}\alpha^6 + 4.709 \times 10^{-5}\alpha^5 - 6.902 \times 10^{-4}\alpha^4 + 5.014 \times 10^{-3}\alpha^3 \\ -1.769 \times 10^{-2}\alpha^2 + 1.845 \times 10^{-2} + 5.691 \times 10^{-2}$$

$$Z^* = \frac{L_{ch}}{D_h\ Re\ Pr} \tag{4.24}$$

  Here Z^*_{th} is defined as the dimensionless thermal entrance length and α is the aspect ratio of the channel. The above relation is used to differentiate between the flow regimes, i.e., from developing to a fully developed flow. The equation 4.23 is only valid for $Z^* > Z^*_{th}$

- **Thermally developing laminar flow**
  The equation valid for a thermally developing flow is given by the following relation for the conditions $1 \leq \alpha \leq 10, Z^* < Z^*_{th}$.

$$Nu = \frac{1}{C_1 (Z^*)^{C_2} + C_3} + C_4 \tag{4.25}$$

$$C1 = (-3.122 * 10^{-}3 * \alpha^3) + (2.435 * 10^{-}2 * \alpha^2) + (2.143 * 10^{-}1 * \alpha) + 7.325; \tag{4.26}$$

$$C2 = 6.412 * 10^{-}1; \tag{4.27}$$

$$C3 = (1.589 * 10^{-}4 * \alpha^2) - (2.603 * 10^{-}3 * \alpha) + (2.444 * 10^{-}2); \tag{4.28}$$

$$C4 = 7.148 - (1.328 * (10/\alpha)) + (1.515 * (10/\alpha^2)) - (5.936/\alpha^3); \tag{4.29}$$

- **Fully developed turbulent flow**
  Due to the lack of accurate relations for a four-sided heated rectangular microchannel in literature especially with water flow, three-side heated channel wall correlations are considered. Amirah, et al. [8] investigated 2D and 3D models of one side and three sides heated rectangular walls, and it can be concluded from one of its results that show the variation of the local Nusselt number along the channel, that the difference in the Nusselt number between the two cases is minor. The Nusselt number for both cases is not quantitatively defined but the plot has been added to the appendix C. Hence, for a fully developed turbulent flow, the Gneilinski equation is used [47].

$$Nu_{fd,\,Tur} = \frac{(f/2)(Re - 1000)Pr}{1 + 12.7\sqrt{f/2}(Pr^{2/3} - 1)} \tag{4.30}$$

  where the fanning factor f is defined as

$$f = (1/4)[1.82log(Re)–1.64]^{-2} \tag{4.31}$$

  The above equation is valid for 0.5 ≤ Pr ≤ 2000 and 2300 ≤ Re ≤ 5e6.

- **Thermally developing turbulent flow**
  As the flow also thermally develops past the entrance region, the relation for thermally developing turbulent flow is given by Zukauskus, valid for for $4000 \leq Re_{D_h} \leq 5 * l0^5$, $0.7 \leq Pr \leq 1.0$; and $L/D_h \geq 0.06$ [47].

$$\frac{Nu_{D_h}}{Nu_{fd,\,Tur}} = 1 + 0.48\left(\frac{L_{ch}}{D_h}\right)^{-0.25}\left[1 + \frac{3600}{ReD_h\sqrt{\frac{L_{ch}}{D_h}e^{-0.17L_{ch}/D_h}}}\right] \tag{4.32}$$

  where $Nu_{fd,\,Tur}$ is the fully developed Nusselt number. Thermally developing turbulent flow for Prandtl numbers $0.6 \leq Pr \leq l0^5$ and Reynolds numbers $2300 \leq Re_{D_h} \leq l0^6$ is given by the following Gneilinski equation.

$$\frac{Nu_{D_h}}{Nu_{fd,\,Tur}} = 1 + \left(\frac{D_h}{L_{ch}}\right)^{2/3} \tag{4.33}$$

As the STP system aims to heat up the receiver cavity up to 1100 K, the water flowing through the micro-channel will consequently boil and eventually vaporize. Hence, the preliminary length calculations have divided into three regions, namely, single-liquid phase region, two-phase flow region, and single-gas phase region. The detailed calculation is done in the next section.

4.3.2. Pressure Loss in Rectangular Micro-channels

One of the criteria for the system channel trade-off is the amount of pressure drop in the channels of the heat exchanger. Pressure losses in internal flows consist of minor and major losses. The major losses in a micro-channel are mainly due to the friction between the channel walls and the flow, whereas, the minor losses consist of pressure drops due to bends, the inlet, and exit. The pressure drop equation can be determined using the following equation:

$$\Delta P = \Delta P_c + \Delta P_{sp,d} + \Delta P_{sp,f} + \Delta P_{tp} + \Delta P_b + \Delta P_e \tag{4.34}$$

Here, ΔP_c is the loss due to contraction at the inlet, ΔP_e is the loss due to expansion at the exit, $\Delta P_{sp,d}$ and $\Delta P_{sp,f}$ are the losses due to single phase flow in the developing and fully developed regions and ΔP_{tp} is the loss due to two phase flow. ΔP_b is the pressure drop due to 90 degree bends. At this conceptual stage, the inlet manifold for the propellant inflow and outlet section of the channels are not considered.

Single phase pressure drop

In a fully developed laminar flow, the mass flow rate and the pressure drop are proportional to each other. The relationship is not as simple in the case of turbulent flow. For a channel length for a developing region ($L_{sp,d}$), hydraulic diameter (D_h) and friction factor $f_{sp,d}$, the pressure drop is described as

$$\Delta P_{sp,d} = \frac{2 f_{app} L_{sp,d} U^2 \nu_f}{D_h} \tag{4.35}$$

$$f_{app} = \frac{1}{Re_{sp,d}}\left[3.44(L^+_{sp,d})^{-0.5} + \frac{1.089/(4L^+_{sp,d}) + f_{sp,d}Re_{sp,d} - 3.44(L^+_{sp,d})^{-0.5}}{1 + 1.31 \times 10^{-4}(L^+_{sp,d})^{-2}}\right] \tag{4.36}$$

$$L^+_{sp,d} = \frac{L_{sp,d}}{Re_{sp,d} D_h} \tag{4.37}$$

$$f_{sp,d}Re_{sp,d} = 24(1 - 1.355\beta + 1.947\beta^2 - 1.701\beta^3 + 0.956\beta^4 - 0.254\beta^5) \tag{4.38}$$

$$Re_{sp,d} = \frac{U D_h}{\mu_{sp,d}}\beta = \frac{W_{ch}}{H_{ch}} \tag{4.39}$$

For a fully developed region, the pressure drop can be estimated using the following correlation

$$\Delta P_{sp,f} = \frac{2 f_{sp,f} L_{sp,f} U^2 \nu_f}{D_h} \tag{4.40}$$

$$f_{sp,f}Re_{sp,f} = 24(1 - 1.355\beta + 1.947\beta^2 - 1.701\beta^3 + 0.956\beta^4 - 0.254\beta^5) \tag{4.41}$$

$$Re_{sp,f} = \frac{U D_h}{\mu_{sp,f}}\beta = \frac{W_{ch}}{H_{ch}} \tag{4.42}$$

Two phase pressure drop

The thermodynamic equilibrium quality X_e for vapor is between 0 to 1, and so the mean gas quality is taken as 0.5. The two phase flow pressure drop can be expressed in terms of two components, namely, accelerational ($\Delta P_{tp,a}$) and frictional ($\Delta P_{tp,f}$) components. The Lockhart–Martinelli correlation model for laminar liquid and laminar vapor can be expressed as [48] [49]:

$$\Delta P_{tp,f} = \frac{L_{tp}}{X_{e,tp}} \int_0^{X_{e,tp}} \frac{2 f_f U^2 (1 - X_e)^2 \nu_f}{D_h} \phi_f^2 dX_e \tag{4.43}$$

$$f_f Re_f = 24(1 - 1.355\beta + 1.947\beta^2 - 1.701\beta^3 + 0.956\beta^4 - 0.254\beta^5) \tag{4.44}$$

$$Re_f = \frac{U(1 - X_e) D_h}{\mu_f} \tag{4.45}$$

$$\phi_f^2 = 1 + \frac{C}{X_{vv}} + \frac{1}{X_{vv}^2}, C = 5 \tag{4.46}$$

$$X_{vv} = \left(\frac{\mu_f}{\mu_g}\right)^{0.5}\left(\frac{1 - X_e}{X_e}\right)^{0.5}\left(\frac{\nu_f}{\nu_g}\right)^{0.5} \tag{4.47}$$

The Lockhart–Martinelli correlation model for laminar liquid and turbulent vapor can be expressed as:

$$\Delta P_{tp,f} = \frac{L_{tp}}{X_{e,tp}} \int_0^{X_{e,tp}} \frac{2 f_f U^2 (1 - X_e)^2 \nu_f}{D_h} \phi_f^2 dX_e \tag{4.48}$$

$$Re_g = \frac{G X_e D_h}{\mu_g} \tag{4.49}$$

$$\phi_f^2 = 1 + \frac{C}{X_{vt}} + \frac{1}{X_{vt}^2}, C = 12 \tag{4.50}$$

$$X_{vt} = \left(\frac{f_f Re_g^{0.25}}{0.079}\right)^{0.5} \left(\frac{1 - X_e}{X_e}\right) \left(\frac{\nu_f}{\nu_g}\right)^{0.5} \tag{4.51}$$

The acceleration pressure drop component arises due to the momentum of the propellant flow gained due to vaporization. This component can be determined using the following equation:

$$\Delta P_{tp,a} = \left(\frac{\dot{m}}{A_{ch}}\right)^2 \left[\frac{X_{e,tp}^2}{\alpha_e}\left(\frac{\nu_f}{\nu_g}\right) + \frac{(1 - X_{e,tp})^2}{1 - \alpha_e} - 1\right] \tag{4.52}$$

$$\alpha_e = \frac{1}{1 + \left(\frac{1 - X_{e,tp}}{X_{e,tp}}\right)\left(\frac{\nu_f}{\nu_g}^{2/3}\right)} \tag{4.53}$$

The total pressure drop through the channel can be estimated by summing the pressure drop due to single phase water flow at the inlet (liquid), two-phase boiling flow, acceleration pressure drop and single phase vapor flow at the channel outlet (gas) as follows:

$$\Delta P_{total} = \Delta P_{sp,l} + \Delta P_{tp,f} + \Delta P_{tp,a} + \Delta P_{sp,g} \tag{4.54}$$

4.3.3. Channel Wall Thickness

As the micro-channels are considered to be non-circular pressure vessels, the wall thickness can be calculated using the equation for rectangular pressure vessels 4.56 [50].

$$S_m = S.F \frac{P \,.\, h_{ch}}{2.t_1} \tag{4.55}$$

$$S_m = S.F \frac{P \,.\, w_{ch}}{2.t_2} \tag{4.56}$$

Here S_m is the membrane stress due to pressure and must not exceed the maximum allowable yield stress of the material. For molybdenum, the ultimate yield stress is 415 MPa, i.e. before the material begins to deform. P is the pressure that the channel must withstand. The channels will be designed to tolerate a pressure of 5 bar and a safety factor $S.F$ of 3 is applied. h_{ch} and w_{ch} are the channel height and width respectively. t_1 and t_2 are the required wall thickness values corresponding the stress acting on channel height and width of the pressure vessel respectively. The dimensions of the channel for varying aspect ratios have been determined in the detailed design chapter 5.

4.3.4. Cavity Dimensioning

The length of the receiver cavity will be the same as the channel length of the heat exchanger. To determine the thickness of the cavity walls, three important factors that need to be taken into consideration [51] are the ability of the cavity to withstand the operating pressure, stresses due to the pressure in the micro-channels and heat absorbed that needs to be conducted from the wall to the propellant. For the baseline design and preliminary thermal study, the corrugation of the cavity surface is considered to be equilateral with the base dimension between the spacing between two channels.

The dimensioning of the rectangular cavity wall thickness will be done by following the American Society of Mechanical Engineers (ASME) Boiler and Pressure Vessel Code, Section VIII, that provides rules, analyzing guidelines and examples of evaluating rectangular pressure vessels [50]. The requirements of the pressure vessel are to operate at a pressure of 5 bar and sustain a wall temperature of at least 1400 K and conduct heat to the flow path of the heat exchanger. According to the code, the design pressure must be 1.5 times of the operating pressure and therefore, the cavity has been designed to operate at 7.5 bar. The cavity and channel wall thickness is computed to be 4.5e-4 m for the above-mentioned conditions. The cavity height is considered to be 5 mm for preliminary ray optics modeling. This value is taken from a study done with 6 optical fibers transmitting a total of 50 W power into a closed cylindrical cavity by Henshall. During the ray-tracing study in the above mentioned research, the highest intensity on the surface of the cavity wall has been reported to be at a cavity length of 5 mm [2]. A parametric study of the cavity height and the intensity distribution will be conducted in chapter 6, section for the final design.

4.4. Optical Fiber Cable

Optical fibers have been found to have a wide range of applications over the years. From being extensively used in the communication industry for the transmission of information to being used in bio-medical applications such as endoscope instruments, advanced imaging techniques, etc. This section will focus on the application of optical fiber cables to transmit sunlight from the concentrator focal point to the propellant heating cavity of the STP system. Its application for the solar thermal propulsion and benefits are discussed in chapter 3, sub-section 3.1.1. A major benefit offered by the optical fibers is that it decouples the thruster from the concentrator, eliminating design constraints imposed by conventional systems that the concentrator can remain pointed at the sun at all times, and offers a degree of flexibility.

In this section, the optical fiber selection is made based on their optical and physical properties. And as seen in the previous section, the concentrator design completely depends on the fiber optic properties and geometry, and so this section will also elaborate on the preliminary design of the concentrator. Apart from defining the geometrical constraints and intrinsic attenuation of the optical fiber cable, the performance of the fiber cable over the cable length, ray tracing inside the receiver cavity due to the optical fiber and coupling concepts with the concentrator and receiver will be discussed.

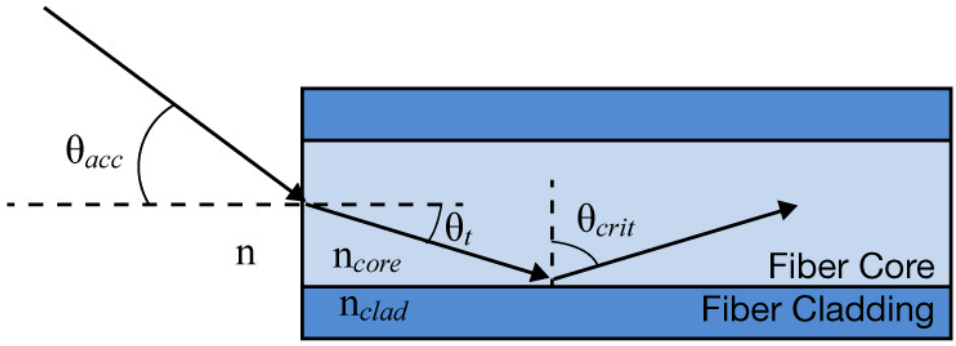

Figure 4.4: Total internal reflection phenomena in an optical fiber [4]

Optical fibers are the components that guide light through a solid medium by utilizing total internal reflection (TIR) within the medium. For the phenomena of TIR to occur, the angle of incidence entering the fiber must be less than the acceptance angle ($sin\ \theta_{acc}$) of the fiber which can be obtained using Snell's law:

$$sin\ \theta_{acc} = \frac{\sqrt{n_{core}^2 - n_{clad}^2}}{n} \tag{4.57}$$

Here n_{core}^2 is the refractive index of the core and it must be higher than the refractive index of the cladding (n_{clad}^2) such that the critical angle is maintained and TIR takes place. n is the refractive index of the surrounding medium and it is equal to 1 for vacuum and air. The acceptance angle of an optical fiber is usually indicated by a dimensionless number known as the numerical aperture and it is mathematically expressed as

$$NA = n\ sin\ \theta_{acc} \tag{4.58}$$

4.5. Transmission Efficiency and Attenuation

Before we look into the optical fibers suitable for the purpose of this study, it is important to first identify the sources of attenuation and its effect on the transmission efficiency of solar energy. There are several ways in which the transmitting energy can be lost: Attenuation due to internal scattering and absorption in the core material, leaks between the core and cladding interface and losses at the entrance and exit of the fiber [52].

4.5.1. Optical Fiber Efficiency

For a length of 1 m, NA - 0.5 and a core diameter of 1 mm, the efficiency of the fiber due to wavelength dependent attenuation is about 0.9978 using the following equation.

$$\eta_{of} = 10^{\frac{(-L*dB)}{10}} \tag{4.59}$$

Here dB is the attenuation (dB/Km) over a range of wavelength (nm) and L is the length of the optical fiber. Henshall [2] assumed a value of 80% for the calculation of the optical fiber performance for its application in solar thermal propulsion. (The power transmitted using 6 optical fibers with a total diameter of 1mm (core diameter 0.76mm) and NA - 0.66 is about 50 W- this doesn't match with the equations used in this thesis and thus the assumption from this paper is not considered). Also, as the core diameter and NA are not the same, the results from the paper are not taken into account. However, Takashi's experimental results for the efficiency of a 1mm diameter optical fiber

with NA of 0.48 shows a fiber transmission of 77% for a length of 10 m. The predicted efficiency for a Space-Based Operational System is however estimated to be 90% [53].

Even though the transmission power consequently reduces with increase in the length of the optical fiber, 90% efficiency will be considered for the purpose of this thesis for conservative results (Using 1m optical fiber - hence higher transmission efficiency compared to 10m). Both these papers have tested the working temperature of optical fibers of 1mm diameter and have shown that the fiber core works perfectly fine at 1000 K.

4.5.2. Sources of Attenuation

The optical fiber performance can severely be affected by several external influences. These external parameter induced losses can be referred to as attenuation and can highly impact the total output power at the end of the optical fiber if not taken into account. The sources of losses can widely be classified into wavelength dependent losses, temperature dependent losses, geometrical setup losses, and losses due to the materials used. Some of the minor and major loss sources, its effect on the performance and methods to prevent the losses have been listed below.

Macro Bend

Losses incurred due to the bending of the optical fiber. When the fiber has a bend radius smaller than the limit imposed on it, the total internal reflection through the fiber becomes difficult. At incident angles higher than the critical angle light escapes the fiber leading to a high loss in the power being transmitted. Other than restricting the bend radius of the fiber, double clad fiber can be used to reduce the risk of bend loss. It ensures a higher critical angle between the two claddings than with the core and the first clad interface. This makes sure that the light escaping the core remains within the outer cladding. Basically, for a large bend radius, the bend losses identified are small and vice-versa. The maximum limit of the bend radius for the optical fiber will depend on the CubeSat unit volume available. For the considered 4U of CubeSat volume available for the propulsion system, it will then depend on the configuration of the CubeSat units or the desired stacking arrangement. In any case, the lower limit of maximum bend radius would be 5 cm considering 1U of CubeSat for storing. This limit is applicable if the optical fibers are stored in coiled form.

A quick analysis of the transmittance of power through the optical fibers was conducted for varying numerical aperture, core diameters and bend radius at a bend angle of 45 degrees in Comsol as shown in the figure 4.5. The maximum transmission can be achieved when the optical fiber is straight as then the bend loss tends to zero i.e the bend angle is 180 degrees. In the case of 90-degree bends, the losses will reduce as the bending radius increases.

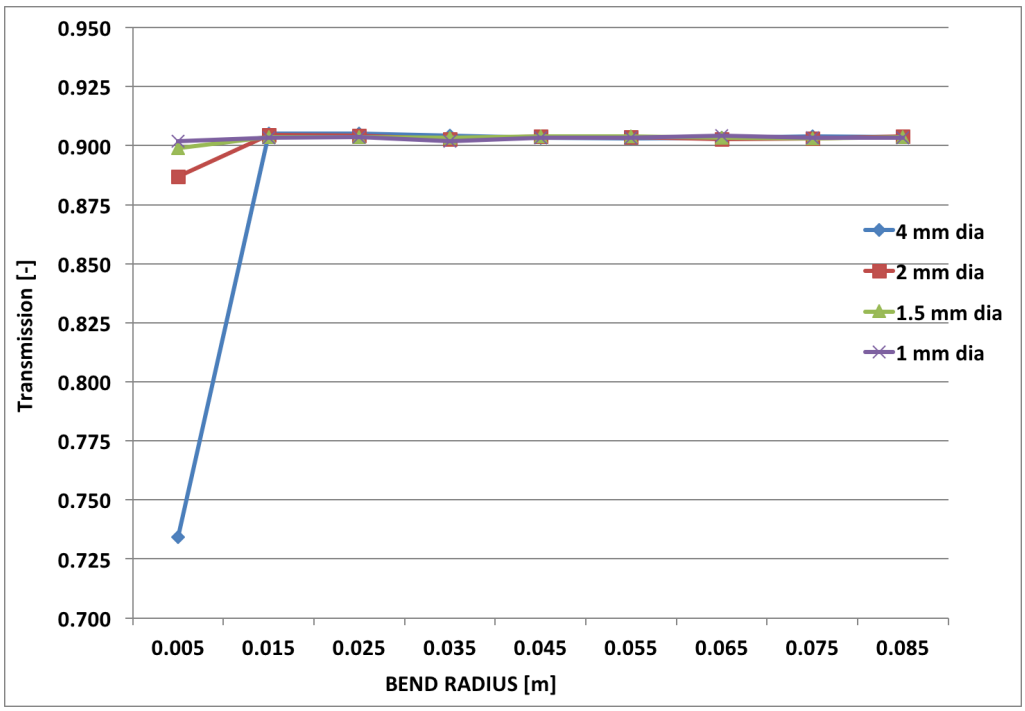

Figure 4.5: Transmission efficiency of power vs bend radius for optical fibers with core diameters of 1 mm, 1.5 mm, 2 mm and 4 mm

The transmittance of the optical fiber is determined by computing the total power deposited at the end surface of the fiber based on the total input power of the rays. The plot above shows the effect of the bend radius on the transmission of the power for different core diameter. The input power for the fiber has been set to 7.6731 W for all cases. It can be observed that for a bend radius less than 15 mm, the transmission efficiency for optical fibers with core diameter 2 mm and 4 mm drastically drops as compared to the fibers with diameter 1 mm and 1.5 mm. This simple analysis proves that to prevent bend losses in fibers, an optimal minimum bend radius exists for every core diameter.

It will later be noticed that in table 4.8 the minimum bend radius given by the manufacturer for the similar core diameter fibers is much higher than the one seen in the plot above. The low bend radius attained in the analysis can be attributed to neglected attenuation of multiple sources stated in this section and physical damages/tears to the material during bends, while the manufacturers have tested the fibers and provided concrete specifications for the products.

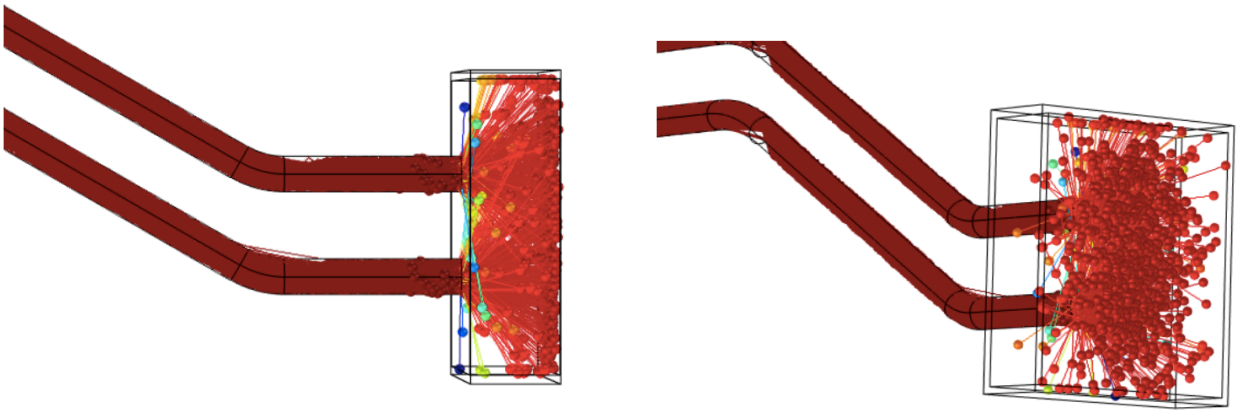

(a) Side view of two optical fibers with bending

(b) Isometric view of two optical fibers with bending

Figure 4.6: Projection of rays into a rectangular closed cavity through bending in optical fibers

The reason why this source is given attention is because it plays an important role in storing the fibers in the available space of the satellite. As we are dealing with CubeSat units, a maximum of 20 cm length may be available for the bend diameter of the fiber. Since the minimum bend radius for fibers with larger diameters is quite high (for efficient transfer), an optimal selection of the optical fiber will be made in section 4.5.2 such that it offers a balance between the performance and losses involved.

Micro Bend Loss

Micro bends and bumps associated with the internal geometry of the fiber, i.e the layers of core and cladding can deteriorate the performance of the fiber as well.

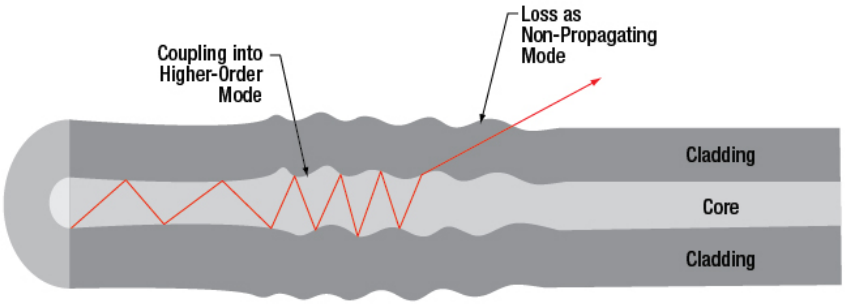

Figure 4.7: Attenuation due to microbends [4]

These micro-irregularities are caused due to physical stress and during manufacturing and unlike macro bend losses, these are generally permanent defects. What these bumps or uneven surfaces do is that it disturbs the ideal condition required for total internal reflection by forcing a transition from propagating mode into a high-order mode which is then coupled into a non-propagating mode. This mode enables leakage of light from the fiber.

Radiation

Long-term exposure of the fibers to radiation have a visible impact on it. Radiation Induced Attenuation (RIA) is caused due to the high energy impact on the fibers and disturbing the bonds of

the fiber material. This leads to the formation of a color center and can also be the cause of change in the refractive index of the materials. To reduce the effect of radiation, radiation resistant fibers are preferred.

Light Scattering

Scattering of light accounts for one of the major losses in optical fibers. Now, these losses can occur due to several external and internal influences such as a change in the refractive index of the material, impurities, bubbles, or particles in the material of the core, etc. Presence of these impurities on the fiber tip cause huge losses in the transmission of the input power by scattering. These losses can be minimized by proper handling of the fiber, cleaning and proper storage.

Cladding Modes and Scratches

Any damage or tears to the core and cladding of the fiber increases the risk of fiber breakage. The loss due to these damages is generated due to the undisrupted condition needed for total internal reflection. This loss can be prevented by using an apt buffer and jacket as the outer protecting layer on the fiber. These materials are usually ethylene tetrafluoro ethylene or partially fluorinated copolymers, for example, Teflon, Tefzel, etc. These materials are characterized by a low thermal conductivity and high flexural strength.

High temperatures

When the fibers are exposed to temperatures above and below its operation range, it has a significant effect on the polymer materials used. This, in turn, induces index and phase change in polymers, causing stiffening and embrittlement of the material. This adds to the attenuation and reduces the flexibility of the fiber. High-temperature resistant materials should be chosen when selecting optical fibers.

As fibers on a spacecraft can be subjected to a wide range of temperatures (-150 C to +120 C) and especially for the STP application which may reach up to 1000 K, attenuation due to high temperature becomes a critical factor. In order to protect the fiber from getting damaged and to ensure it stays within the working conditions, a detailed study of the optical fiber's thermal model has been done. This helps in determining the output and surface temperature and the insulation thickness and material apt for the purpose.

Temperature dependence of optical materials can be calculated using Sellmeier equation [54]:

$$n_T = n_R + \frac{dn}{dT} * (T - T_{ext}) \tag{4.60}$$

Here the dn/dT is the temperature coefficient of the refractive index and is about 12.9 x 10-6 [1/K] for silica which is the core material for optical fibers. n_R and n_T are the refractive indices at room temperature and new temperature respectively.

Solarization or Photodarkening

This damage mechanism is caused when the fiber is exposed to intense UV light (<300 nm) or short-wavelength visible light. This exposure causes the formation of excited electron energy states that add to the loss by increasing the absorption of light in the fiber. The cause behind photodarkening is mostly unknown but using optical fibers with low hydroxyl ions and fibers doped with fluorine have shown to resist photodarkening. However, over a long period of time, the attenuation increases for the mentioned wavelength spectrum. Since this effect takes place outside the wavelength range (300 nm - 2200 nm) considered for this study, this can be neglected.

Most of these sources of attenuation are either mentioned in the specifications data sheet of the optical fibers or it can be determined by experimentally testing the fibers. The losses due to intrinsic parameters such as micro bends, scattering due to surface irregularities and material interfaces are not entirely in our control since these defects originate from manufacturing, whereas, the losses due to external influences can be handled or diminished by taking the measures mentioned above.

The total loss due to the above mentioned factors cannot be quantified without proper testing. Therefore, for the purpose of this thesis, the attenuation (dB/Km) over a range of wavelength (nm) plot is used for the selected optical fiber as provided by the manufacturer. The plot can be referred to in appendix A.

4.6. Optical Fiber Candidates

For an optical fiber to be suitable for solar radiation transmission, the fiber must have the following properties:

- Step-index optical fiber (multimode)
- Large numerical aperture, low OH. A high level of hydroxyl ions can be problematic as it indicates the abundance of water vapor during the manufacturing of the optical fibers and could give rise to undesirable vibrational absorption during transmission [2].
- It must be high temperature, radiation and solarization resistant.
- The fiber optics must have a low attenuation over the solar spectrum

A multimode step-index optical fiber is required as it allows the light rays to have multiple trajectories along the length of the fiber. This design leads to a broader output pulse with respect to the input. Geometrically, the step-index fiber results in a zig-zag path due to the acute change in refractive index between the core and cladding.

Apart from the selection requirements mentioned above, it must be noted that the concentrator design is heavily dependent on the core diameter of the optical fiber as elaborated in section 4.7. The dependency of the concentrator aperture on the image size, which is basically the core diameter of the optical fiber at the focal spot in this case, demands on selecting an optical fiber with large core diameter, large numerical aperture and small attenuation value for an effective transmission.

Another important selection criteria, which deals with the system integration and storage, is the bend radius of the optical fiber. The bend radius of an optical fiber is defined as the minimum bending that the fiber can withstand before it faces permanent damage or breaking occurs. This parameter is of utmost importance for the fiber to remain efficient and not incur further attenuation during packaging and operation. The table 4.8 presents some of the feasible optical fibers in the market. The selection will be done in section 4.7 once the performance associated with each fiber property is studied.

Table 4.8: Optical Fiber Candidates

Fibre/ Product name	Manufa-cturer	NA	Temp Range [°C]	Accept-ance half angle	Bend radius (Long term) [mm]	Core Dia [µm]	Clad Dia [µm]	Buffer Dia [µm]	Ref.
FLU	Polymicro	0.66	–10 to +160	41.3°	-	750 ± 10	-	-	[55]
Ultra Low - OH FI (FIP600-660710)	Polymicro	0.22 ± 0.02	-65 to +300	12.7°	>= 132	600 ± 10	660 ± 10	710 ± 10	[56]
Anhydro-guideTM (AFS)	FiberGuide Industries	0.26	-40 to + 85	15 °	>= 44	200 ± 10	220 ± 4	320 ± 16	[57]
Optran® UVWFS	Ceram Optec	0.28 ± 0.02	-190 to 350	16.2 °	>= 66	220	233.2	-	[58]
OPTRAN ULTRATM	Ceram Optec	0.37 ± 0.02	-190 to + 400	21.72 °	>=141	600	660	710	[59]
		0.44 ± 0.02	-40 to 130	26.1 °	>=180	600	660	800	[59]
		0.53 ± 0.02	-40 to 100	32 °	>=180	600	660	800	[59]
FT200EMT	Thorlabs, Inc	0.39	-40 to 150	22.95°	>=100	1000 ±15	1035 ± 15	1400 ± 50	[4]
		0.50	-40 to 150	30 °	>=80	1000 ± 15	1035 ± 15	1400 ± 50	[4]
		0.50	-40 to 150	30 °	>=150	1500 ± 30	1550 ± 31	2000 ± 100	[4]

4.7. Concentrator Design

For the purpose of coupling a concentrator to the optical fiber, the following requirements must be met for optimal design and transmission of solar radiation:

- The rim able of the concentrator must be greater than/equal to the acceptance angle of the fiber optics which is in turn defined by its numerical aperture.

In 2005, the application of fiber optics in STP systems was studied by Paul R. Henshall et al. and it was observed that it has a suited application in small satellites. Also, fiber optics facilitates replacement of large concentrators with multiple small concentrators and thus lowering the system mass as a lower support structural mass is needed [2].

As the scope of the thesis lies in designing the heat exchanger and receiver-cavity of the STP system, only a high-level study of the concentrator design and analysis has been conducted. The inclusion of the optical fibers put no constraints on the rigidity and position of the concentrator and but the system requirement constrains the concentrator to be only inflatable for stacking in the available volume of the CubeSat. From a detailed study done by the author of [20], it has been concluded that the parabolic mirror seems to offer the highest concentration ratio which outperforms the rest.

For the designing of a parabolic concentrator, the following equations are applicable. The height (H) and the focal length (f) of the concentrator are given by the following relations:

$$H = \frac{d_c^2}{16f} \tag{4.61}$$

$$tan\left(\frac{\phi_{rim}}{2}\right) = \frac{1}{4\left(\frac{f}{d_c}\right)} \tag{4.62}$$

Here d_c is the concentrator diameter, θ_r is the rim angle of the concentrator. Ideally, the rim angle must be equal to or less than the acceptance angle of the optical fiber.

$$\phi_{rim} \leq \theta_{max} \tag{4.63}$$

The acceptance angle for the selected optical fiber can be determined from the equation 4.57 and is found to be 30°.

As mentioned above, the diameter of the concentrator depends on the image size of the optical fiber, it can be determined using the following equation.

$$d_{of} = \frac{d_c\ sin(\theta_s + \phi_{shading})}{sin(\phi_{rim})cos(\phi_{rim} + \theta_s + \phi_{shading})} \tag{4.64}$$

Here θ_{sh} is the shading angle on the concentrator due to the optical fiber. It is assumed that the shading angle is 0° such that the fiber is perfectly aligned at the principal axis and placed at the focus of the concentrator. θ_s is the solar half angle of the incident solar radiation on the mirror, 0.267° and the optical fiber tip size is denoted by d_{of}. For the selected optical fiber, the core diameter is 1 mm and hence the value of d_{of}. Once the concentrator diameter is calculated using equation 4.64, the focal length and height of the concentrator can be determined with equation 4.62 and 4.61 respectively. Subsequently, the concentration ratio can be estimated which is defined as the ratio of the concentrator area to the receptor area of the fiber.

$$CR = \left(\frac{d_c}{d_{of}}\right)^2 = \frac{sin^2(\phi_{rim}) * cos^2(\theta_s + \phi_{rim} + \theta_d))}{sin^2(\theta_s + \theta_d)}; \tag{4.65}$$

As can be seen from the equation, the concentration ratio is clearly dependent on the rim angle and θ_d, which is the measure of angular error of the mirror. Once the concentrator diameter is calculated, the power input at the inlet of the optical fiber can be estimated using the equation 5.29 and the power output using equation 5.30 defined in chapter 5 in section 5.3 which focuses on the thermal model of the optical fiber. The power output for varying core diameter of the optical fiber has been studied using the above mentioned equations for a fiber length of 1 m.

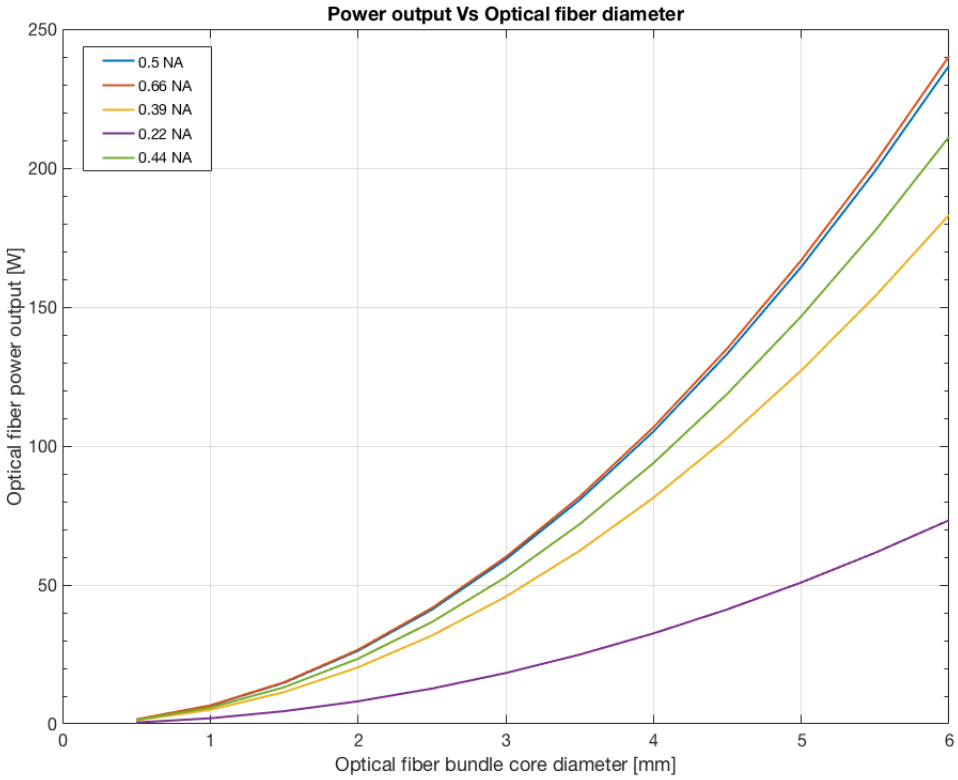

Figure 4.8: Power output in optical fibers of different numerical apertures with varying core diameter

In the plot 4.8 it can be observed that the power output exponentially increases with the increase in core diameter of the fiber. Also, the higher the numerical aperture the more is the ability of the fiber to intake concentrated power. Therefore, a fiber with high NA and a reasonable core diameter will be preferred. The optical fiber selected for the STP system is based on the graphical trade-off shown below. All optical fibers listed in the table 4.8 have low OH content and have a transmission range between 300 – 2200 nm. Hence, the FP1000ERT - 0.50 NA, Ø1000 µm Core with Multimode index, Low OH fiber has been selected as it satisfies all the requirements. Even though one of the Thorlabs fibers offers one of the highest core diameters, the former has been preferred due to its smaller bend radius so that it can be stored within a total of 4U Cubesat volume available for the propulsion system.

4.7.1. Mass Estimation and Material

This sub-section will deal with the mass determination of the optical system.

Optical Fiber

The mass of a single optical fiber with diameter 1 mm, NA - 0.5, and 1 m long is 3 grams. This step-index optical fiber (multimode) from ThorLabs has a core made up of pure silica and a hard polymer cladding. The fiber is then sheathed in a Tefzel coating and this material limits the working temperature to a maximum of 150° C (423 K).

Inflatable Parabolic Concentrator Mass

The selected concentrator consists of the following components: reflector surface, torus (support structure) and tripod (support structure). The inflatable concentrator shown in the figure 4.9(a) is

a conceptual design presented in [5] for space-based antenna systems with a diameter of 35 m. As the detailed design of a concentrator is not within the scope of this thesis, the above mentioned inflatable concentrator is taken as reference and the area density of each of the components based on the material (Shape Memory Polymer) has been considered to determine the mass of a scaled down concentrator design. The input parameters taken are listed in the table below.

Component	**Area density** $[Kg/m^2]$
Reflector Surface	0.400
Canopy	0.035
RI Tube + Heater & MLI	1.150
Tripod	1.150

Table 4.9: Area density of Concentrator components [5]

With the given mass density, the mass of the components can be calculated once the area of components is determined. The area of the reflector and the transparent canopy can be mathematically expressed as [60],

$$A_{reflector} = \frac{\pi * \left(\left(\left(\frac{1}{4*f}\right)^2 * d_c^2 + 1\right)^{3/2} - 1\right)}{6 * \left(\frac{1}{4*f}\right)^2} \tag{4.66}$$

The area of the torus and trip are inflatable cylindrical structures and can be calculated using the following equations respectively.

$$A_{torus} = \pi D_{tor} L_{tor} \tag{4.67}$$

$$A_{tripod} = 3\pi D_{tri} L_{tri} \tag{4.68}$$

Here D_{tor} and D_{tri} are the diameters and L_{tor} and L_{tri} is the length of the torus and tripod support structure. The mass of the total system is calculated including the inflation system, miscellaneous, and considering a 20% contingency percentage for the mass of each component. The values have been tabulated in 4.13 and 4.14 for single and bundled optical fiber systems respectively.

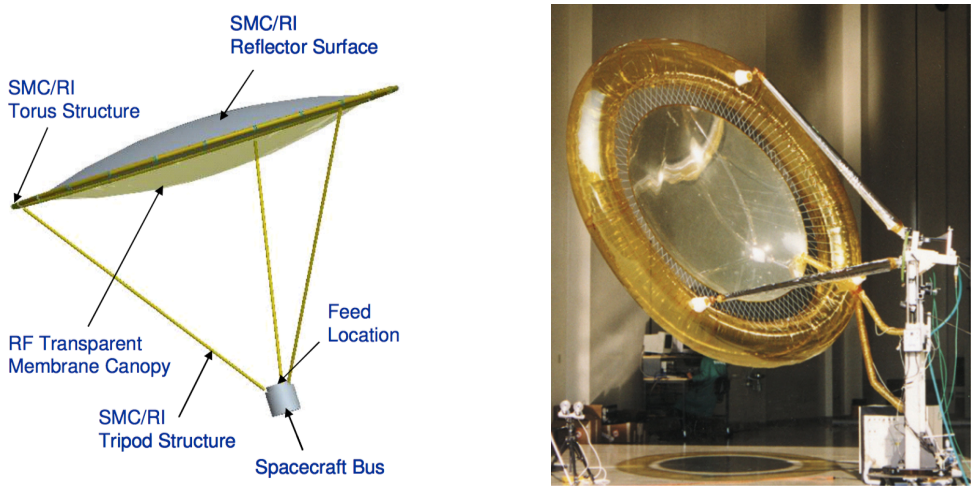

Figure 4.9: Inflatable Concentrator using torus and tripod tube as support structure [5]

4.7.2. Concentrator - Optical Fiber Requirement

Before we proceed with the concentrator selection and system properties, a system requirement for the optical system containing the concentrator and optical fibers is generated. It is solely based on the overall propulsion system requirements defined at the beginning for the LUMIO mission in chapter 2.

In order to define the optical system requirement, the mass and volume available for the subsystem were estimated based on calculations done previously and valid criteria.

Table 4.10: Mass estimation of STP sub-components

Parameters	Value [Kg]	Rationale
Propellant mass at 1000 K	1.848945	Value calculated based on thrust requirement for the mission + 5%. Propulsion 5% on total propellant for calculation uncertainties. The system margin is to compensate for uncertainties and changes in the system design [61].
Thruster mass	0.0054	Molybdenum heat exchanger and insulation mass.
Propellant Tank mass	1.5	Rough calculations
Estimated ADCS mass (micro-resistojet)	0.2114	Assumption,- each 360 g thruster generates 1.5 mN thrust. - Isp - 94.9 s.,ADCS propulsion system requirement for LUMIO : 1. Propellant mass calculated for 72.91 Ns of total impulse is 86.23 g 2. Dry mass from micro-resistojet paper - 310 g (Total system mass (360 g) - propellant mass (50 g) from the literature on micro-resistojet.
Pumps/valves	0.175	MGD1000 ▪ 0-1500 ml/min free flow ▪ Max pressure of 7000 mbar ▪ Voltage range of 5-24V ▪ Size: 55 x 35 x 35 mm ▪ Weight 75g ▪ Sample price: $338-$368 each
20 % Margin	1.064	ESA Standard value - for subsystem Margin for complete new developments [61]
Total mass	4.804745	-
Total Available mass	5.32	Each Cubesat Unit - 1.33 Kg [4U]
Remaining mass	0.5152	Available mass for the concentrator - optical fibers

Table 4.11: Optical system requirements

ID	Name	Requirement	Rationale
Conc-OF-STP-001	Mass	The concentrator - OF system mass shall be below 0.50 Kg	The entire system must fit within 4U (In terms of Cubesat units). This requirement has been generated based on LUMIO propulsion system mass and volume budget. 4U corresponds to 1.33 Kg per unit and total of 5.32 Kg. Deducting the core thruster mass, propellant mass, propellant tank mass, ADCS propulsion system mass and 10% margin to determine the concentrator mass
Conc-OF-STP-002	Packaging Volume	The concentrator - OF system volume shall be below 1000 cm3	Approximated value based on thruster volume and propellant tank (unknown volume - valves, pumps, manifold)
Conc-OF-STP-003	Power	The concentrator - OF system shall be able to provide an output of at least 55 W	With this power, the cavity wall can reach upto 1100 K as stored energy (no propellant flow), Power 10% on nominal power. - ESA Standard

4.7.3. Bundled and Single Optical Fibers

There are two possible arrangements that can be considered for the optical system of an STP consisting of a concentrator and optical fibers: a system with single optical fibers and system with bundled optical fibers. The study and selection of these two arrangements completely depend on the system requirements table 4.11 generated for the optical system and the best fit out of the two will then be picked to proceed with for further analysis.

Single Optical Fibers

A system with single optical fibers means that each optical fiber will be coupled to one concentrator each and the performance of each concentrator-fiber system will be evaluated based on its physical properties and dimensions. Based on the linear increment of parameters such as mass and power output for such a system, the overall system performance is estimated for increasing number of optical fibers. Some of the general input parameters used for both systems have been tabulated below.

Fiber efficiency	Mass of single fiber	Diameter	Numerical Aperture	Fiber Length
0.90	0.003 [Kg]	1 [mm]	0.50	1 [m]

Table 4.12: Optical fiber specificatios

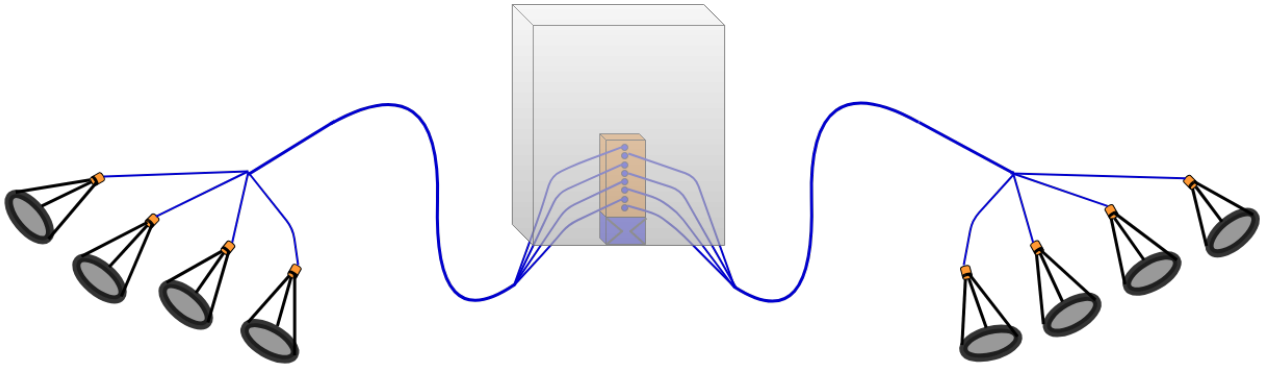

Figure 4.10: Possible configuration of single optical fiber system

Table 4.13: Characterization of single fiber optical system

Number of Optical fibers	Concentrator	Optical fiber			Total Mass [Kg]
	Mass system [Kg]	Mass [Kg]	Expected Power Input [W]	Expected Power Output [W]	
1	0.0245	0.003	7.6731	6.90579	0.0139
2	0.049	0.006	15.3462	13.81158	0.0278
3	0.0735	0.009	23.0193	20.71737	0.0417
4	0.098	0.012	30.6924	27.62316	0.0556
5	0.1225	0.015	38.3655	34.52895	0.0695
6	0.147	0.018	46.0386	41.43474	0.0834
7	0.1715	0.021	53.7117	48.34053	0.0973
8	0.196	0.024	61.3848	55.24632	0.1112
9	0.2205	0.027	69.0579	62.15211	0.1251
10	0.245	0.03	76.731	69.0579	0.139
11	0.2695	0.033	84.4041	75.96369	0.1529
12	0.294	0.036	92.0772	82.86948	0.1668

Bundled Optical Fibers

Bundle packaging fraction is one of the essential parameters that need to be calculated in order to estimate the power loss in transmission. The packaging factor can be defined as the fraction of the cross-sectional area of N single fibers to the total cross-sectional area of the bundle geometry.

$$BPF = N \times \frac{A_{of}}{A_{bundle}} \tag{4.69}$$

Where N is the no.of optical fibers, A_{of} is the cross-sectional area of a single optical fiber and A_{bundle} is the cross-sectional area of the bundle using bundle diameter which has been estimated in the previous table.

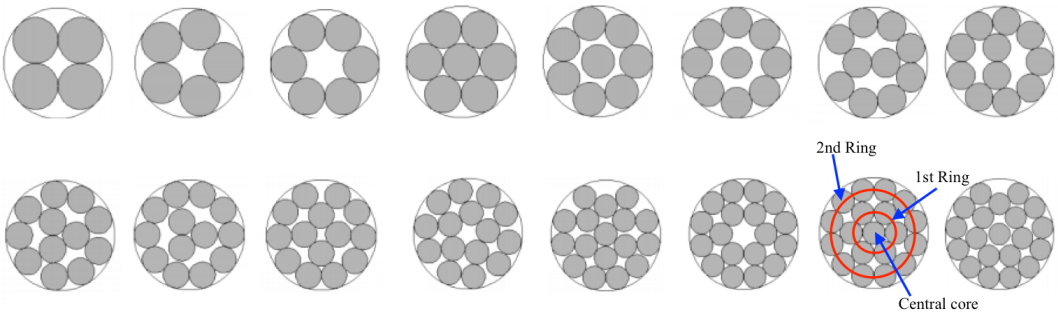

Figure 4.11: Bundled optical fibers with packaging structure

The diameter for bundled fibers can be calculated with the equation where m is the number of rings and d is the diameter of a single optical fiber:

$$D = (2 * m + 1) * d \tag{4.70}$$

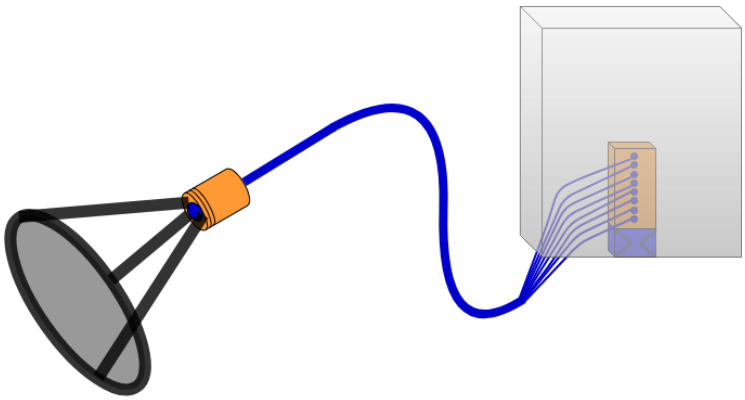

Figure 4.12: A possible configuration of bundled optical fiber system

In the above, the bundled fibers are coupled to one concentrator and thus the concentrator diameter varies with respect to the number of optical fibers. The input power for each optical fiber for the bundled system is the same as ”expected power input” in table 4.13.

Table 4.14: Characterization of bundled fibers optical system

Number of Optical fibers	**Optical fiber**						**Concentrator**		**Total Mass [Kg]**
	Mass [Kg]	Bundle Dia [mm]	Total Bundle Area [mm^2]	BPF	Ideal Power Output [W]	Expected Power Output [W]	Conc. Diam [m]	Mass system [Kg]	
1	0.003	1	0.7854	1.0000	6.9058	6.9058	0.099	0.0245	0.0139
2	0.006	2	3.1416	0.5000	27.6234	13.8117	0.198	0.049	0.0278

Table 4.14: Characterization of bundled fibers optical system

Number of Optical fibers	Optical fiber						Concentrator		Total Mass [Kg]
3	0.009	2.154	3.6440	0.6466	32.0412	20.7176	0.213	0.0735	0.0417
4	0.012	2.414	4.5768	0.6864	40.2431	27.6234	0.239	0.098	0.0556
5	0.015	2.701	5.7298	0.6854	50.3809	34.5292	0.267	0.1225	0.0695
6	0.018	3	7.0686	0.6667	62.1526	41.4351	0.297	0.147	0.0834
7	0.021	3	7.0686	0.7778	62.1526	48.3409	0.297	0.1715	0.0973
8	0.024	3.304	8.5737	0.7328	75.3871	55.2468	0.327	0.196	0.1112
9	0.027	3.613	10.2524	0.6895	90.1473	62.1526	0.358	0.2205	0.1251
10	0.030	3.813	11.4189	0.6878	100.4038	69.0584	0.377	0.245	0.139
11	0.033	3.923	12.0872	0.7148	106.2804	75.9642	0.388	0.2695	0.1529
12	0.036	4.029	12.7492	0.7392	112.1015	82.8702	0.399	0.294	0.1668

From the above tables, the mass of the two optical systems can be compared graphically as shown below in figure 4.13. The mass of the optical system with singles increases linearly with each added fiber whereas, the optical system with bundled fibers is slightly heavier and varies more or less linearly as well. The mass of the coupling interface, structure mass to support the fiber at the focal point of the concentrator and receiver junction is not considered and is assumed to weigh the same for both cases.

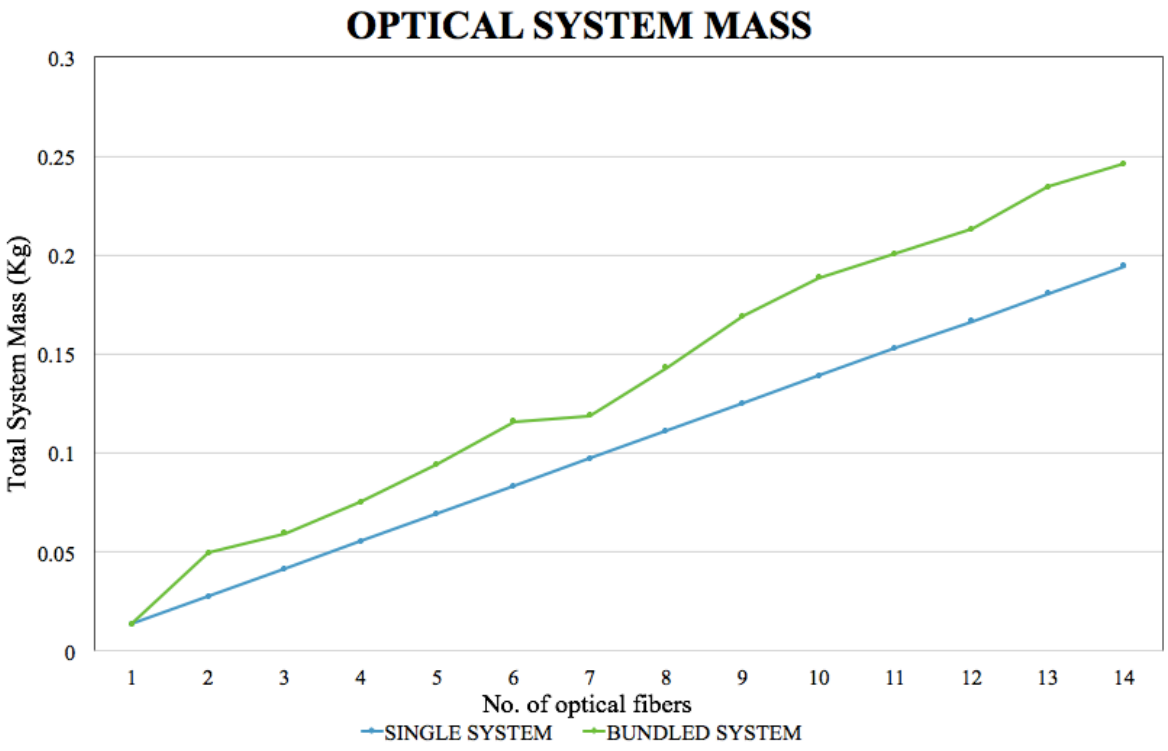

Figure 4.13: Optical system mass for single and bundled fiber system

A trade-off has been done to compare the performance and system properties of single fiber system and fiber bundle system as shown in figure 4.14 just aiming at fulfilling the power requirement for the lunar mission considered for this thesis. Remaining values presented in the tables 4.13 and 4.14 characterize optical systems for other missions demanding different power output. The criteria selected for this trade-off are mass of the system and power output which are quantitatively compared, and complexity of the deployment system and complexity of the inflation system are qualitatively stated. Since both the systems meet the system requirements of the optical system, the goal of this trade-off is to see which one is better with respect to each other. In the case of the power criterion, both systems are capable of transferring almost the same amount of power. As gathered from the above calculations and table, the total mass of the bundle system is 1.3 times heavier than the single fiber system. Naturally, having multiple single fiber-concentrator systems will add to the deployment and inflation system compared to one large concentrator-bundled fiber system. Therefore, to reduce the complexity of the optical system and also because the bundled optical system has more advantages over the single fiber optical system, the bundled optical system has been selected.

For 8 Fib.	Total System Mass [Kg]	Power [W]	Deployment system [Complexity]	Inflation system [Complexity]
Singles	0.1112	55.246	Multiple deploy system will lead to complex setting	Every concentrator will have its own inflation system and hence complex integration
Bundle	0.143 (1.28597 times heavier than singles)	55.247	Single deployement mechanism	Single system and hence less complicated interface

	Within requirement but slighty better
	Within requirement

Figure 4.14: Trade-off matrix for optical system concept

4.8. Initial Design

The initial dimensioning of the heat exchanger and optical system can now be concluded in this section. The fixed dimensions at this stage are only the cavity height at 5 mm (considered from literature in section 3.3.2), channel length at 3.287 cm that has been computed in chapter 3, section 4.3.4 and equilateral corrugated triangles. The nozzle convergent angle and the divergent angle is set to 15 degrees and 20.42 degrees respectively as discussed in section 4.6. The optical fiber selected for the STP system is FT200EMT from ThorLabs with a core diameter of 1 mm and NA of 0.5. In section 4.7.3, the selection of an optical system was achieved and thus, this thesis will proceed with a bundle of 8 optical fibers and a single concentrator system that transmits a total power of 55.246 W. The channel dimensions, nozzle height, and no.of channels are difficult to determine without the thermal analysis. Thus, it must be noted that chapter 4 and chapter 5 iterate parallelly.

The figure 4.15 illustrates the initial design render. The remaining unknown dimensions of the intial design are presented at the end of chapter 5.

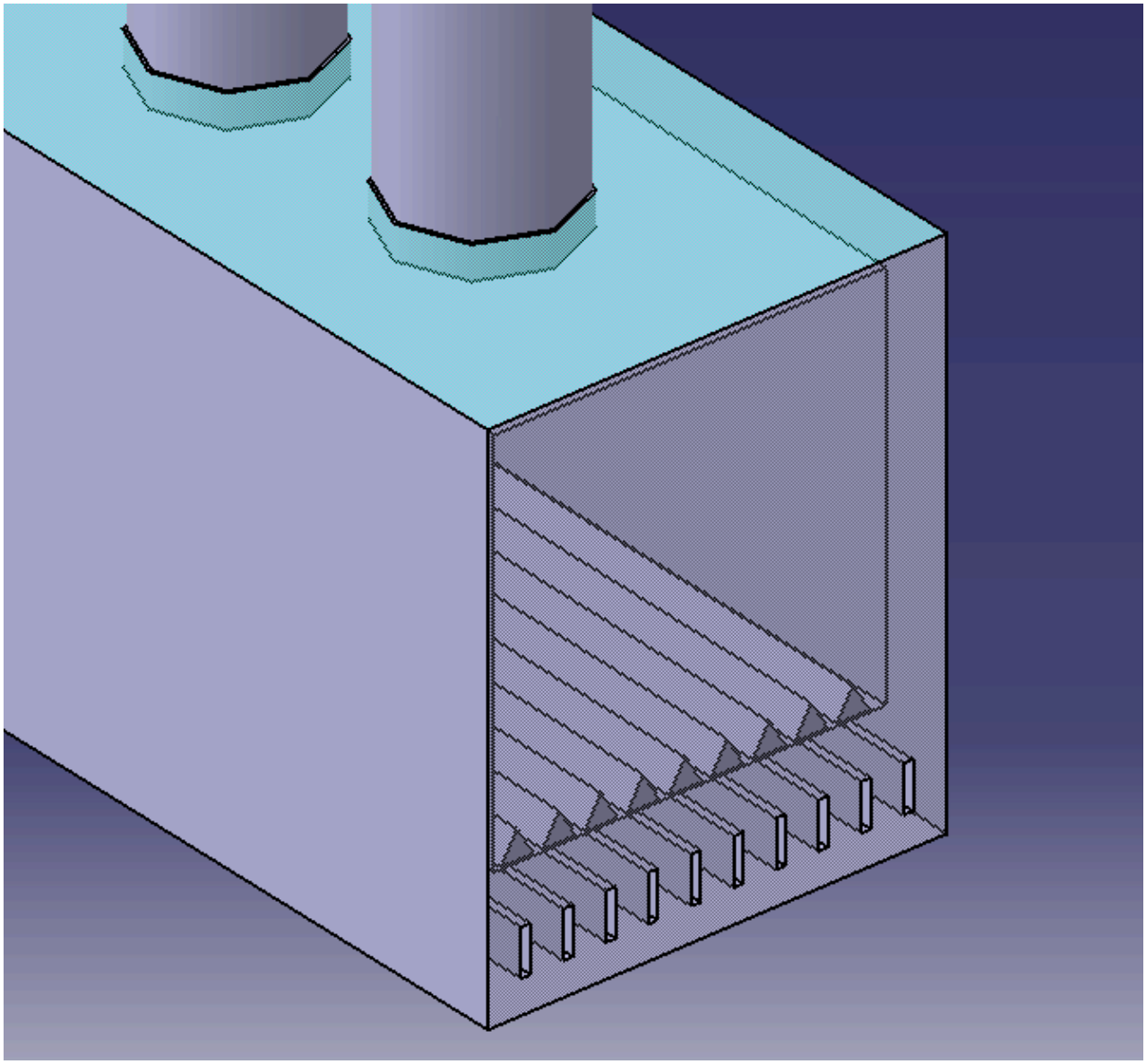

Figure 4.15: Baseline design

5

Thermal Modelling

This chapter will define and formulate the analytical heat transfer model of the heat exchanger and optical system for the preliminary design process. This model has been incorporated for a detailed calculation of the temperatures of the optical fibers, receiver cavity wall and subsequently the channel wall and flow temperatures. Consequently, this model is used for parametric studies that benefit in trade-off analyses due to its low computational time. Different aspect ratios and the channel length of the micro-channels are studied using this tool and it helps to finalize the heat-exchanger dimensions which satisfies the design requirements. This mathematical model in Matlab will be validated using a finite element analysis software, Comsol, in chapter 6.

In order to obtain the final temperature of the heat exchanger walls, the heat loss from the heat exchanger will be computed. This model depends on the power output from the optical fibers and that is determined using equations combined in section 4.4 and 4.7. The energy and transmission model of the optical system is decoupled from the thermal model of the heat exchanger and the output of the former is given as an input for the latter model. The structure of the thermal model is depicted in the figure 5.1 which shows the algorithm flow from the input values to the calculated parameters to the final output.

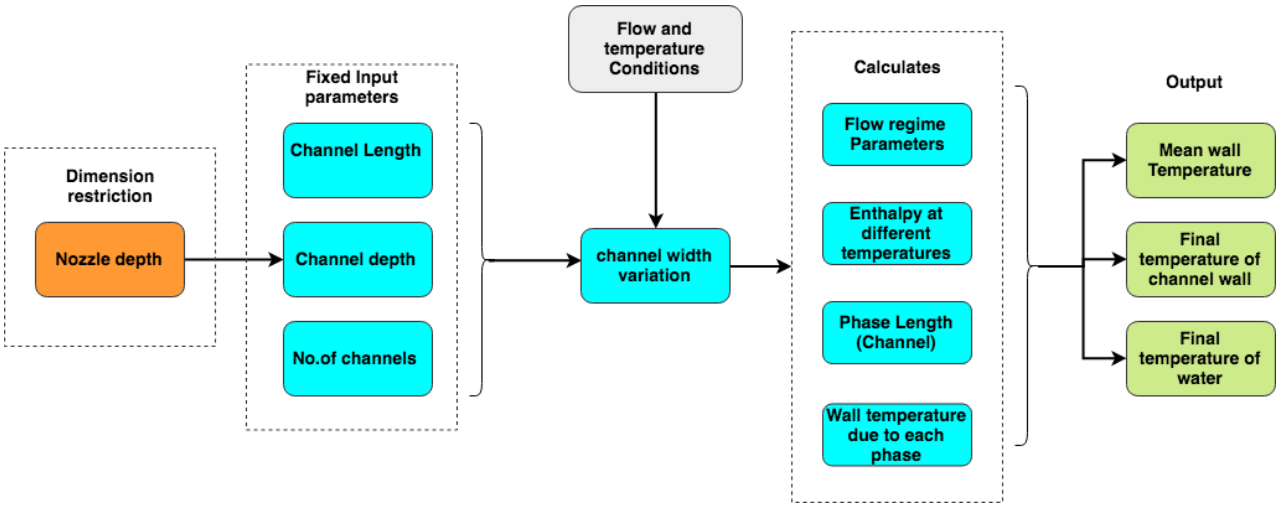

Figure 5.1: Structure of the thermal model for flow and channel wall temperature

The model initially assumes the outer wall and insulating surface temperature for the case I (without insulation) and case II (with insulation) respectively to estimate the inner cavity temperature in an iterative process. Section 5.1 briefly describes the geometrical model of the heat exchanger and optical fibers integrated with the cavity. Section 5.2 then deals with the thermal heat loss model and the equations involved for two cases, namely, with insulation and without insulation. Section 5.3 describes the thermal model of the optical fiber and the total power transmitted through these fibers. Section 5.5 attends to the flow regime within the micro-channels based on the equations described in chapter 4, section 4.3.1 and results in the final temperature of the flow and channel wall at the end of the channel length. A time-dependent thermal model has been incorporated such that the time taken to heat up the walls and subsequently the time taken to cool down can be studied.

5.1. Geometrical Mathematical Model

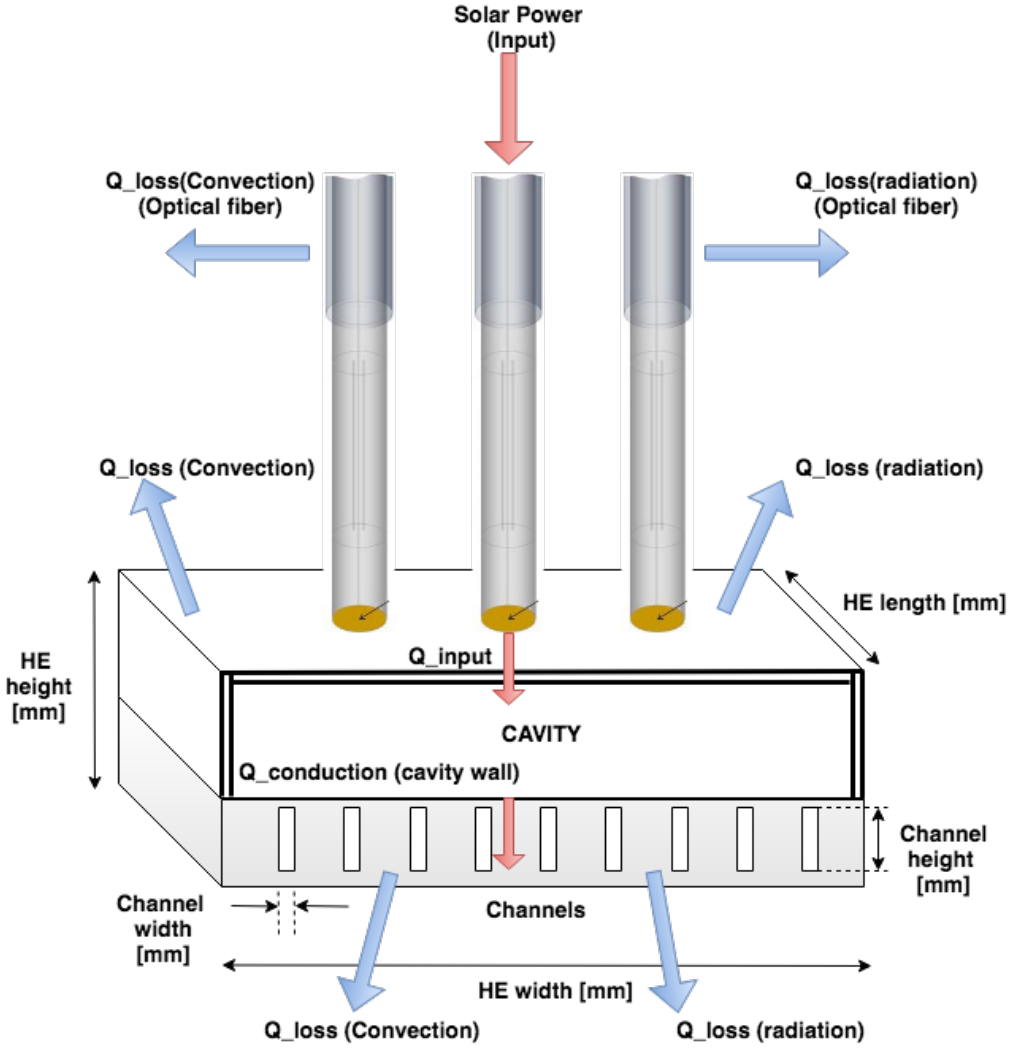

Figure 5.2: Thermal power flow through the Heat Exchanger and Receiver Cavity system without insulation

Before proceeding with defining the mathematical model of the thruster, the geometrical and optical parameters of the initial design will be described. The geometry of the baseline design of the heat exchanger has been described in chapter 4 and can also be seen in the figure 5.2.

5.2. Heat Loss Model

The heat loss model will be computed based on the heat loss taking place from the system outer surface to the surroundings. As heat loss to the surroundings can be more or less prevented by adding insulation, it is mandatory to estimate the heat loss through the insulation as well. Therefore, in this section, a heat loss model will be used to predict the temperature of the system based on input parameters with and without insulation. The required input parameters are geometric dimensions, the mass flow rate of the propellant, solar radiation input, and initial temperature. The generic heat equation for a system can be stated as,

$$Q_{Input} = Q_{Loss} + Q_{Stored} \tag{5.1}$$

Here Q_{Input} is the total thermal power received by the system, Q_{Loss} is the total heat loss of the system and Q_{Stored} is the stored power that heats up the system. Since the heat exchanger and receiver cavity is an enclosed system, the heat loss is will take place from the outer surface only as shown in the schematic diagram shown below 5.3.

The above equation can be elaborated as,

$$Q_{Input} = Q_{radiation} + Q_{convection} + Q_{conduction} + Q_{Stored} \tag{5.2}$$

The thermal power entering the cavity is via optical fibers and have been modelled separately.

5.2.1. Input Thermal Power

The input power to the receiver is the amount of power transmitted by the optical fibers at its output tip. It can be expressed with the following equation using the relation 5.30

$$Q_{input} = \alpha_{cav} Q_{Fiber\ out} \tag{5.3}$$

Where α_{cav} is the absorption coefficient of the cavity material.

The modes of heat transfer depend on the geometry and dimensions of the system and the corresponding correlations for radiation, convection and conduction vary even with the slightest change in dimensions. Thus, the following heat loss equations are split into two cases: without insulation and with insulation. These cases are further discussed in the imminent sections.

5.2.2. Case I: Without Insulation

This case defines a heat exchanger model without any insulation. Therefore, the heat loss via convection (in presence of atmosphere) and radiation is computed from the outer wall of the heat exchanger to the surrounding atmosphere.

Radiation

Any heated surface radiates out energy to its surroundings and this can be defined as a function of the surface emissivity, view factor, surface area and the fourth power temperature difference between the surface and surrounding. In case of a heated heat exchanger, the surroundings can be assumed to be at room temperature.

$$Q_{radiation} = \epsilon \sigma A F_{12} (T^4_{outer\ wall} - T^4_{room\ temp}) \tag{5.4}$$

Here F is the geometric view factor. In general, the view factor F_{12} between two black surfaces A_1 and A_2, can be defined as the fraction of radiation emitted by surface A_1 that arrives at surface A_2. In this case, the view factor between the outer wall of the heat exchanger and the exterior ambient surrounding will be 1.

Convection

The thermal power lost is also due to free convection from the surface of the heat exchanger to its surroundings. The following equation can be used to determine the power lost via free convection:

$$Q_{convection} = h_c A(T_{outer\ wall} - T_{room\ temp}) = \frac{Nuk}{L} A(T_{outer\ wall} - T_{room\ temp}) \tag{5.5}$$

where Nu is the Nusselt number, k is the thermal conductivity of the surrounding medium and h_c is the convective heat transfer co-efficient. In general, the Nusselt number and area of a cuboid can be calculated using the following relations:

$$Nu = \bar{h}\frac{D}{k} \tag{5.6}$$

$$A_s = 2D^2\left(1 + \frac{2L}{D}\right) \tag{5.7}$$

Here D is the length of the shorter side and L is the length of the longer side of the cuboid.

Since the heat exchanger is a cuboid, the Nusselt number can be determined based on the long horizontal non-circular cylinders model as described in [62]. As the convective heat transfer co-efficient is unknown, the Nusselt number can be estimated using the following correlations:

$$Nu^T = G\bar{C}_l Ra^{1/4} \tag{5.8}$$

$$Nu_l = \frac{C2}{log\left(1 + \frac{C2}{Nu^T}\right)} \tag{5.9}$$

$$Nu_t = \bar{C}_t Ra^{1/3} \tag{5.10}$$

$$Nu = [(Nu_l)^m + (Nu_t)^m]^{1/m} \tag{5.11}$$

Ra is the Rayleigh number in equation 5.8. In the case of free convection, the Rayleigh number gives a proper indication of the flow regime of the boundary layer at the surface i.e whether it is turbulent or laminar. In the current thermal model of the heat exchanger, the surface is considered to be in contact with air. Therefore, the properties of air at the surface temperature of the outer wall are considered.

$$Ra = \frac{g\beta\Delta T D^3}{\nu\alpha} \tag{5.12}$$

Since the heat exchanger both with and without insulation remains a cuboid, the above correlations are applicable for both cases. For the case I, this model is valid for cuboids that have an aspect ratio (L/D) larger than 4 with D being the length of the shorter side of the cuboid.

Conduction

An important step before calculating the heat loss by radiation and natural convection from the outer surface of the system, with and without insulation, is defining the conduction model. As seen in the above equations, the heat loss depends on the temperature of the outer surface of the heat exchanger and that depends on the heat conducted through the inner wall of the cavity to the outer wall. Hence, the conducted power through the system can be calculated using the following equation,

$$Q_{conduction} = \frac{k\ A}{L}\Delta T \tag{5.13}$$

Since the heat exchanger can be considered to be rectangular cuboid, in order to calculate the heat conducted from the inner cavity wall to the outer surface, the conduction shape factor needs to be calculated first as it is not one of the conventional enclosed geometries. The conduction shape factor is characterized as a geometry dependent quantity and is related to the power as:

$$Q_{conduction} = S^*_{\sqrt{A_i}} k(T_{inner\ wall} - T_{outer\ wall}) \tag{5.14}$$

Most papers in the literature describe the conduction shape factor for spherical and cylindrical cavities enclosed within same geometries, and the models are restricted to uniform gaping between the geometries. However, the paper [63] describes analytical models to calculate the conduction shape factor for a variety of geometry combinations, including a cuboid in a cubical enclosure, which is needed for the purpose of the presented design in this thesis. A cross-sectional cut view of the cavity generic dimensions can be seen below for better understanding.

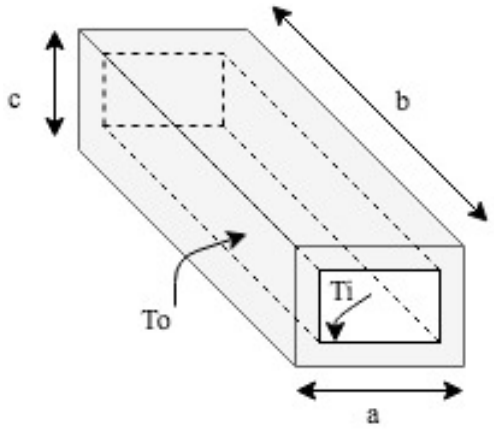

Figure 5.3: Schematic diagram of enclosed cavity and outer geometry with effective gap (thickness) for conduction

The conduction shape factor (CSF) can be calculated using two methods, namely, integral method and two-rule method. The difference between the two is the complexity of the inner body geometry and easy estimation of the effective gap spacing, which is defined as the thickness between enclosures. The former method is used in cases of uniform gaping especially in concentric spheres where the effective gap is determined using area integration of spherical coordinates. For cases involving the complex formulation of area integration due to multiple faces, the latter method is used. This method, as the name suggests, involves two steps. The first being calculation of the net volume of the enclosure and the next being the area of the inner geometry.

Using the two-rule method, CSF can be mathematically expressed as [63]

$$S^*_{\sqrt{A_i}} = \frac{\sqrt{A_i}}{\delta_e} + S^*_{\infty} \tag{5.15}$$

$$S^*_{\sqrt{A_i}} = \frac{2\sqrt{\pi}}{\left[1 + 6\pi\left(\frac{V^{1/3}}{\sqrt{A_i}}\right)^3\right]^{1/3} - 1} + S^*_{\infty} \tag{5.16}$$

Here $S^*_{\sqrt{A_i}}$ is the conduction shape factor taking the characteristic length as the square root of the surface area of the inner body, S^*_{∞} is the shape factor for full-space limit and has been calculated

using Yovanovich and Culham's model to have a value of 3.469. The selection of the characteristic length has been proposed to be the square root of surface area for non-circular channels by several researchers as a scale for problems dealing with convection and conduction. The method presented in the paper has been validated with numerical simulations.

Therefore, the inner wall temperature can be obtained with the equation below:

$$Q_{conduction} = Q_{convection} + Q_{radiation} \tag{5.17}$$

$$T_i = \left(\frac{1}{S^*_{\sqrt{A_i}} k}\right)\left(\epsilon\sigma A(T_o^4 - T_r^4) + A\frac{(Nuk_{air})}{D}(T_o - T_r)\right) + T_o \tag{5.18}$$

Here T_o is the outer wall temperature of the cavity without insulation, T_i is the inner wall temperature of the cavity, T_r is the room or ambient temperature, L is the length of the heat exchanger, and k_{mo} is the thermal conductivity of the heat exchanger material.

5.2.3. Case II: With Insulation

In this case, the heat exchanger model is defined with insulation around it. Therefore, the heat loss via convection (in presence of atmosphere) and radiation is computed from the outer wall of the insulation to the surrounding atmosphere. Apart from a change in the area of the outer surface which is in direct contact with the surrounding and material emissivity, the heat loss via radiative heat transfer relation remains unchanged. Certainly, a system with insulation is required and integrated to prevent any damage the hot heat exchanger can cause to the surrounding sub-systems and electronics components.

Conduction

When insulation is added to the system, the final temperature attained at the outer surface of insulation differs from the without insulation case due to the thermal conductivity and area of the insulating layer. The heat transfer via conduction for a layered system can be determined by calculating the effective conductivity through the wall of the heat exchanger to the insulation as:

$$\frac{L}{K_{eff}A_{HE}} = \left[\frac{1}{k_{mo} * S^*_{\sqrt{A_i}}} + \frac{1}{k_{ins} * S^*_{\sqrt{A_o}}}\right] \tag{5.19}$$

$$Q_{cond} = \frac{K_{eff}A_{HE}}{L}(T_{ins} - T_{room}) \tag{5.20}$$

k_{ins} is the thermal conductivity of the insulating material, $S^*_{\sqrt{A_o}}$ is the conduction shape factor taking the characteristic length as the square root of surface area of the outer body (heat exchanger) and T_{ins} is the temperature of the outer surface of the insulation. The equation 5.20 can then be substituted into equation 5.18 to calculate the inner wall temperature of the cavity.

Convection

In case of added insulation, the system no longer has L»D as an insulation thickness of 1.2 cm is taken on either side. The Nusselt number can be then determined based on the short square cylinder - face up model as described in [62].

$$Nu^T = G\bar{C}_l Ra^{1/4} \tag{5.21}$$

$$Nu_l = [(N_{cond})^n + (Nu^T)^n]^{1/n} \tag{5.22}$$

$$Nu_t = \bar{C}_t Ra^{1/3} \tag{5.23}$$

$$Nu = [(Nu_l)^m + (Nu_t)^m]^{1/m} \tag{5.24}$$

This model is valid for cuboids that have an aspect ratio (L/D) smaller than 4. The table below 5.1 shows the coefficients for the cases both with and without insulation models.

Table 5.1: Convection Coefficient values for short and long non-circular cylinders

Model	L/D	Nu_cond	G	C_t Pr- 0.71 (air)	n	m	C_2
Short non-circular cylinder	0.625	1.63	0.828	0.094	1.07	10	-
Long non-circular cylinder	-	-	0.735	0.087	-	4.5	1/3

5.2.4. Power Lost to Propellant Flow

The power transmitted to the propellant adds to the total heat lost and when the water is released into the heat exchanger, the power transferred can be determined as follows:

$$Q_{prop} = \dot{m}(h_{final\ temp} - h_{inlet\ temp}) \tag{5.25}$$

As the ultimate aim is to heat up the propellant to 1000 K, the power is required to heat water from 293.15 K to 1000 k at 5 bar. The mass flow rate is determined based on the thrust required. The change in enthalpy is obtained as follows:

$$\Delta H = \Delta H_{293.15K \rightarrow T_{boil_{liq}}} + \Delta H_{T_{boil_{liq}} \rightarrow T_{boil_{gas}}} + \Delta H_{T_{boil_{gas}} \rightarrow 1000K} \tag{5.26}$$

Here $T_{boil_{liq}}$ is the boiling temperature of water at 5 bar, still in liquid state, which is 424.98 K and $T_{boil_{gas}}$ is the boiling temperature of water when the phase changes to a gaseous state. The difference between the enthalpies at these two temperatures gives the heat of vaporization.

Table 5.2: Enthalpy of water at different temperatures at 5 bar

$H_{293\ K}$	$H_{boil_{liq}}$	$H_{boil_{gas}}$	$H_{1000\ K}$	ΔH	$Unit$
105.290	639.54	2560.7	3988.500	3883.210	KJ/ Kg

5.3. Thermal Study of the Optical System

This section will elaborate on the thermal model of the optical fibers. As the rate of heat energy received by the optical fiber is dependent on the concentrator surface and having determined the geometrical parameters of the optical system in chapter 4, the analytical study can be carried out. The rate of heat energy received by the parabolic concentrator can be determined using the following equation[64][65]:

$$Q_{conc\ in} = 2\pi f \rho_{mirror}\, S(sin^2\phi_{rim} - sin^2\phi_{shading}) \tag{5.27}$$

where S is the solar flux, f is the focal length, ρ_{mirror} is the reflectance of the mirror surface, ϕ_{rim} is the rim angle of the parabolic concentrator and $\phi_{shading}$ is the shading angle because of the optical fiber core (tip size). Assuming an ideal concentrator, the efficiency of the parabolic concentrator can be as [66].

$$\eta_{conc} = \frac{(sin^2\phi_{rim} - sin^2\phi_{shading})}{4\ tan^2(\theta_{max}/2)} \rho_{mirror} \tag{5.28}$$

Now, assuming that the optical fiber is placed exactly at the focal point of the parabolic concentrator and lies on the focal plane, the rate of energy at the inlet of the optical fiber can be estimated based on opto-geometrical parameters as presented in [64].

$$Q_{Fiber\ in} = \frac{\pi D_{conc}^2}{16\ tan^2(\theta_{max}/2)} \times \rho_{mirror}\ S\ (sin^2\phi_{rim} - sin^2\phi_{shading}) \tag{5.29}$$

Here, the mirror reflectively (ρ_{mirror}) is assumed to be 0.8 [20] for a parabolic mirror surface.

Here polarized reflection of radiation entering the optical fiber is considered as the light is propagating from the space environment to the core material of the fiber.$Q_{Fiber\ in}$ has been calculated to be 7.6731 W for 1 optical fiber with a core diameter of 1 mm. The power at the output tip of the fiber can be obtained from the relation given below.

$$Q_{Fiber\ out} = \eta_{of} Q_{Fiber\ in} \tag{5.30}$$

5.3.1. Heat Loss in Optical Fiber

Similar to any other body in the atmosphere, the heat loss in optical fibers also takes via convection (in the presence of atmosphere) and radiation. This section delves into the equations used for determined the heat loss taking place in fibers.

Conduction

To determine the heat loss through the optical fibers via convection and radiation to its surrounding atmosphere, a similar method as for the heat loss in the heat exchanger is applied. Hence, first, the conduction through the fiber is computed as this will provide the outer coat temperature.

The effective axial conductivity of the fiber and conducted heat is formulated to be:

$$\frac{L}{K_{eff}A_{fiber}} = \left[\frac{1}{k_{core} * 2 * \pi * R_{core} * L_{of}} + \frac{log(R_{clad}/R_{core})}{k_{clad} * 2 * \pi * L_{of}} + \frac{log(R_{coat}/R_{clad})}{k_{coat} * 2 * \pi * L_{of})}\right] \tag{5.31}$$

$$Q_{cond} = \frac{K_{eff}A_{fiber}}{L}(T_{coat} - T_{room}) \tag{5.32}$$

Convection

Considering the optical fibers as long vertical cylinders, the convection heat transfer from the lateral surface can be calculated using the following relations for a cylinder of length L and the total diameter of the fiber, including cladding and coating, D [62]. The Nusselt number for a vertical cylinder is determined for uniform heat flux and is based on the Nusselt number for a vertical flat plate of height L. It can be written as follows,

$$Nu_l = \frac{\xi}{ln(1+\xi)} Nu_{l,Plate} \tag{5.33}$$

$$\xi = \frac{1.8\ L/D}{Nu_{Plate}^T} \tag{5.34}$$

where, the $Nu_{l,Plate}$ and Nu_{Plate}^T for a vertical plate receiving uniform heat flux and constant ambient temperature can be estimated using the relations 5.35 and 5.36

$$Nu_{l,Plate} = \frac{1}{ln(1 + \frac{1}{Nu^T})} \tag{5.35}$$

$$Nu_{Plate}^{T} = \overline{H}_l \, Ra^{1/5} \qquad \overline{H}_l = \frac{6}{5}\left(\frac{Pr}{4 + 9\sqrt{Pr} + 10Pr}\right)^{1/5} \tag{5.36}$$

$$Nu_t = \frac{(C_t^V)^{3/4} \, Ra^{1/4}}{\left(1 + \left(\frac{C_2 Pr}{Ra}\right)^{0.4}\right)} \qquad C_2 = 7x10^{12} \tag{5.37}$$

$$Nu = (Nu_l^m + Nu_t^m)^{1/m} \qquad m = 6.0 \tag{5.38}$$

The heat loss via convection can subsequently be calculated using equation 5.5.

Radiation

The buffer or jacket of the optical fibers will undoubtedly also radiate heat to the surrounding atmosphere. Similar to the section 5.2.2 the heat lost via radiation can be described. In this case, the surface emissivity of the outer material is 0.3 and the view factor is 1. All the above equations are incorporated into the thermal model and used to calculate the temperature of the system due to the stored energy.

5.3.2. Optical Fiber Power Transmission

As explained in section 4.5, the efficiency is considered to be 90%, therefore, for a power input of 7.6731 W, the power output at the end of a 1 m long optical fiber is 6.9058 W. As the number of optical fibers increases, the total power input for the heat exchanger linearly increases as shown in the plot 5.4 below. The power output in both single and bundled optical fiber systems is the same to the second decimal point as can be seen in tables 4.13 and 4.14, therefore, no additional changes or effect applies to the thermal model of the heat exchanger due to the selected optical system.

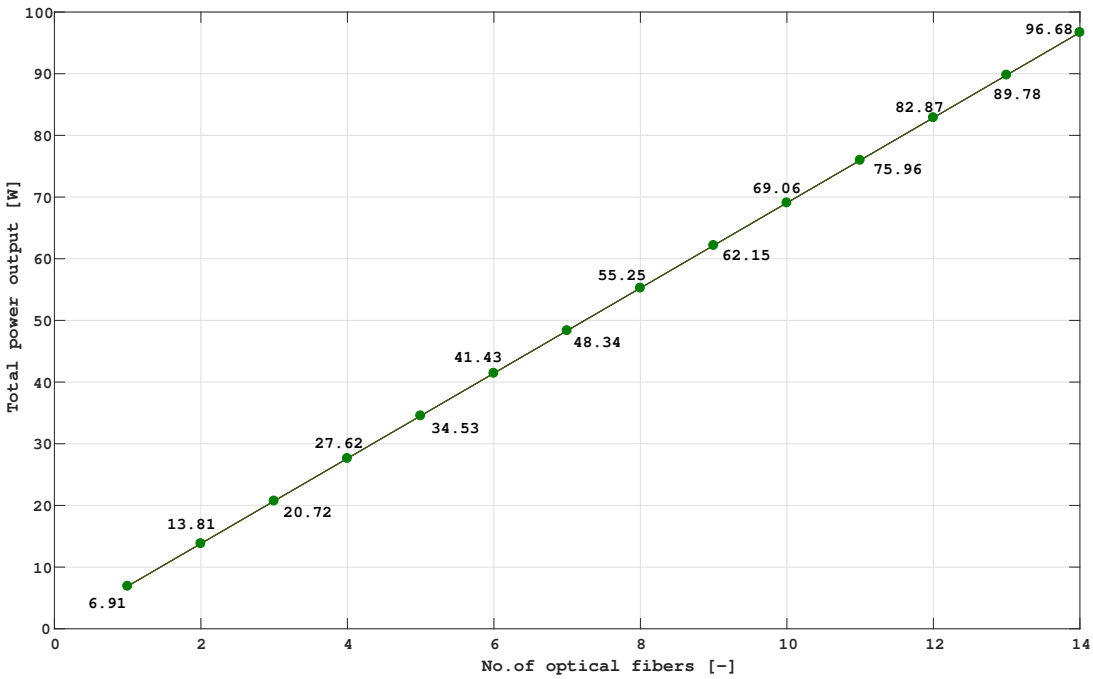

Figure 5.4: Total power output vs. No. of optical fibers plot

5.4. Time Dependent Model

The time-dependent model is introduced to analyze the heat losses to the surroundings and the time taken by the heat exchanger to get heated and to cool down. It is also important to ensure that the propellant is discharged once the heat exchanger cavity reaches an equilibrium to prevent insufficient heating. This section will deal with two cases, namely, dry and wet operation. In the dry operation model, there is no propellant flow through the channels and the loss of heat energy to the propellant flow is neglected whereas, the wet operation model discharges water into the heat exchanger channels once no change in temperature is observed.

(Q_{stored}) is the stored thermal energy that contributes to the heating of the heat exchanger itself.

$$Q_{stored} = Q_{input} - Q_{loss} \tag{5.39}$$

For dry operation the power lost in heating up the propellant, Q_{prop}, becomes zero and for wet operation, Q_{prop} has a finite value. The heat loss due to radiation, convection, and propellant flow is calculated at every time step to determine the rise in the cavity wall temperature. The heat losses are computed radially and not axially. The time-dependent loop can be described as follows

$$Q_{loss,\ i} = Q_{covection,\ i} + Q_{radiation,\ i} + Q_{prop,\ i} \tag{5.40}$$

In the case of wet operation (with propellant), the water enters into the system once the cavity temperature stabilizes. The heat transferred to the propellant is included in the heat lost is because it lowers the final temperature of the cavity wall.

$$Q_{stored,\ i} = Q_{input,\ i} - Q_{loss,\ i} \tag{5.41}$$

$$\Delta T_i = \frac{Q_{stored,\ i}}{Cp_{mo} Mass} \tag{5.42}$$

$$T_{i+1} = T_i + \Delta T_i \tag{5.43}$$

This stored energy increases the temperature of the cavity of the heat exchanger and the increase in cavity temperature with time can be seen in the plot below. The simulation includes a thick insulation of 1.2 cm on either side of the heat exchanger which causes the cavity temperature to reach up to 1200 K using 8 optical fibers. At 800 seconds, when the cavity is observed to attain a constant temperature, loss due to power transferred into heating the water begins. An immediate drop in the cavity wall temperature can be noticed as a result, followed by reaching a constant wall temperature until the power input is cut off from the system.

From the plot 5.5 it can be concluded that the power needed to reach a wall temperature of about 1220 K during dry operation and 1083 K during water flow through the system is 55.25 W and requires 8 optical fibers for the power transmission.

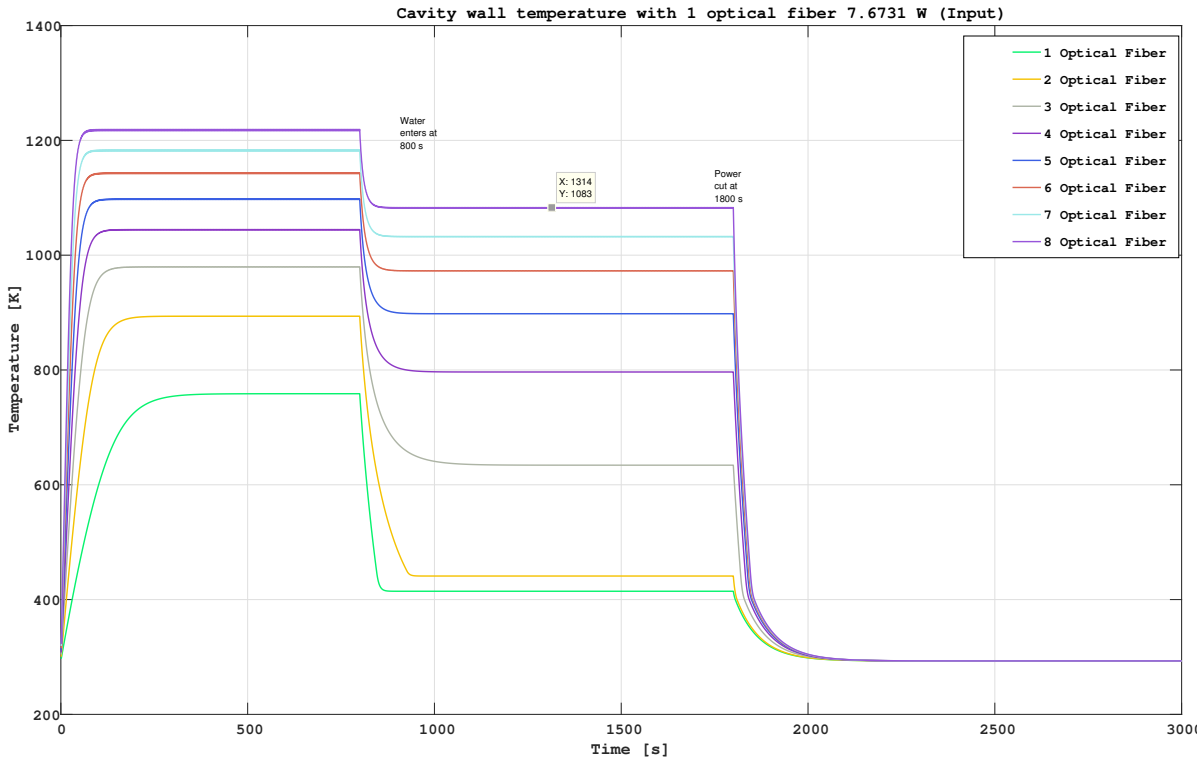

Figure 5.5: Cavity wall temperature with increasing no. of optical fibers

5.5. Flow and Channel Wall Temperature Model

The flow in the micro-channels is modelled based on forced convection with the relations described in section 4.3. Several theoretical models have been developed at the department of space systems engineering that includes two-phase flows and takes into account the change in propellant properties with phase change. One of the models developed in [67] is referred to as the baseline structure to include single phase and two phase flow properties. The aspect ratio in this study is defined as the ratio of the channel height to the channel width ($H_{channel}/W_{channel}$)

In the plot 5.6, for channel heights lower than 0.7098 mm no significant change in temperature is observed for a length of 4.023 cm. If we look at the table 4.1 of nozzle depth and flow regime, it is noted that below the depth of 0.7098, the Knudsen number begins to increase. A higher Knudsen number is attributed to higher losses due to viscous flow. Since a final flow temperature of 1000 K is achieved at 0.7098 mm of channel depth itself, this height will be selected since it's characterized by higher Reynolds numbers, which is slightly better for the purpose of heat transfer efficiency.

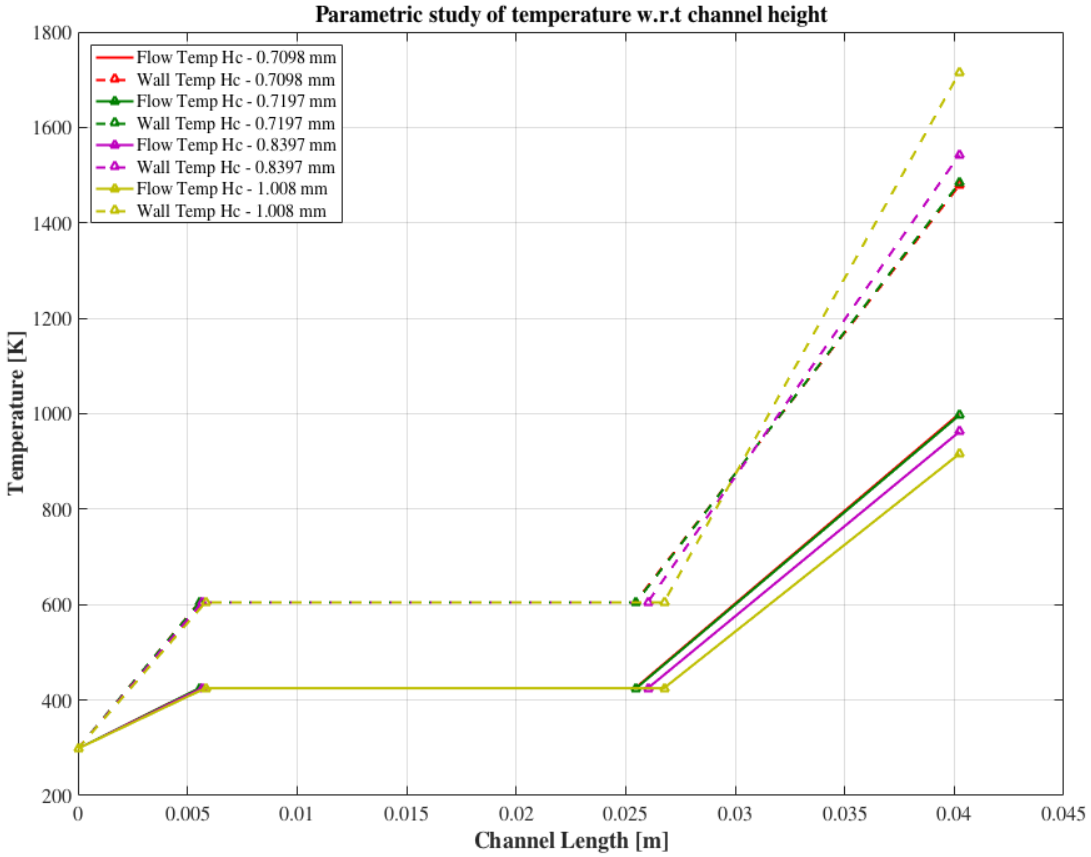

Figure 5.6: Effect of channel height on the final flow temperature

In the plot 5.7, the channel length, number of channels and channel height are kept constant at 4.023 cm, 10 and 0.7098 mm respectively. It can be observed that the flow temperatures do not get heated sufficiently and clearly take longer to reach the gaseous state with the decrease in aspect ratio. The mass flow rate is assumed to be equally distributed in each channel and thus, the mass flow rate in each channel is determined as:

$$\dot{m}_{channel} = \frac{\dot{m}}{N} \tag{5.44}$$

As the number of channels (N) remains constant, the mass flow rate or mass flux through each channel remains constant as well. This drop in the final flow temperature can be accounted due to the insufficient heating or comparatively lower heating of the fluid particles at the top layer, as it may not come into contact with the top heated wall due to wider channels. Also, at lower aspect ratios, the flow becomes laminar and hence, theoretically, it becomes less efficient for the convective heat transfer because the laminar boundary layer growth creates a stagnation zone.

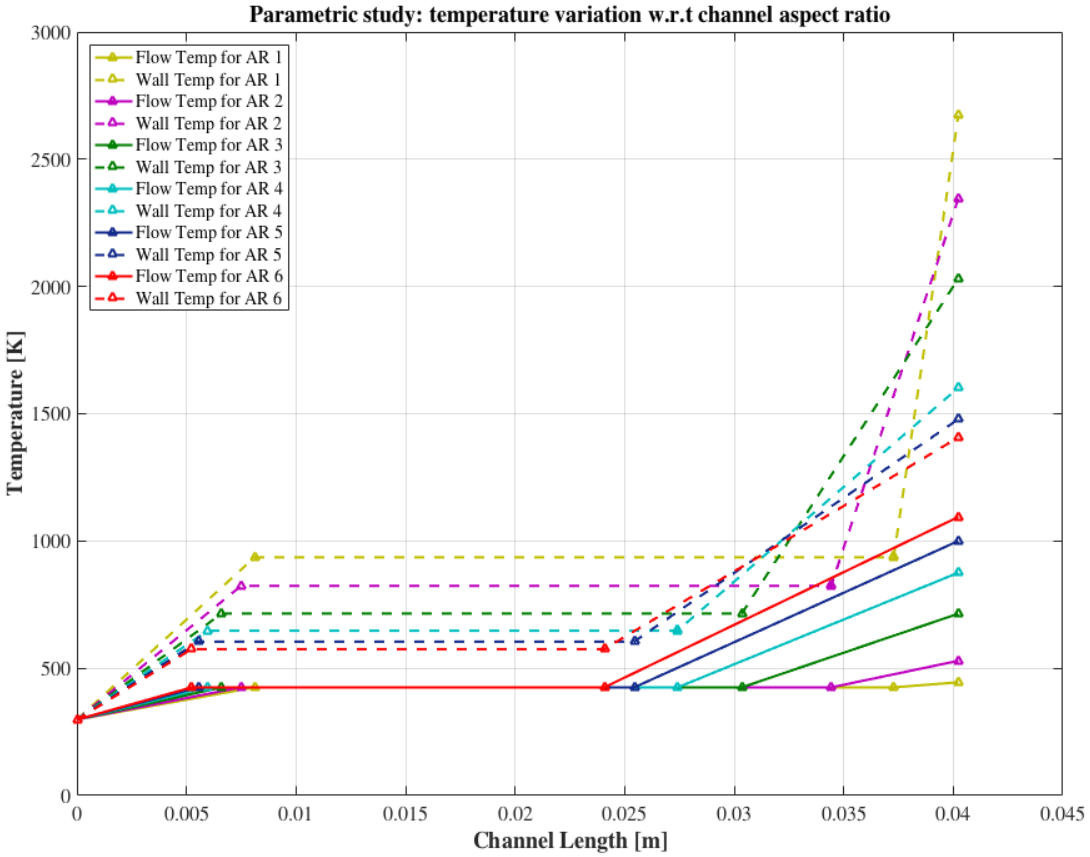

Figure 5.7: Effect of channel aspect ratio on the final flow temperature

The next figure 5.8 depicts the required channel length to ensure heating up of water up to a temperature of 1000 K for a channel height of 0.7098 mm, aspect ratio of 5 and no.of channels equal to 10. For a channel length 4.023 cm, the flow temperature at the end of the channel reaches to 1000 K.

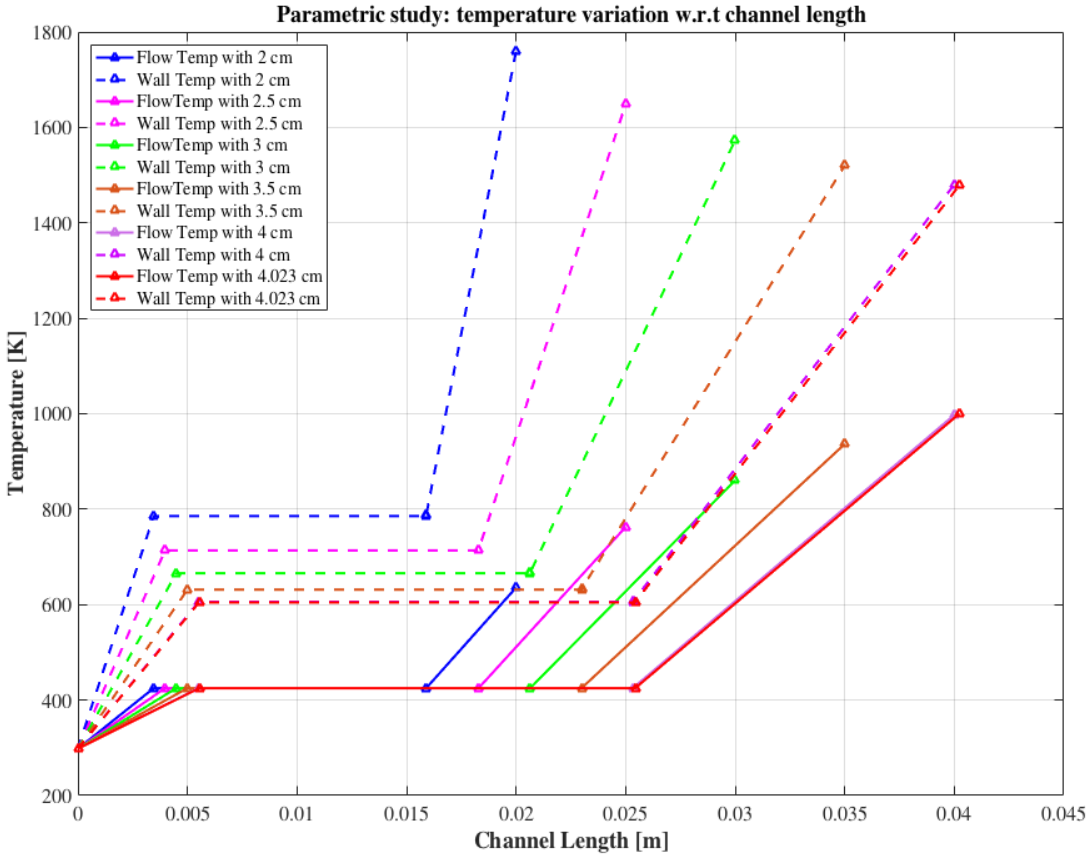

Figure 5.8: Determining the required (minimum) channel length to reach a flow temperature of 1000 K

Following the parametric study of the channel length and aspect ratio for a fixed mass flux through the channels, it can be gathered that a channel height of 0.7098 mm with an aspect ratio of 5 and a length of 4.023 cm is the most eligible design to ensure the heating of the propellant up to 1000 K (**REQ-HE-6**) while staying within the channel length (**REQ-HE-5**) criteria.

Pressure loss in the channel was then studied for the selected channel length based on the equations defined in chapter 4, sub-section 4.3.2. A parametric study is also conducted to observe the change in pressure drop with respect to the aspect ratio of the channels for all channel height cases while keeping the number of channels and channel length constant.

In figure 5.9, it is evident that the lowest value of total pressure drop is for the least aspect ratio for the highest value of channel height (height: 1.008 mm, width: 0.504), keeping mass flow rate through the cross-section constant. The pressure drop is inversely proportional to the hydraulic diameter (D_h) of the channel. Considering the channel dimension that fulfills the temperature requirement, the total pressure drop is observed to be 0.0578 pa. Hence, the pressure at the chamber will drop to 4.9999 bar. Further drop in pressure will be noticed once the pressure drop at inlet manifold is included.

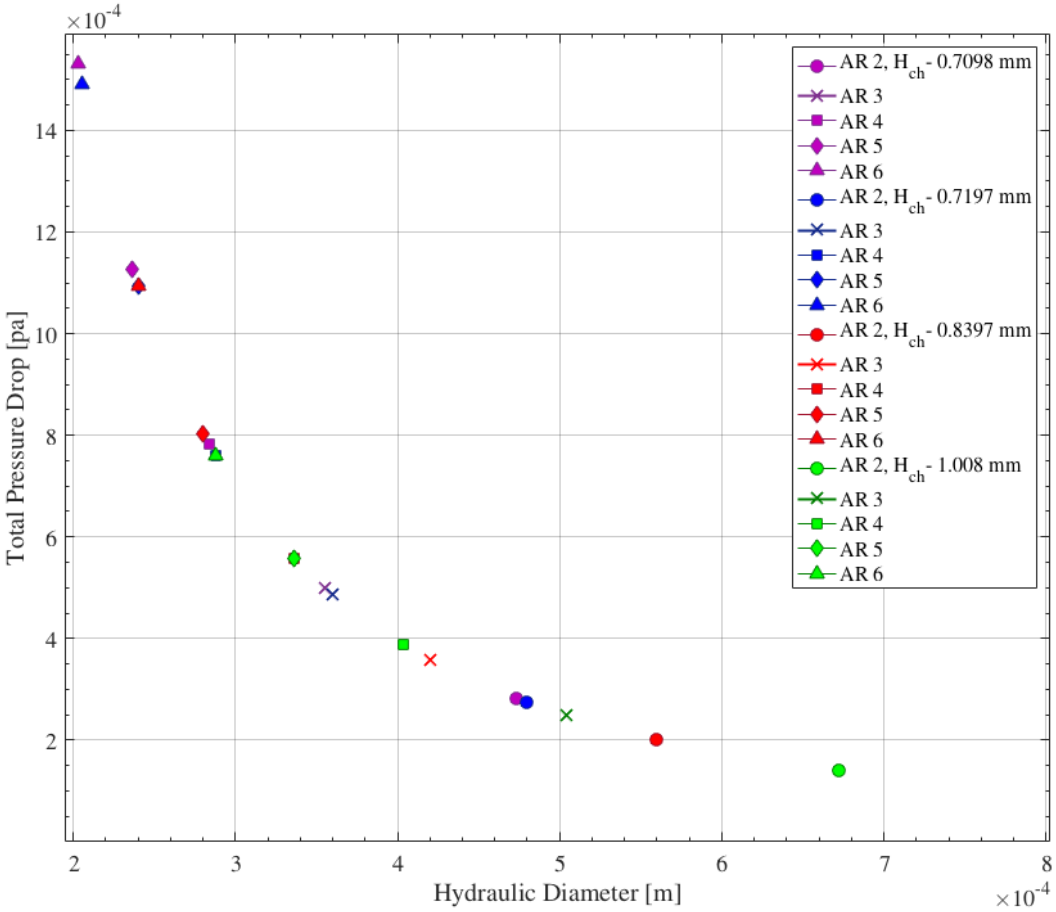

Figure 5.9: Pressure drop in the channels with respect to aspect ratio with constant channel length

Table 5.3: Pressure drop in a channel length of 4.023 cm

	Water Flow [Single phase]	**Boiling [Two phase]**	**Vapor Flow [Single phase]**
Channel Length [m]	0.0055	0.0200	0.0148
Frictional Pressure Drop [pa]	0.0051338	0.049498	0.0020293
Accelerational Pressure Drop [pa]	-	0.0011	-
Total Pressure Drop [pa]	0.0578		

Keeping the initial baseline dimensions from chapter 4, the channel dimensions have been determined in as a result of the thermal analysis done in this chapter. Figure 5.10 shows the baseline

design attained after a parametric study. The channel length has been changed from 3.287 cm to 4.023 cm due to increased length of the two phase flow that has been inferred from the plot explained in the above sections. This design will be imported to the Comsol model of ray heat tracing to investigate the ray power deposited on the surface of the corrugated cavity.

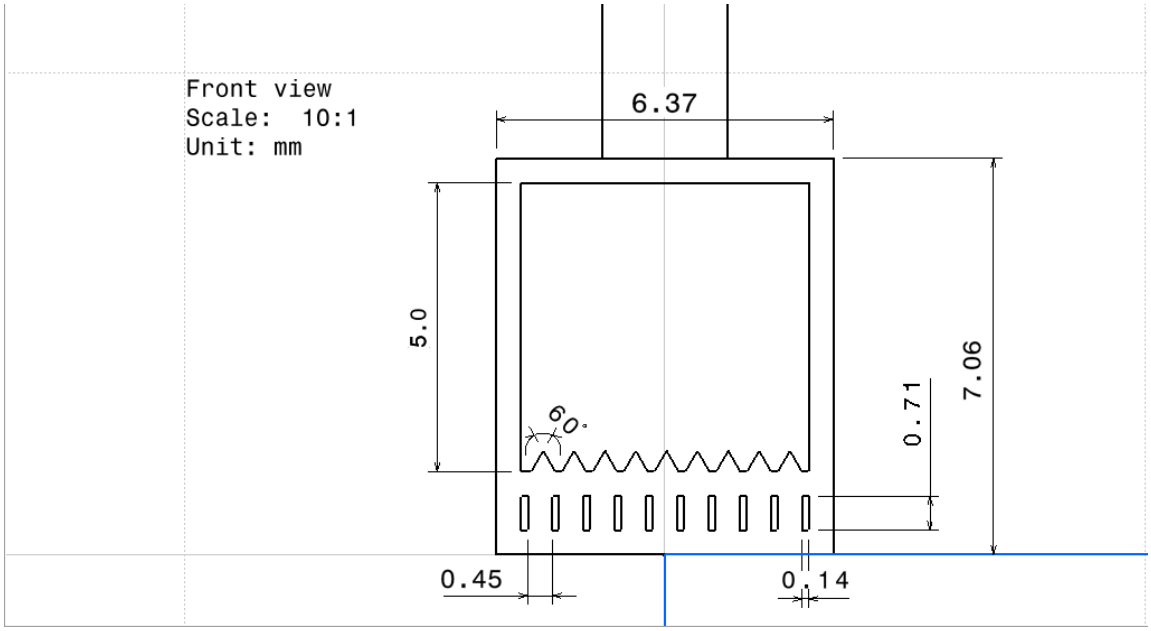

Figure 5.10: Baseline design dimensions: front view

6

Final Design and Results

This chapter attends to the verification of the analytical model with a multiphysics finite element analysis software, Comsol 5.3A, for the final design. The final design attained from the analytical study of the heat exchanger is imported into Comsol. This software offers coupling of the geometrical optical rays and heat transfer in solids as well as conjugate heat transfer. The verification of the final design is split into two FEA models. The first model (section 6.1.2) is based on the ray optics module and the heat transfer module coupled for the heat exchanger with optical fibers integrated into the design. The second model (section 6.1.3) uses the conjugate heat transfer module to investigate the heat transfer between the channel walls and the propellant flow through the channels.

This chapter further focuses on the final design of the thruster and its performance. The final design was achieved following an iterative process between the detailed design and thermal model of the design. The figure 6.1 depicts the process structure incorporated between the Matlab and Comsol model.

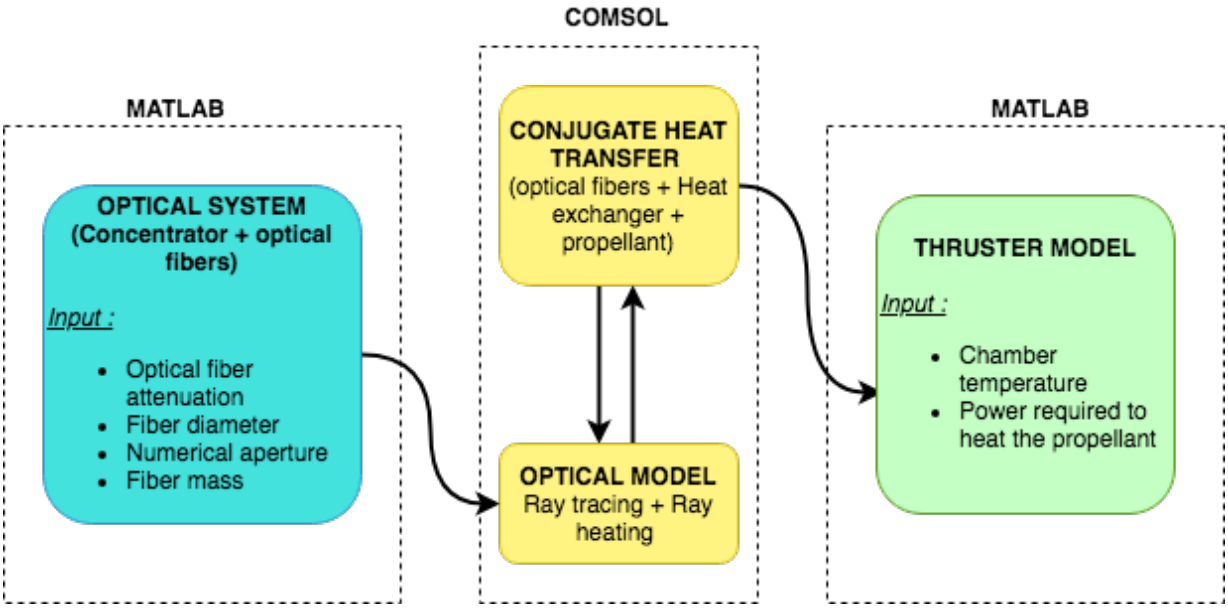

Figure 6.1: Model structure of the iterative process

Due to the lack of computational power to run heavy Comsol 5.3A files, the simulation was split

into two models. The final temperature of the cavity walls attained from the ray heating model was given as input in the conjugate heat transfer model which includes propellant flow through the channels. The chapter then progresses to study the optical fiber-receiver cavity interface in section 6.2. Once the temperature results of the analytical and numerical models are verified, the thruster performance of the final design is presented in section 6.4.

The first ray tracing and heating was studied for the baseline model with corrugated cavity surface. It was found that the temperature of the heat exchanger cavity with and without corrugation varied by 0.04 % since the added mass of the corrugation summed up to 4.1300e-05 Kg. Also, a homogeneous temperature throughout the heat exchanger was achieved which concluded that the temperature due to the cavity shape remained unaffected at this scale. This resulted in proceeding with a plain cavity surface instead.

6.1. Heat Exchanger

This section begins with a brief introduction and reasoning for the selection of the software page. It continues to focus on three Comsol models and discusses the previously mentioned main models in depth. The number of optical fibers selected for the numerical analysis is based on the analytically calculated power output study done in chapter 4.

There are several software packages available to trace the solar rays in optical systems. Only two of the available tools were selected as possible options - SolTrace and Comsol 5.3A, these being the validated software packages. SolTrace is a software tool and the code uses Monte-Carlo ray-tracing methodology for the concentrated solar energy in complex optical systems and determines its optical performance based on the interaction of the solar ray intensity with the system. This open source project has been developed at the National Renewable Energy Laboratory (NREL)[68]. The ray optics module in Comsol offers an effective calculation of ray trajectories for complicated systems. Apart from ray tracing, Comsol offers multiphysics coupling of other modules such as heat transfer in solids and fluid, solid mechanics, wave propagation, etc. with the optics module. This feature makes Comsol the clear winner and therefore, it has been selected to proceed with the thermal modeling and analysis of optical fibres integrated with the heat exchanger.

6.1.1. Ray Tracing Model

For the purpose of finalizing the cavity depth required for the heat exchanger, it is important to see whether the variation in cavity depth affects the power deposit on the bottom wall of the cavity and also the intensity distribution over the walls. The figure 6.2 shows 8 optical fibers ray tracing into a rectangular cavity. The intensity of the rays and power deposited at the bottom surface of the cavity is then achieved as the output.

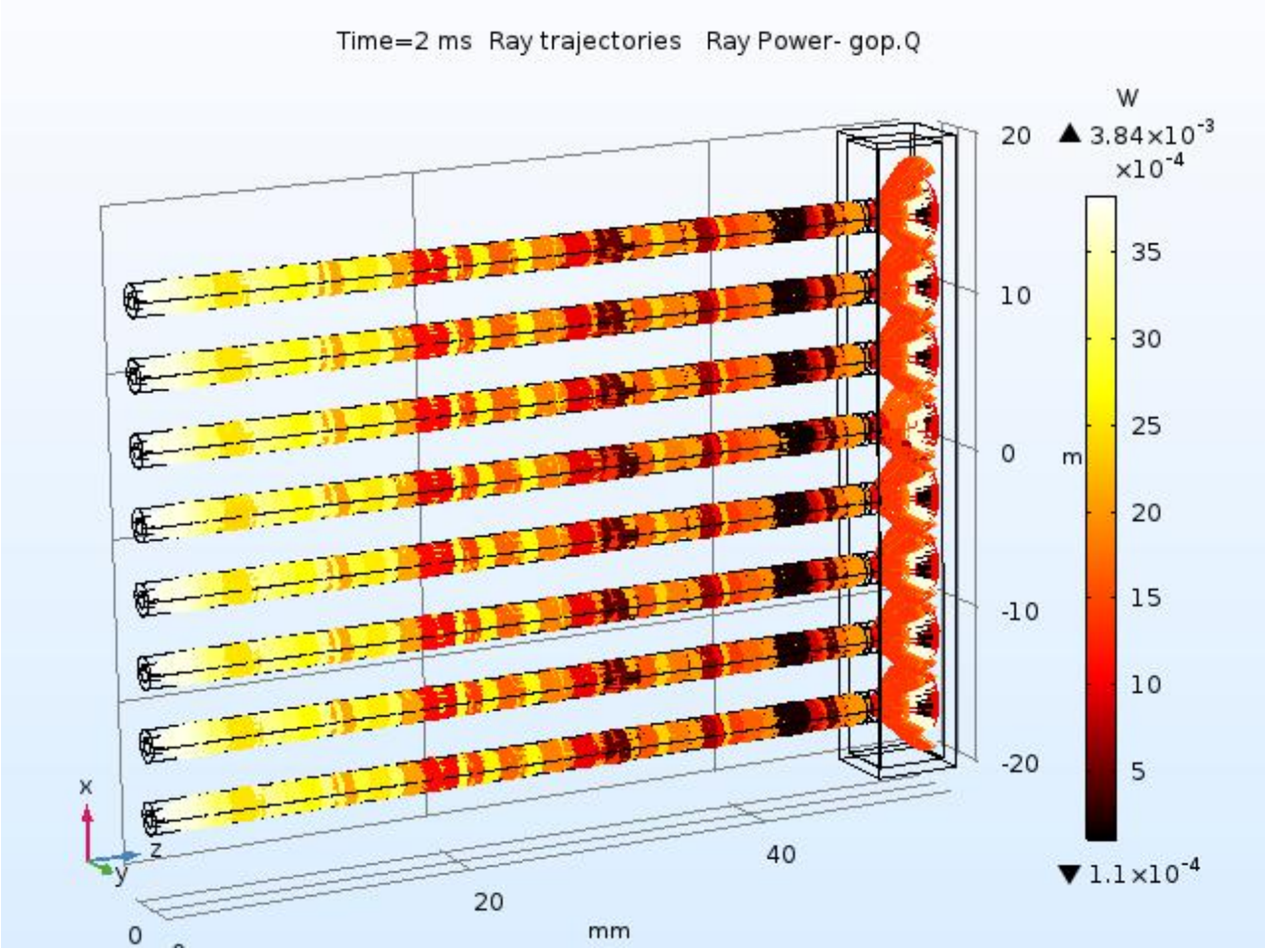

Figure 6.2: Ray tracing of 8 optical fibers into the cavity and freezing at the bottom wall

The subplots in 6.3 depict the heat flux density distribution over the inner wall cavity of the heat exchanger using 8 optical fibers transmitting a power of 7.67 W each at the inlet. The power transmitted at the output end of the fiber depends on the transmittance factor. This plot shows the variation of heat flux density and accumulated power with an increase in the height or distance of the bottom cavity wall from the outlet of the optical fiber. It is observed that at 1.5 cm cavity height the power is highly concentrated at smaller regions with a maximum heat flux density of 1.06^7 W/mm^2. As the distance between the cavity and outlet tip of the fiber is increased, a more even distribution of power is observed but with lower concentration. Clearly, the shorter the distance between both surfaces, the more is the heat flux density. One important aspect of ray intensity and power deposition observed during this study is that as the height increases, the power deposited exactly on the cavity surface parallel to the outlet of the fiber, decreases. A reduction in deposited power is detected as the height increases after 5.5 mm by 1.5 %. Hence, this value will be considered as the upper limit. This is due to the heat rays impinging on the side walls of the cavity first.

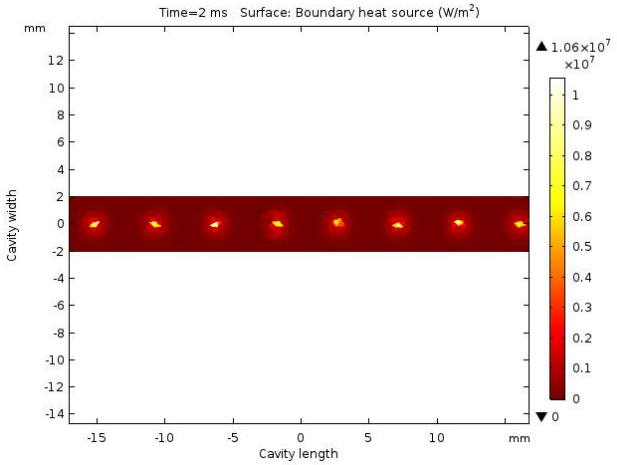

(a) Heat flux density at cavity height of 1.5 mm

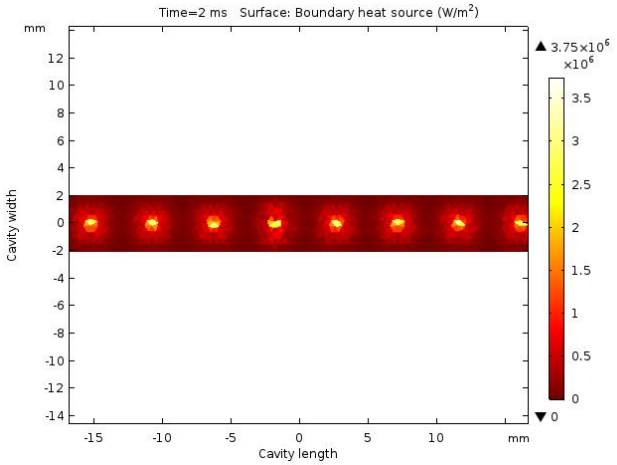

(b) Heat flux density at cavity height of 2.5 mm

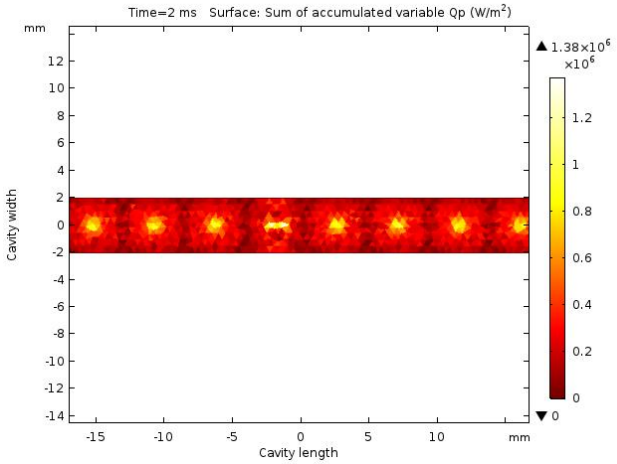

(c) Heat flux density at cavity height of 3.5 mm

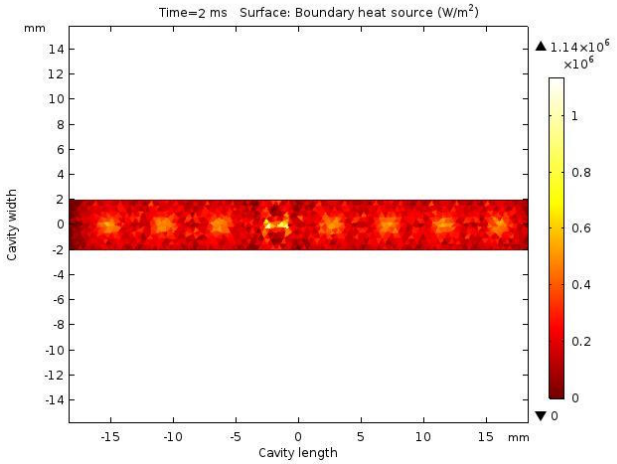

(d) Heat flux density at cavity height of 4.5 mm

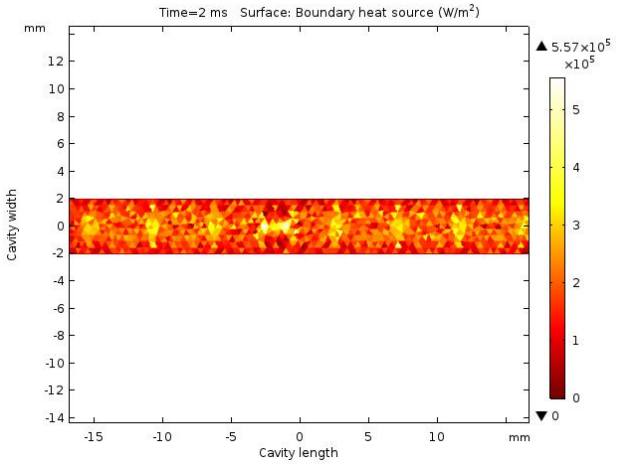

(e) Heat flux density at cavity height of 5.5 mm

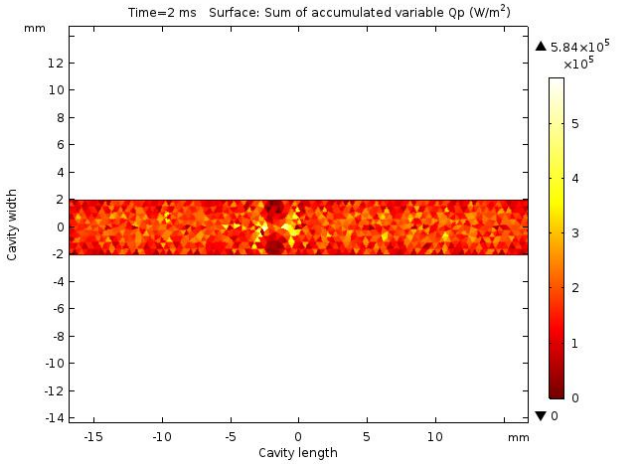

(f) Heat flux density at cavity height of 6.5 mm

Figure 6.3: Heat flux density at the bottom cavity with respect to change in cavity height using 8 optical fibers.

In section 6.1.2, the ray heating multiphysics feature was incorporated to determine the variation of temperature on the cavity due to ray heating and how they affect each other through a bidirectional, or two-way, coupling. In order to compute the temperature distribution along the cavity length and width and to solve for the ray trajectories, the Ray Heating interface and Bidirectionally Coupled Ray Tracing study step are used.

The coupling between the geometrical optics and heat transfer in solids is based on the absorption coefficient of the participating surface when the rays pass through the object. The intensity and power of the rays are then determined using the following equations.

$$I = I_o e^{\left(\frac{-2K_o kL}{n}\right)} \tag{6.1}$$

$$P = P_o e^{\left(\frac{-2K_o kL}{n}\right)} \tag{6.2}$$

Here L is the optical path length and is characterized as a product of the speed of light in vacuum and time step (ct). n and k are the real and imaginary numbers of refractive index respectively. K_o is the free-space wave number which is defined as a function of the free-space wavelength, λ_o.

$$K_o = \frac{2\pi}{\lambda_o} \tag{6.3}$$

In the ray heating model, the diffuse surface (radiation) properties were given to the cavity walls with their respective emissivities.

6.1.2. Ray Optics Modelling in COMSOL

An initial modeling of an optical fibre in Comsol has been done only using the ray optics module to generate a view of the rays emitting from the optical fibre and impinging on the cavity base wall (6.1.1). This model will now serve the purpose of checking the transmittance, validate the number of optical fibres needed for the system, study the variation with the arrangement of these fibres over the cavity to ensure even distribution of heat flux and the final cavity wall temperature of the heat exchanger.

Ray Heating Model Definition

The selected optical fiber in section 4.6 is modelled in Comsol using solid concentric cylindrical pipes with bend curvature as shown in the figure 4.6. This bend curvature of the pipe was varied for a range of 5 mm to 80 mm bend radius using a parametric function called sweep parameter. This was done to study the transmittance through the fiber of fixed diameter with a change in bend radius. The relationship between the bend radius and transmittance is studied to prevent extreme losses during the transmission of solar energy through the fibers into the receiver. One of the plots is shown in figure 4.5.

Geometrical and Material Input Parameters

1. The material for each fiber layer was given as input along with the temperature dependent refractive index equation for the fiber.

2. The rays are released from a point source at one end of the pipe with a cone angle of $\pi/6$ which is defined as the acceptance angle of the fiber. The point source is given a power of 7.67 W as determined from the optical system calculations in chapter 4 section 4.7.

3. The dimensions of the heat exchanger obtained from the Matlab thermal model was geometrically imported from Catia with its bottom surface acting as the wall where the power is made to deposit using the wall node with the deposited ray power subnode.

4. The surrounding medium (exterior) is considered to have a refractive index of 1 assuming either vacuum or air.

5. Numerical aperture of the fiber is given as 0.50.

6. The remaining surfaces of the heat exchanger outer walls is considered to be thermally insulated.

Mesh Element Quality and Size

For validating the model in Comsol, the mesh resolution and mesh element quality will be discussed in this section. Undoubtedly, a low mesh quality and resolution lead to inaccurate results as it can affect the mesh element shape when dealing with large forces acting on the model and can cause convergence error as well. The mesh quality represents the shape of an element and is expressed between 0 and 1, with 1 characterizing a perfectly shaped element. Although a structured mesh (hexahedron) is always preferred over unstructured mesh as the former, in general, is known to offer higher resolution and convergence. However, due to the intersection of the circular optical fibers and cavity surface, refinement of the mesh was obtained efficiently for an unstructured tetrahedral mesh. The default 3D mesh element of Comsol, free tetrahedron, has been used for the meshing of the model. The mesh quality measure are described for the following fine to a coarse mesh of sizes 0.1 mm, 0.25 mm and 0.5 mm (minimum element size). The fine meshing is limited to 0.1 mm due to the computer's 4GB of RAM which is not feasible to run large files as more elements means more grids to be computed, therefore, requires more memory. For the optical fibers, the meshing is maintained at 0.01 mm mesh size due to narrow distance between the core and the cladding and thus smaller mesh size around the curved sections are considered.

Table 6.1: Mesh quality for bidirectionally coupled ray tracing model

Measures	**Quality measure**						**Definition (Comsol 5.3A)**
	0.1 mm		**0.25 mm**		**0.5 mm**		
	Min.	**Mean**	**Min.**	**Mean**	**Min.**	**Mean**	
Skewness	0.2795	0.79	0.415	0.703	0.55	0.613	Measure of the equiangular skew of the element, 0 indicates an equilateral cell (best quality) and a value of 1 indicates a completely degenerate cell.
Volume versus Circumradius	0.644	-	0.497	-	0.40	-	Quotient of element edge length and element volume.
Volume versus Length	0.644	-	0.47	-	0.38	-	Quotient of element edge length and element volume.

Table 6.1: Mesh quality for bidirectionally coupled ray tracing model

Measures	Quality measure						Definition (Comsol 5.3A)
	0.1 mm		0.25 mm		0.5 mm		
	Min.	Mean	Min.	Mean	Min.	Mean	
Maximum Angle	0.715	-	0.3417	-	0.391	-	It shows how much larger is the angle of an element is from the largest angle of an optimal element. Quality value is 1 for a case with no angle greater than the largest angle.
Computational Time	18499 s		9360 s		4320s		

In the table 6.1 the minimum value is the least value found for the respective quality measures for a mesh size. Mean is the average of the overall quality values of the total elements formed for the entire model volume. The domain elements for the finest meshing are about 8.02 million, - boundary elements and - edge elements. The time taken for simulation is much longer than the coarse meshing and has an absolute tolerance of 10E-6 as the main objective of the simulations is to reduce the error between the real and approximated solution. The minimum quality value accounts to 1 - 1.5 percent of the total elements which is attributed mostly to the sharp geometry. The overall mean quality is no less than 0.79 which means the majority of the mesh elements remain in the average domain. Thus the quality of the selected mesh affirms less accurate results. The convergence plot shows the error vs iteration number for the selected mesh size. Here the error in the plot shows the estimated relative error after each iteration. The convergence plot in the figure 6.4 shows that the solution diverges slightly and begins to converge again and eventually converges post 22 iterations. Similar plots were attained from in-built ray tracing examples in Comsol using time-dependent and segregated solver with smaller divergence. Even though the error at the end is observed to be extremely low, there is still a divergence and this could perhaps be due to insufficient meshing but the computational power required for the finer mesh is constrained because of the RAM.

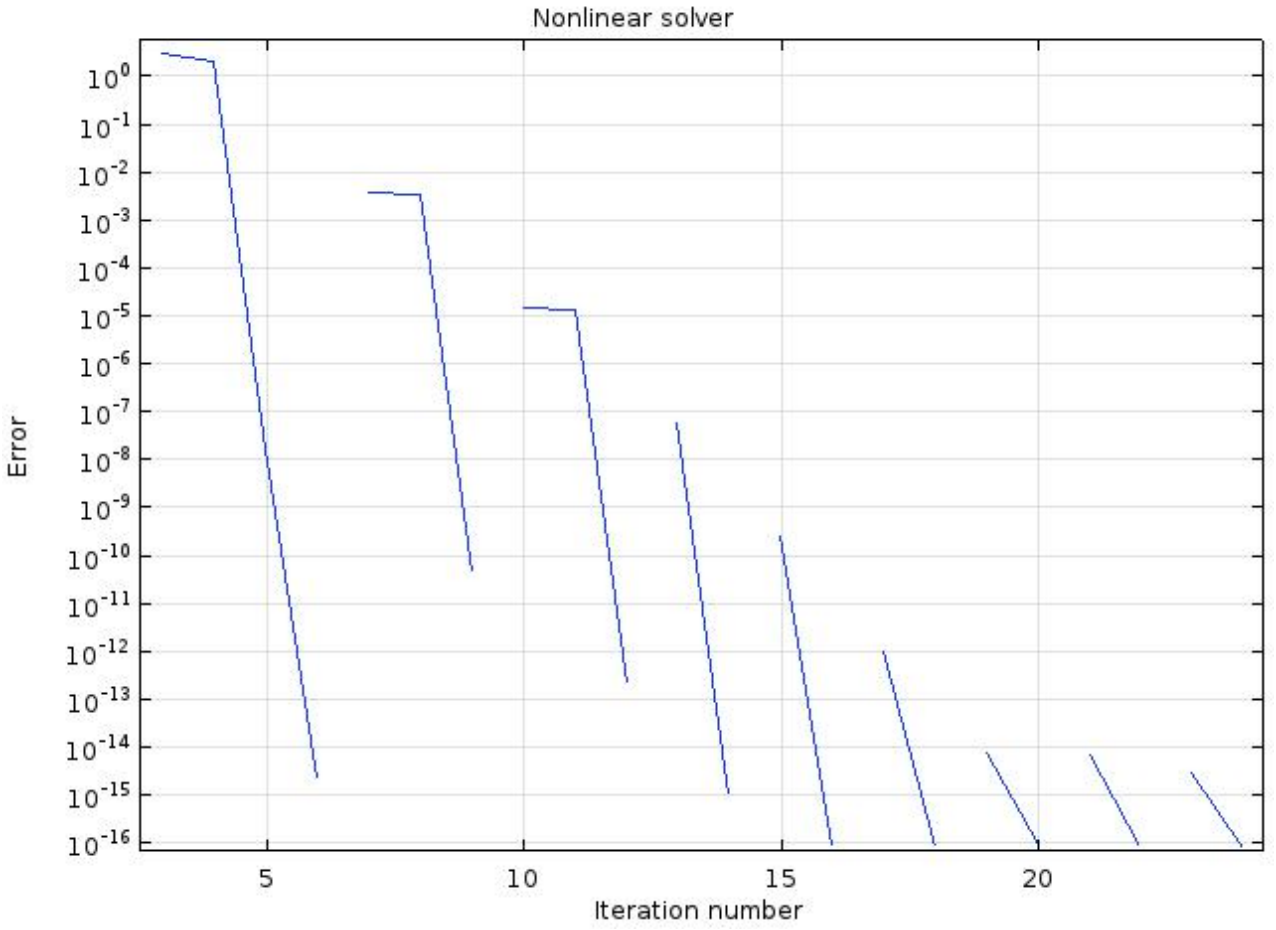

Figure 6.4: Convergence plot for a mesh size of 0.1 mm in Ray heating model

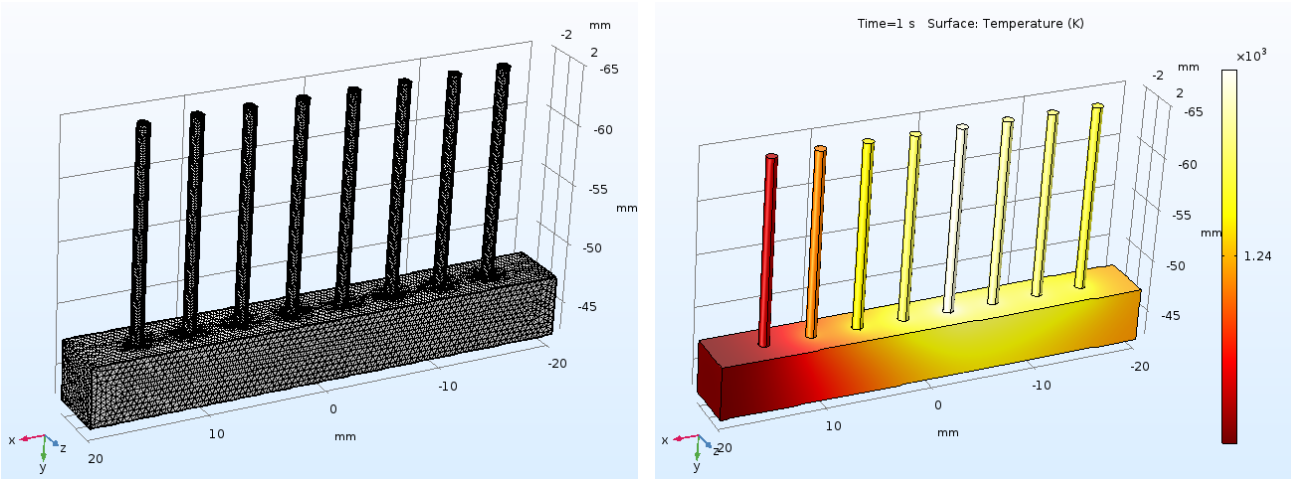

(a) Tetrahedron Meshing

(b) Temperature 3D plot

Figure 6.5: Meshing and temperature result for coupled geometrical ray tracing and ray heating

The figures 6.5 and 6.6 display the mesh, surface temperature and temperature contours of the heat exchanger and optical fibers respectively. The isosurface temperature contour helps to visualize the variation of temperature flow/ distribution along the heat exchanger where the temperature is quantified as constant at the end but since a homogeneous temperature is attained, no variation is noticed. It can be observed that the final temperature attained with 8 optical fibers is about 1240 K in the cavity.

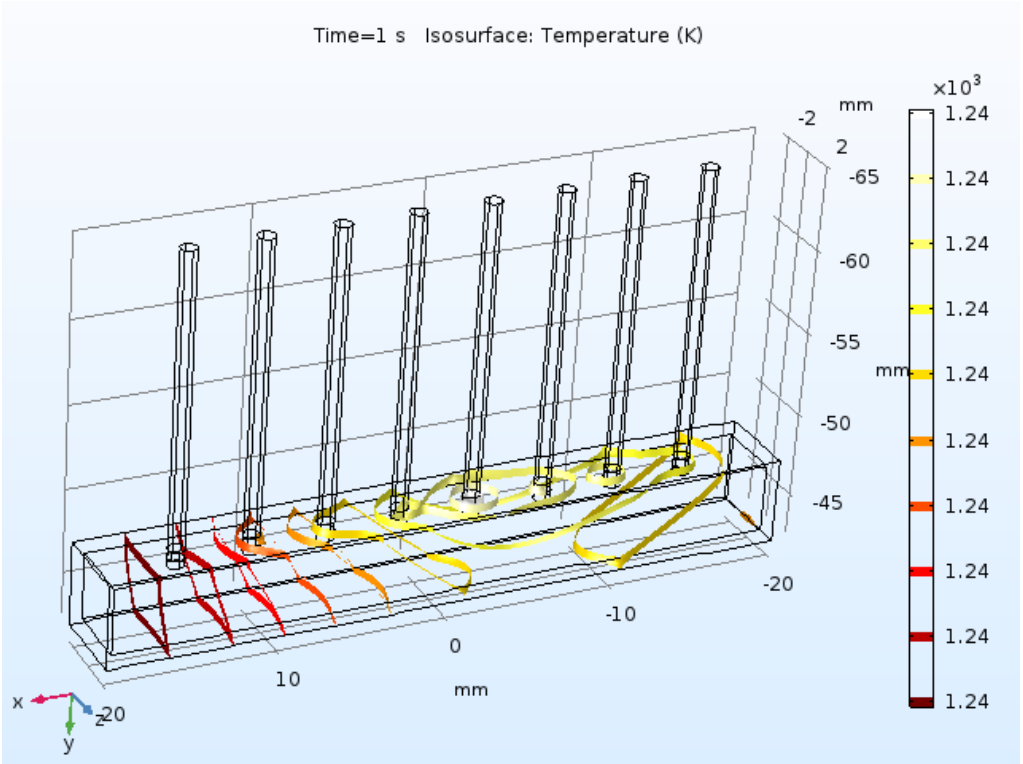

Figure 6.6: Temperature contour 3D plot

The temperature values attained for the optical fibers will be neglected in the ray heating model as the diffuse surface properties for the jacket layer of the fiber was not given as input due to insufficient memory to run the simulations.

6.1.3. Conjugate Heat Transfer Model

This section will describe the conjugate heat transfer model which simulates the fluid flow in the micro-channels of the heat exchanger. The model takes into account the heat transfer taking place between the fluid and channel walls using convection, conduction and surface-to-surface radiation between the optical fiber tip and cavity inner walls. The wall temperature obtained from the ray heating model is given as a temperature boundary condition on the inner cavity walls

Boundary Conditions

This set of nonlinear elliptical governing equations has been solved subject to following boundary conditions:

1. At the micro-channel inlet, mass flow rate are assumed uniform and constant and pressure is set to 5 bar.

2. At the fluid-solid interface, the velocity in the y direction is zero, while the fluid flow satisfies velocity slip wall condition.
3. At the micro-channel outlet (x=L) the exit pressure is taken as zero and the diffusion flux in the direction normal to the exit is assumed to be zero for velocity.
4. Diffuse surface property is applied to the cavity walls.
5. The wall temperature of the cavity is set to 1240 K.

Mesh Element Quality and Size

For the conjugate heat transfer model that uses non-isothermal flow (multiphysics model) to couple the flow within the channels and heat transfer between the flow and the channel walls via convection, the following figures depict the convergence study of varying mesh size and quality.

In the figure 6.7 the mesh sizing is provided as a sweep parameter for the study. The maximum and minimum element size is varied from a coarse to fine meshing. The iteration begins from the start once one solution is generated for first meshing input and is plotted continuously. The segregated solver is used for this model as two parameters are studied for convergence i.e the velocity and pressure of the fluid and the temperature. Again, error in the plot shows the estimated relative error after each iteration. It must be noticed that the convergence is insignificantly varying for the finer mesh (3rd) compared to the coarse mesh. With the improvement in mesh quality with finer meshing, the computational time subsequently increases. The computational time for minimum element size of 0.72 mm, 0.4 mm and 0.16 mm was found to be 22 minutes 7 seconds, 56 minutes, and 1 hour, 26 minutes respectively. With the convergence rate remaining more or less constant after a point, the mesh quality does vary and is given preference in this study and therefore, a finer meshing is incorporated for accurate results as it is within acceptable computational time. The mesh element sizes (table 6.2) and convergence plot (figure 6.8) are presented next.

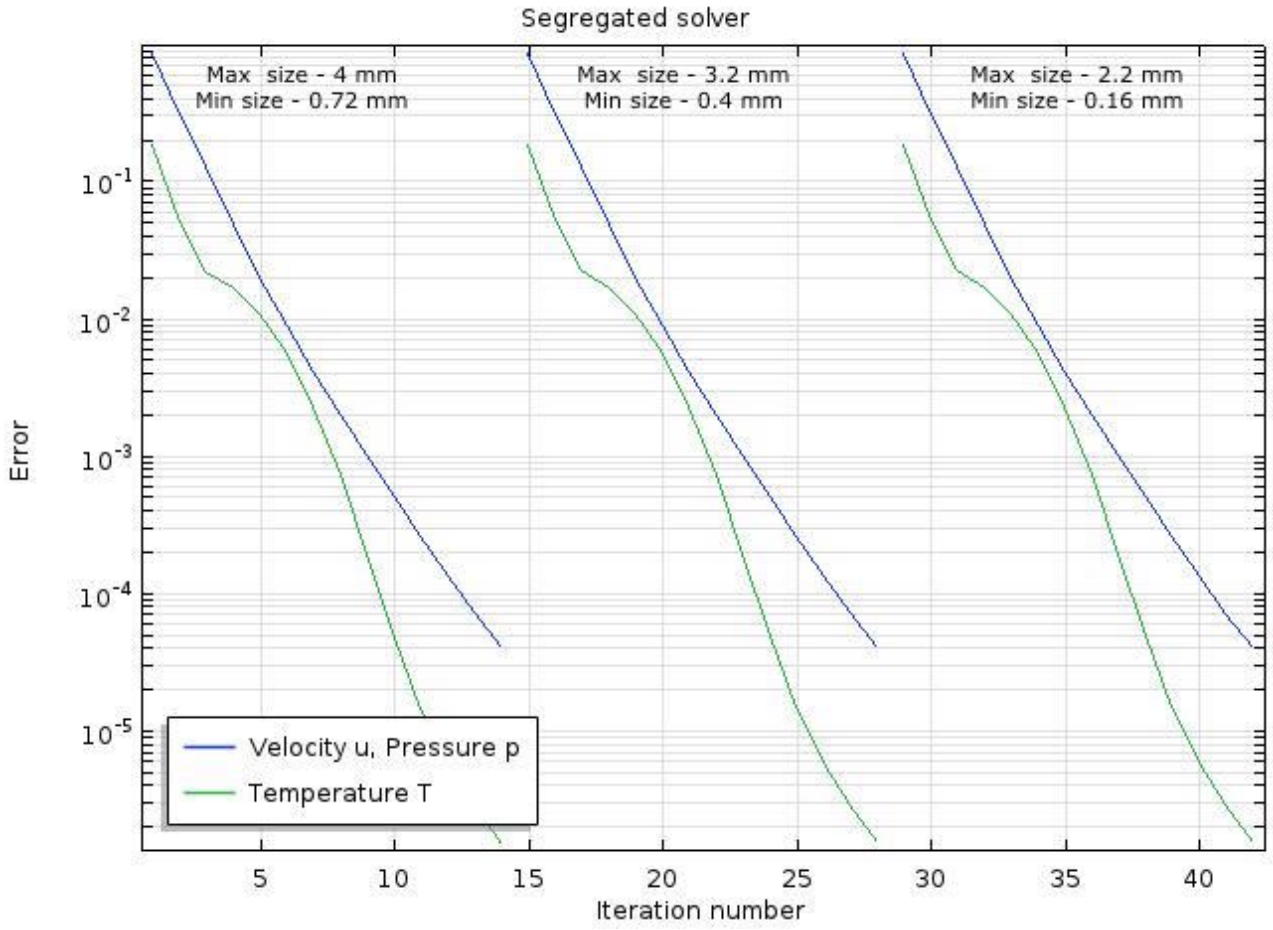

Figure 6.7: Mesh convergence study for the conjugate heat transfer model for varying mesh size

Table 6.2: Mesh size and quality for the conjugate heat transfer model

Size [mm]	**Size Insulation + HE**	**Channel Domain**	**Channel Walls**	**Corner refinement**	**Boundary Layer Trimming angle[deg]**
Maximum Element size	0.8	0.388	0.388	0.1	50
Minimum Element size	0.08	0.0597	0.0597	-	240
Mesh Quality	0.7999				
Computational Time	1 hour 56 minutes				

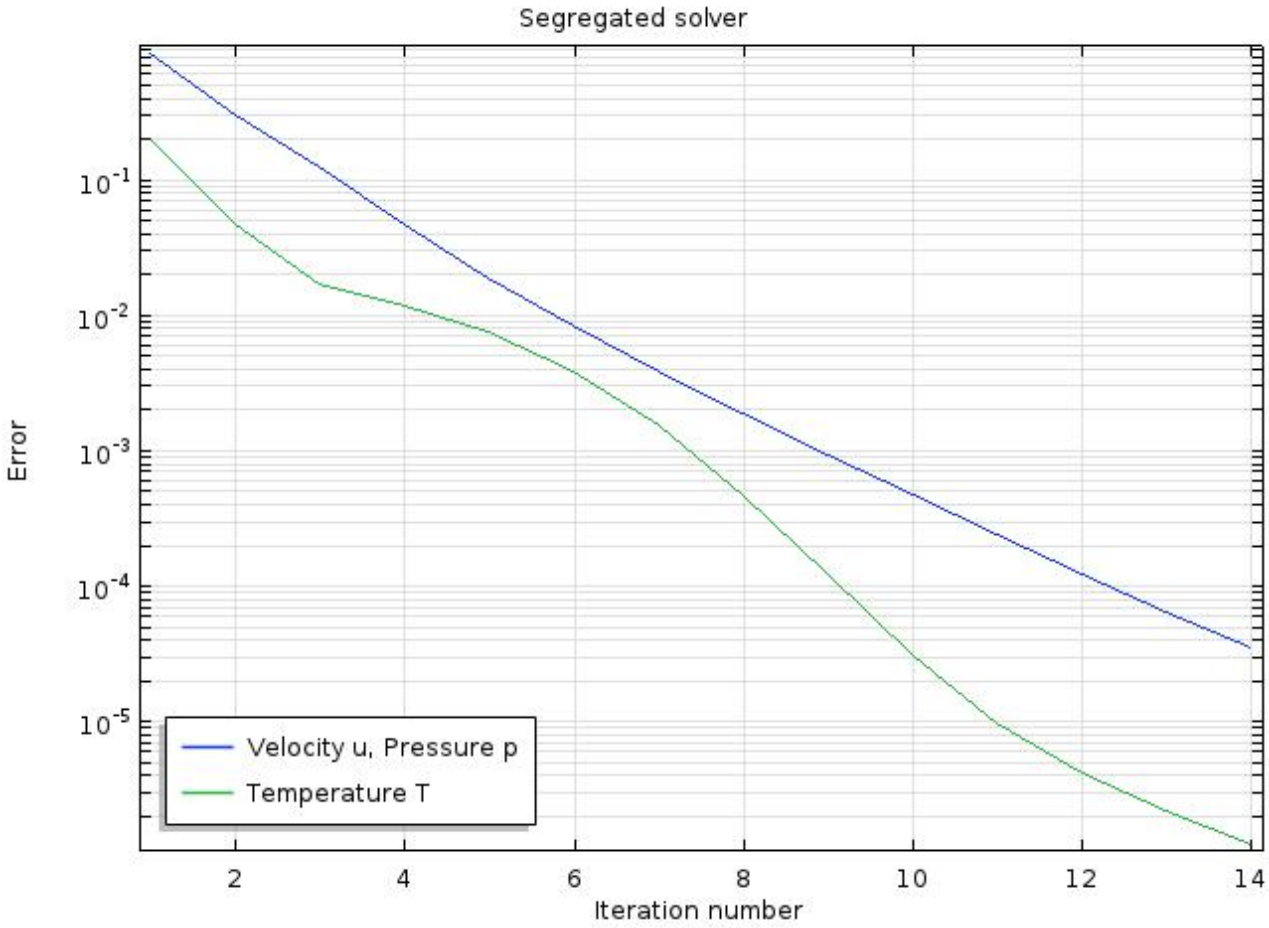

Figure 6.8: Convergence plot for conjugate heat transfer model

For a mesh quality higher than 0.79, i.e extremely fine meshing with minimum element size for heat exchanger domain as 0.06 mm and minimum element size for the channel domain as 0.00117 mm, the difference in result for the temperature is 3.09 % whereas the computational time increases by almost 6.7 times (converges within 10 iterations). Since the results are not drastically varying and also the computational time is acceptable, the mesh size mentioned in table 6.2 is used for this study.

With the cavity wall attaining almost 1200 K, the boundary condition was set to a 1200 K temperature for the bottom wall. The figures below represented the steady state temperature of the heat exchanger with water. The mass flow rate per channel, inlet pressure, and outlet pressure was set to 2.4679e-05, 5 bar and 0 bar respectively. As can be seen in figure 6.10, the temperature of the channel wall reaches to almost 1198 K and the value obtained from the analytical thermal model is 1259.7 K.

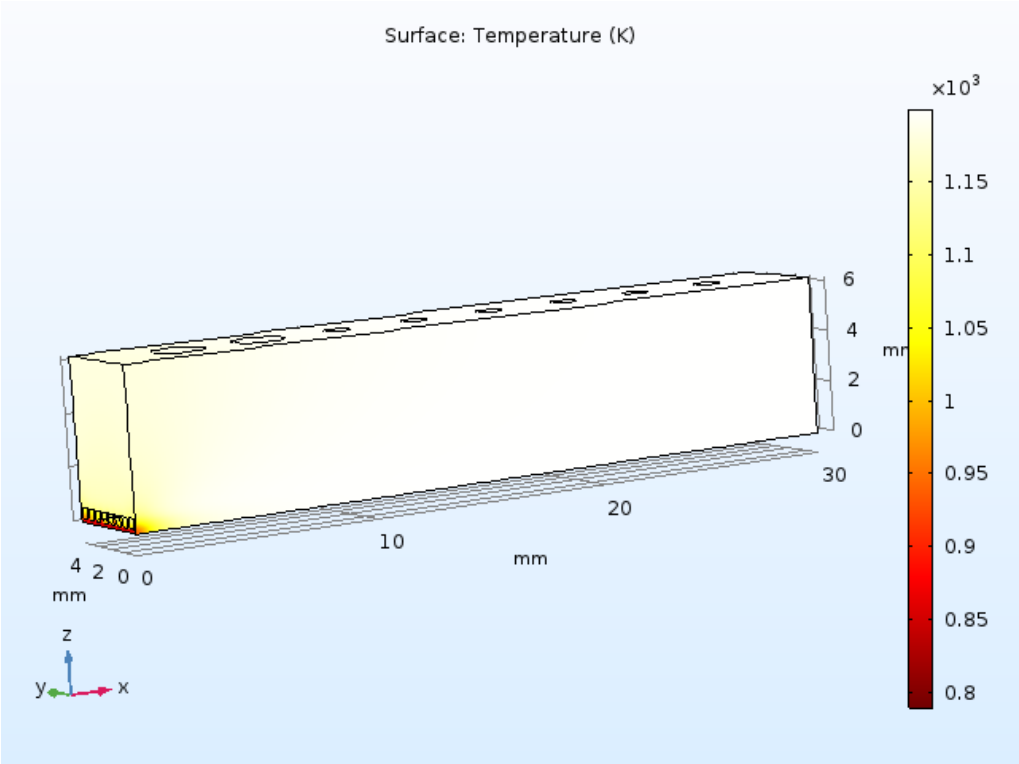

Figure 6.9: Temperature plot (3D) of the heat exchanger due to conjugate heat transfer

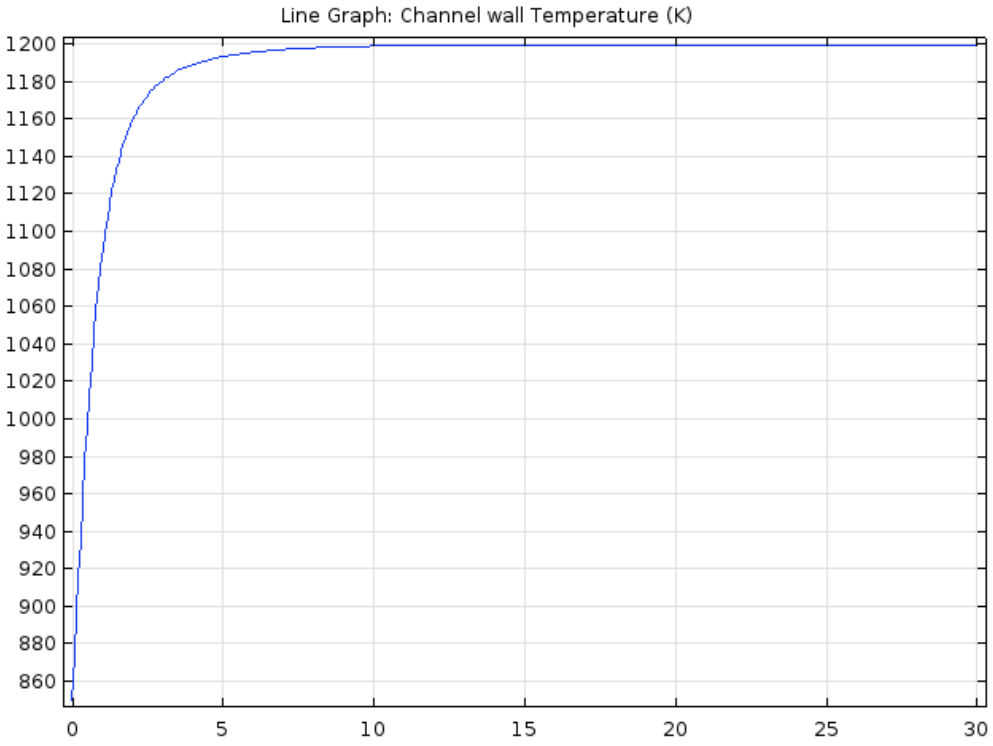

Figure 6.10: Channel wall temperature with respect to channel length in steady state

6.2. Fibre Optic-Receiver Coupling

The interface between the optical fiber and receiver is a critical junction and requires proper connection to prevent heat loss. Before delving into the coupling concepts for the intersection, the need for investigating the mentioned interface will be established in the sub-section 6.2.1. For this purpose, two important parameters, that will form the basis of the fiber-receiver coupling, are studied namely, intensity on the inner cavity surface and the tip end temperature of the fiber. Once the necessity of a coupling concept is realized, three coupling concepts will be presented and numerically analyzed in sub-section 6.2.2.

6.2.1. Optical Fiber Temperature due to Hot Cavity

In this section, a sectional 2D heat transfer model has been simulated in Comsol considering radiative and conductive modes of heat transfer. The material properties of the cavity and fibers have been taken from the materials table 4.6. The inner wall of the cavity is considered to have a boundary temperature of 1200 K and diffuse surface properties are added for radiative heat transfer inside the cavity. In this model, the fiber consists of the core, the cladding layer and a layer of coat/jacket. The ambient surrounding is considered be at 293.18 K. The sub-figures in 6.19 show the temperature contours for a time-dependent study done in Comsol. The contours help in visualizing the progression of temperature from the cavity to the optical fiber with time.

The bare fiber can be seen to reach the same temperature as the cavity without any insulation. Due to molybdenum's high thermal conductivity, the cavity is seen to be heated in 0.1 seconds for a wall thickness of 0.5 mm. The heat conducted to the fiber through the jacket and cladding layers is clearly slower due to its low conductive properties. However, over a long period of time, a uniform temperature over the entire system is observed.

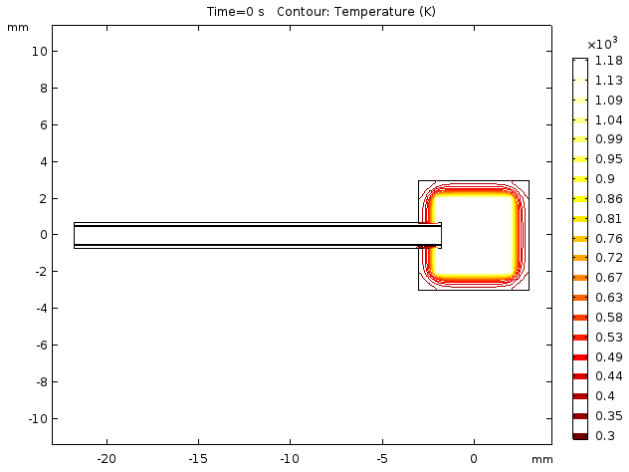

(a) Contour temperature at 0 s

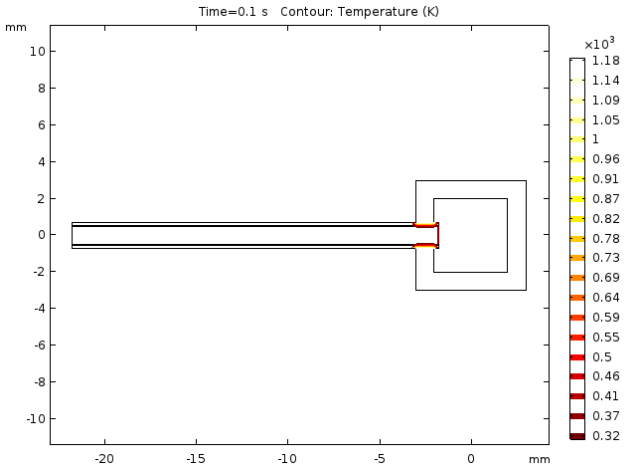

(b) Contour temperature at 0.1 s

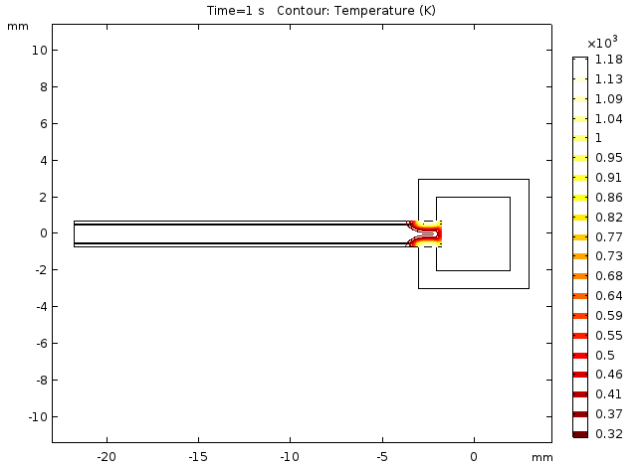

(c) Contour temperature at 1 s

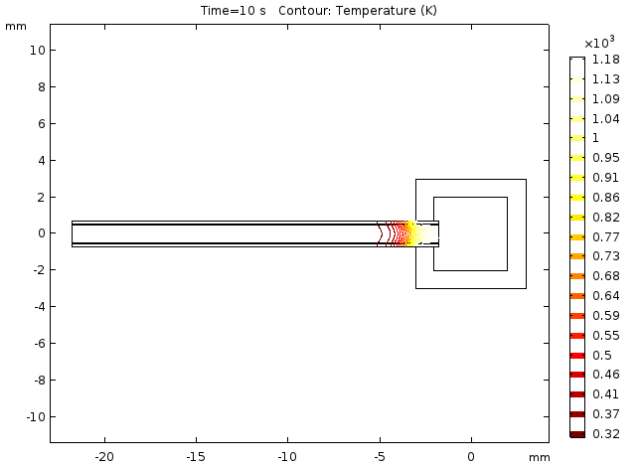

(d) Contour temperature at 10 s

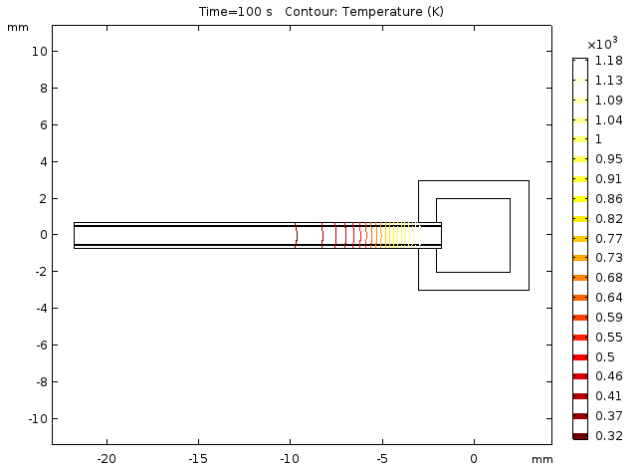

(e) Contour temperature at 100 s

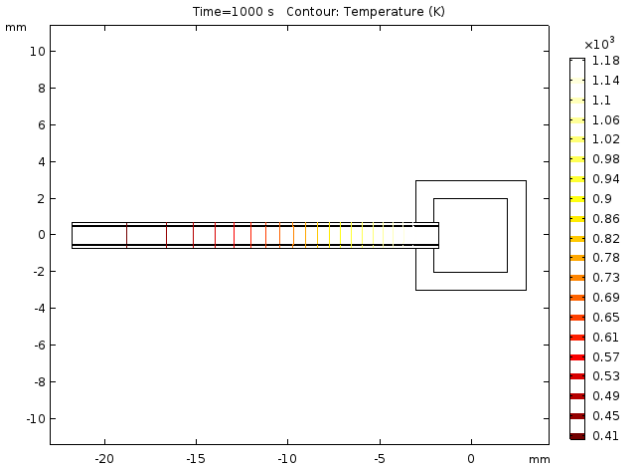

(f) Contour temperature at 1000 s

Figure 6.11: Temperature contour of the optical fiber - receiver for transient and steady state heat transfer.

6.2.2. Fibre Optic-Receiver Coupling Concepts

The temperatures at the receiver cavity can reach up to 1200 K with about 55 W of power. This high temperature can melt the optical fiber coat and cladding materials and also damage the core. Therefore, it is of utmost importance to look into the interface between the fiber and receiver to prevent low transmission efficiency and complete melting of the materials. As inferred from the figure 6.19, the optical fiber will be subjected to really high temperatures when in contact with the receiver. The core of an optical fiber is known to work fine up to 1000 K [69] but the cladding and jacket material melts due to their low working temperature. Hence, two of the three concepts proposed are based on stripped clad and jacket material and making only the core approach the receiver. Each concept will be explained further and studied simultaneously. The following are the interface coupling concepts:

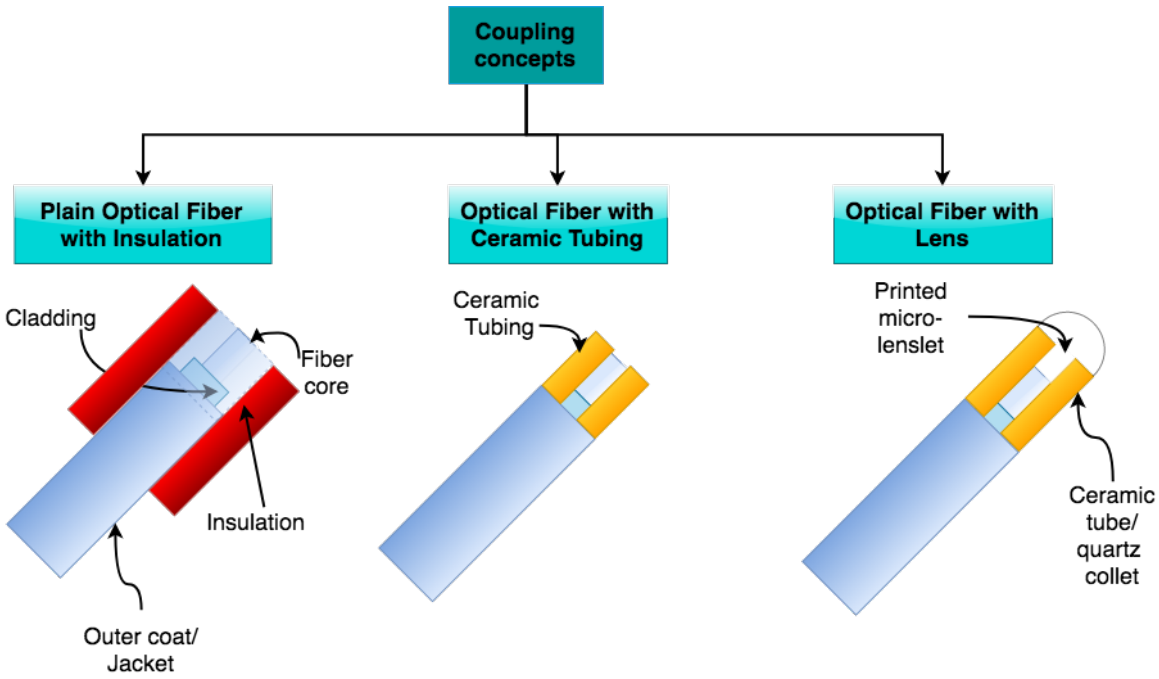

Figure 6.12: Optical fiber and receiver interface concepts

Mesh Quality and Convergence

The 2D model of the fiber is meshed (unstructured) with an element size of 7.9E-4 mm and the heat exchanger and insulation is meshed with an element size of 0.3 mm. The mesh quality of the selected mesh size was found to be 0.88. The mesh and convergence plot of the first coupling concept is shown in the figure below.

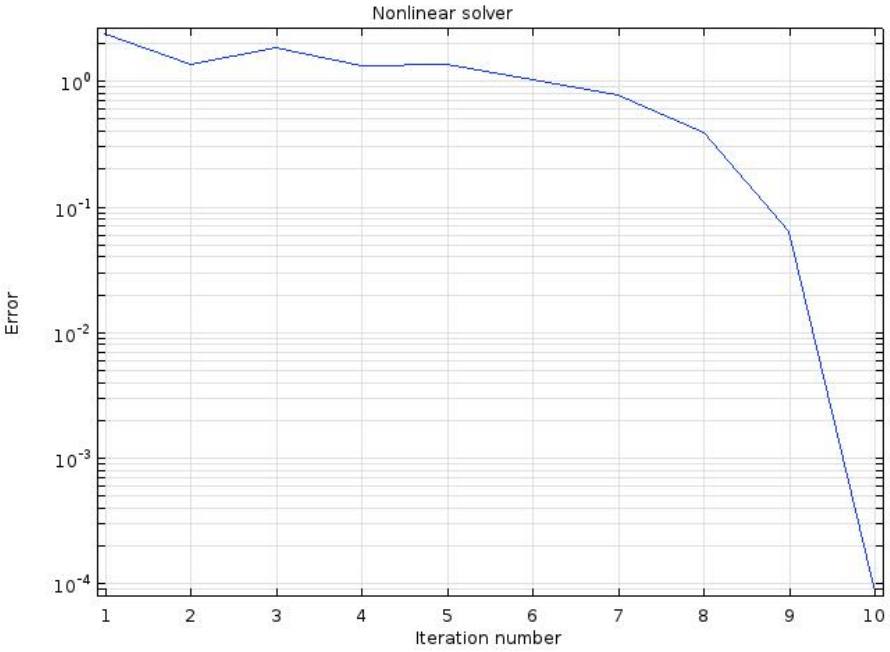

Figure 6.13: Convergence plot for optical fiber and receiver interface concept 1

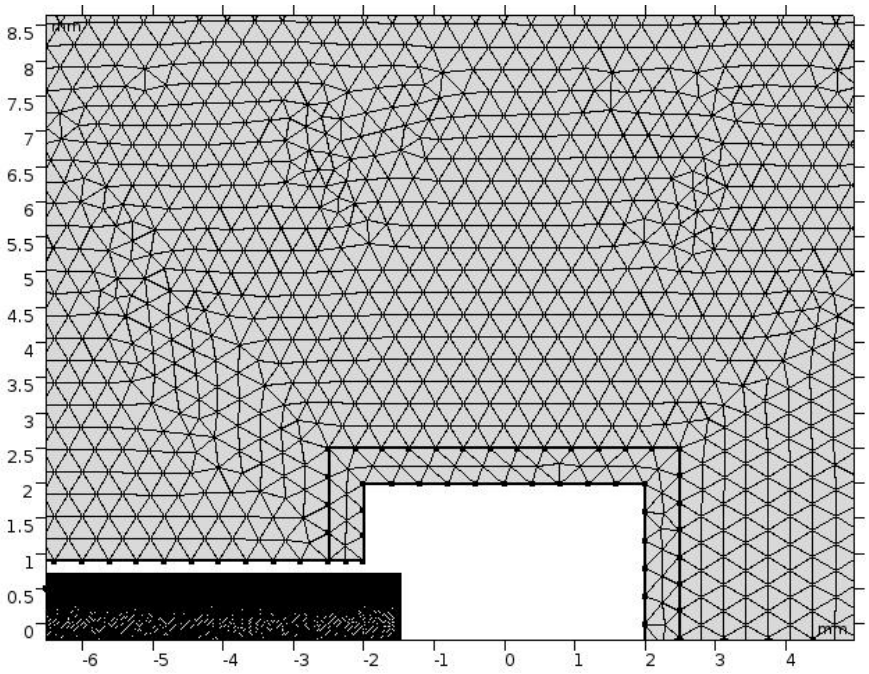

Figure 6.14: Mesh for optical fiber and receiver interface concept 1

Plain Optical Fiber with Insulation

This concept is considered only to compare the heating of the fiber with and without direct contact with the receiver wall. In this concept, the cladding and jacket layer remains along with the fiber core. A thin layer of insulation is added to the optical fiber which is of the same material as the insulation selected for the heat exchanger. In the following plot, the temperature of the optical fiber

tip reaches to at 1089.7 K, which can be seen in figure 6.16, while the cavity is at 1200 K with the pyrogel blanket extending towards the buffer of the optical fiber.

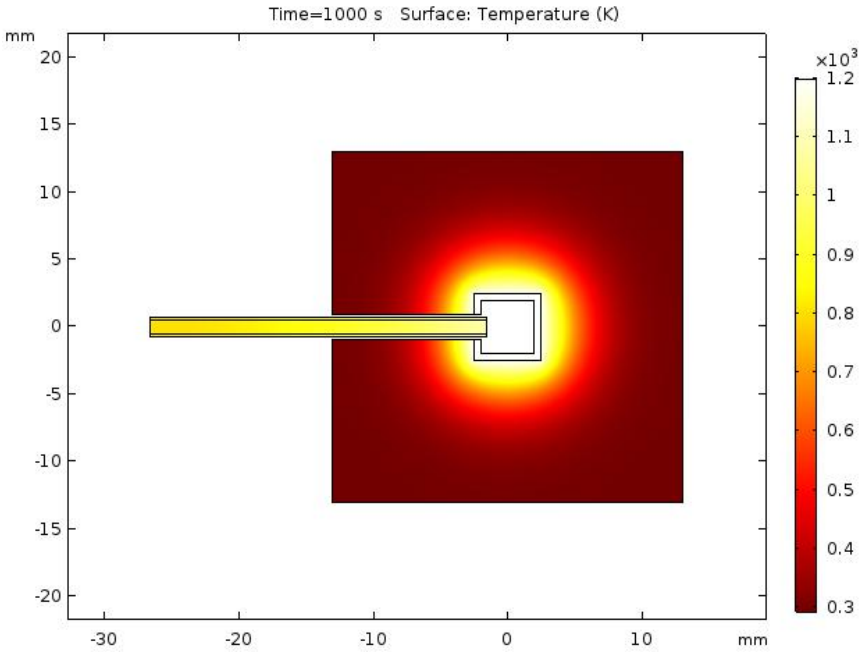

Figure 6.15: Optical fiber and receiver interface concept 1 - Plain optical fiber with insulation

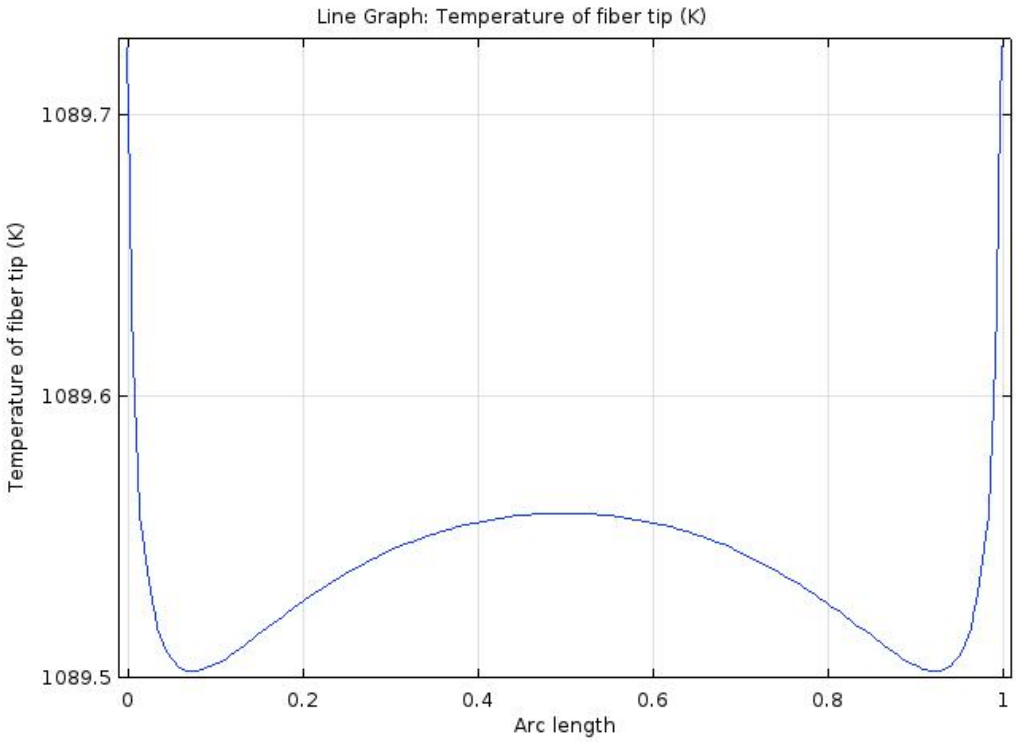

Figure 6.16: Optical fiber tip temperature with insulation

Plain Optical Fiber with Ceramic Tubing

The concept of using a ceramic tubing has been proposed in [69] for offering rigidity and insulation to the core of the fiber that is extending into the receiver cavity such that it doesn't physically come in contact with the cavity wall. Some of the advanced ceramics were investigated to select an appropriate material. From the material property plots shown in B for several advanced ceramics, it can be noticed that alumina (Al_2O_3) and zirconia (ZrO_2) have a lowest thermal conductivity compared to the rest of the materials. To select one material amongst the two candidates, we look into the flexural strength of the material and the clear winner is zirconia. A tube of this material will be used to analyze the effect of heat transfer at the interface. In the surface temperature plot of the heat exchanger cavity along with insulation, and zirconia insulating tube through which the fiber protrudes into the cavity. It must be noted that the insulating tube is not in contact with the cavity-insulation bodies. The tube and fiber are solely getting heated due to radiation. Similar cavity conditions are applied to this model.

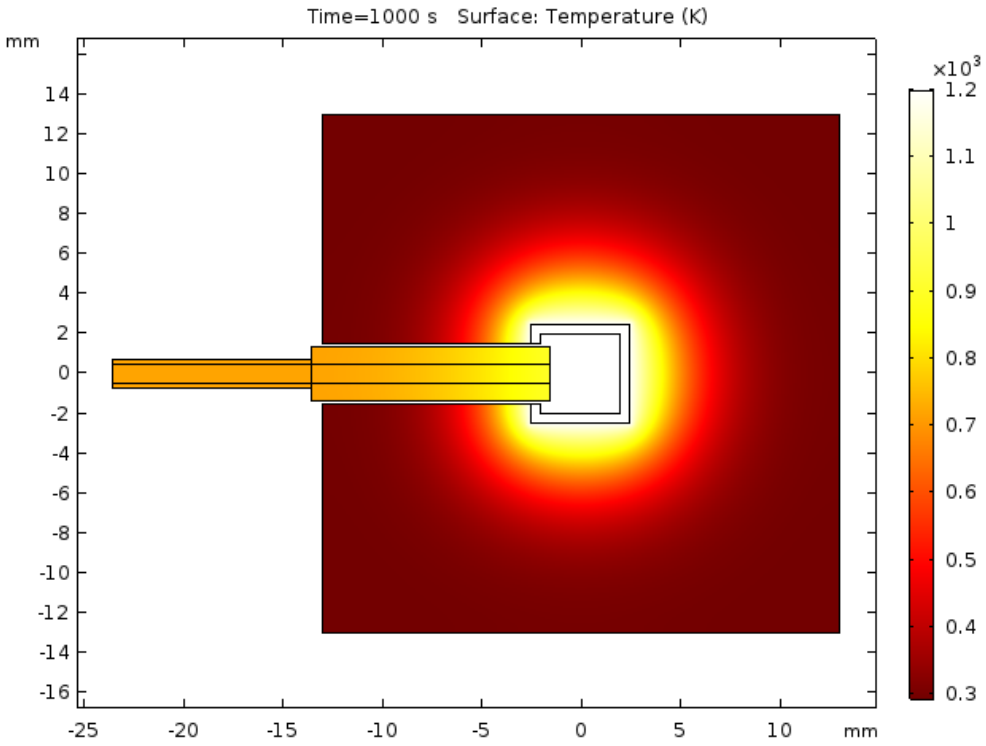

Figure 6.17: The temperature of the coupling system with 2.7 mm thick diameter zirconia tube - Optical fiber and receiver interface concept 2 - Plain optical fiber with ceramic tubing

Using a 2.7 mm dia zirconia tube, it can be observed in the plot 6.18 that the tip temperature of the fiber core is at 1062.5 K and this is still unacceptable for the proper working of the fiber. Increasing the insulating tube diameter will further reduce the temperature but due to geometrical constraints, it will not be possible.

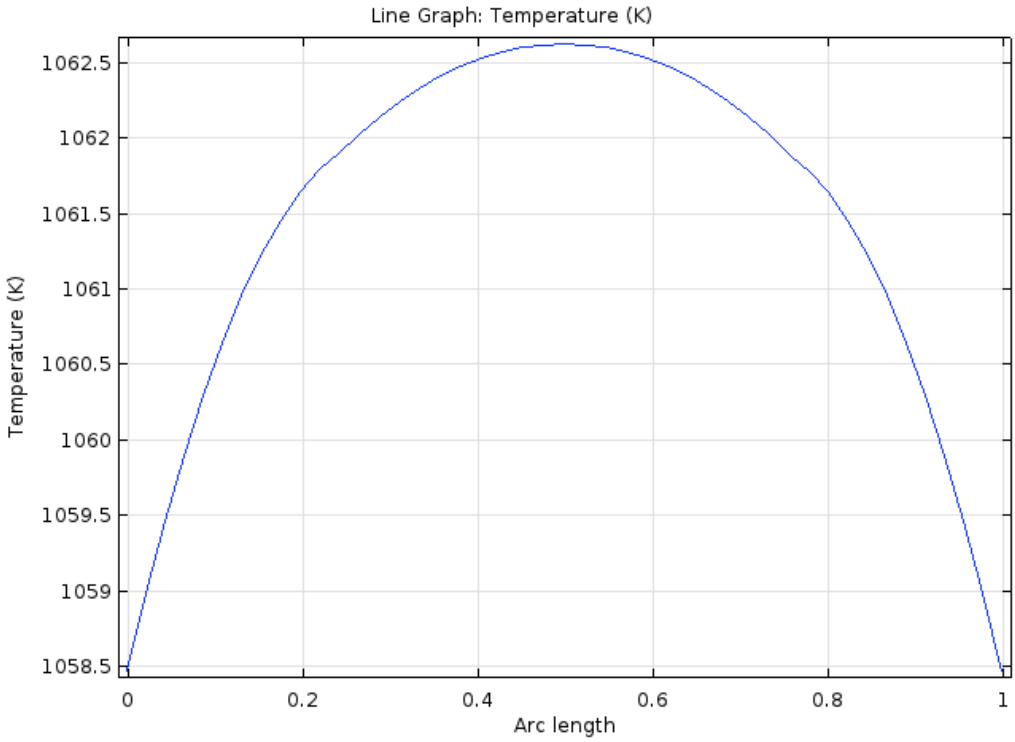

Figure 6.18: Optical fiber tip temperature with 2.7 mm thick diameter zirconia tube

Plain Optical Fiber with Micro-Lenslet

The following concept is not only meant to prevent damage caused to the optical fiber due to high temperatures but also to improve the transmission of the solar energy as the lenslet simultaneously acts as a collimator. The concept involves a quartz collet surrounding just the fiber core and a micro-lenslet formed over the tip of the fiber core like shown in the image below.

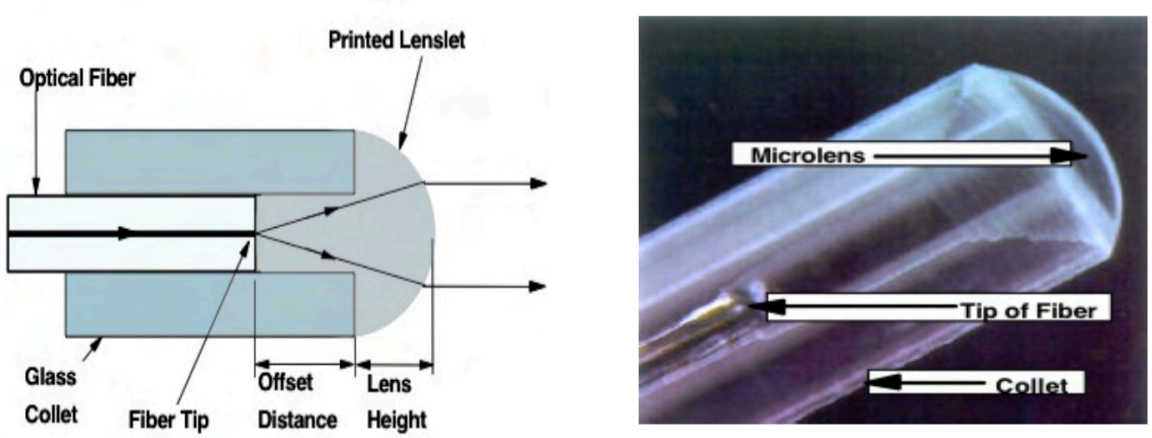

(a) Optical rays through system

(b) Microlenslet printed on the tip of an optical fiber

Figure 6.19: Microlens printed onto a single mode optical fiber with quarts collet [6].

An important criteria for the selection of the collet material is that it must have a refractive index lower than that of the lens material in order to maintain the phenomena of total internal reflection, have a high melting temperature, and comparatively low thermal conductivity. The fiber is usually slid into the collet up to the offset distance as shown in the figure above and is generally glued together. For the collet, quartz seems to fulfill the criteria since it has a refractive index of about 1.39 and a melting temperature of 1983 K. For the lens, the material selected is SiO2-TiO2 hybrid glass since it has one of the highest melting temperatures (1973 K), a low coefficient of thermal expansion of 0.5E-6 K^{-1} and a refractive index that ranges between 1.7 to 2.2 depending upon the composition and weight percentage of each element in this hybrid material. The lens (optical) material can then be deposited into the offset section and up to the required lens height by drop-on-demand (DOD) microjet fabrication. DOD is the most commonly used method for micro-lens fabrication and the production approach is described in [6].

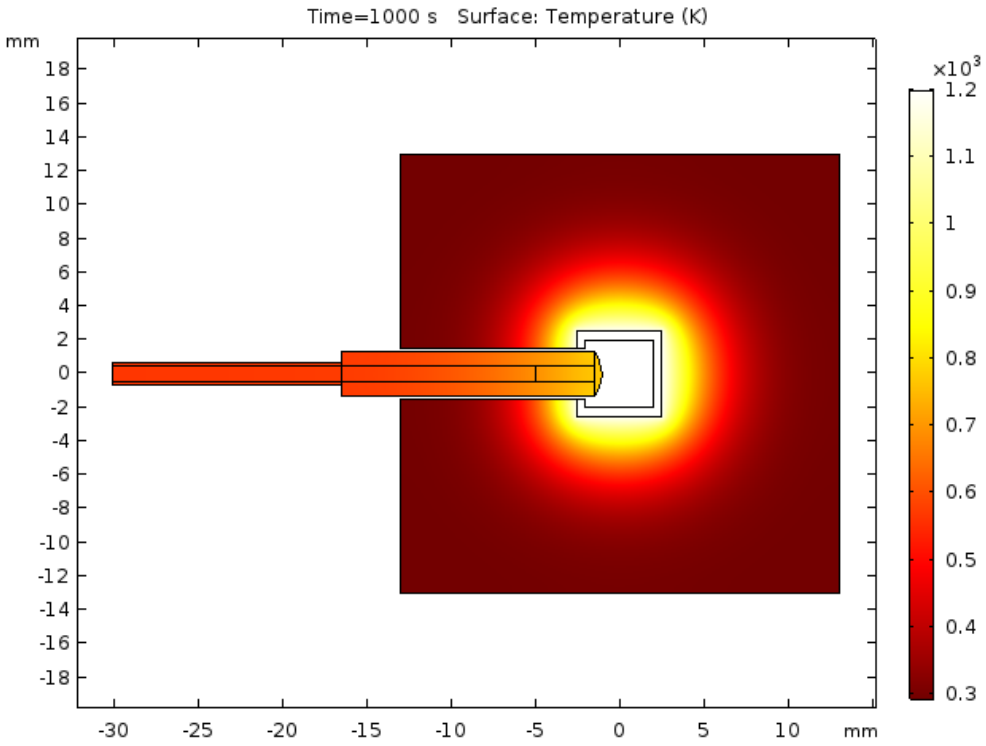

Figure 6.20: The temperature of the coupling system with 2.7 mm thick diameter zirconia tube - Optical fiber and receiver interface concept 2 - Plain optical fiber with ceramic tubing

In the figure 6.20 the surface temperature of the coupling interface is seen which consists of a quartz collet of diameter 2.7 mm (same diameter as insulator tube used in second coupling concept) and an arbitrary offset distance and lens height has been set to visualize the outcome of this concept. It can be noticed that the temperature of the lens material is approximately lesser than 800 K and therefore, the tip temperature of the optical fiber is at 690 K in figure 6.21. Furthermore, the temperature of the buffer material of the fiber is plotted along the length in mm and is shown in the figure 6.22. The immediate temperature at the junction of the optical fiber core and quartz collet is about 572.5 K and the length increase in the negative x-direction (as seen in the surface temperature plot), the temperature keeps decreasing drastically.

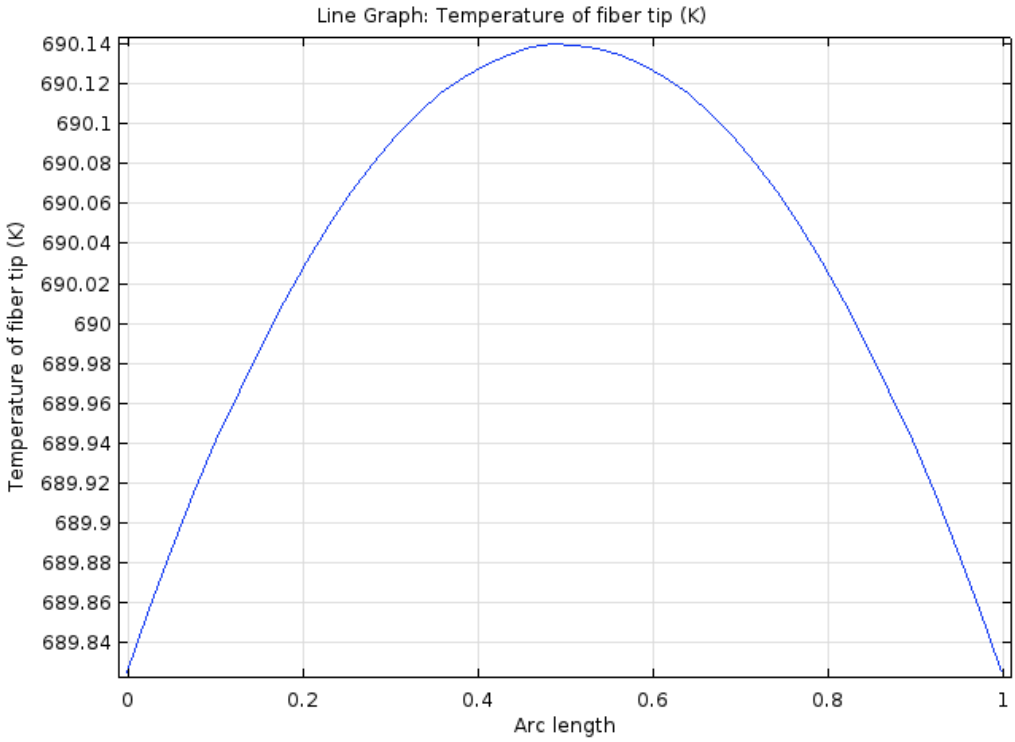

Figure 6.21: Optical fiber and receiver interface concept 3 - the temperature of the fiber tip (end)

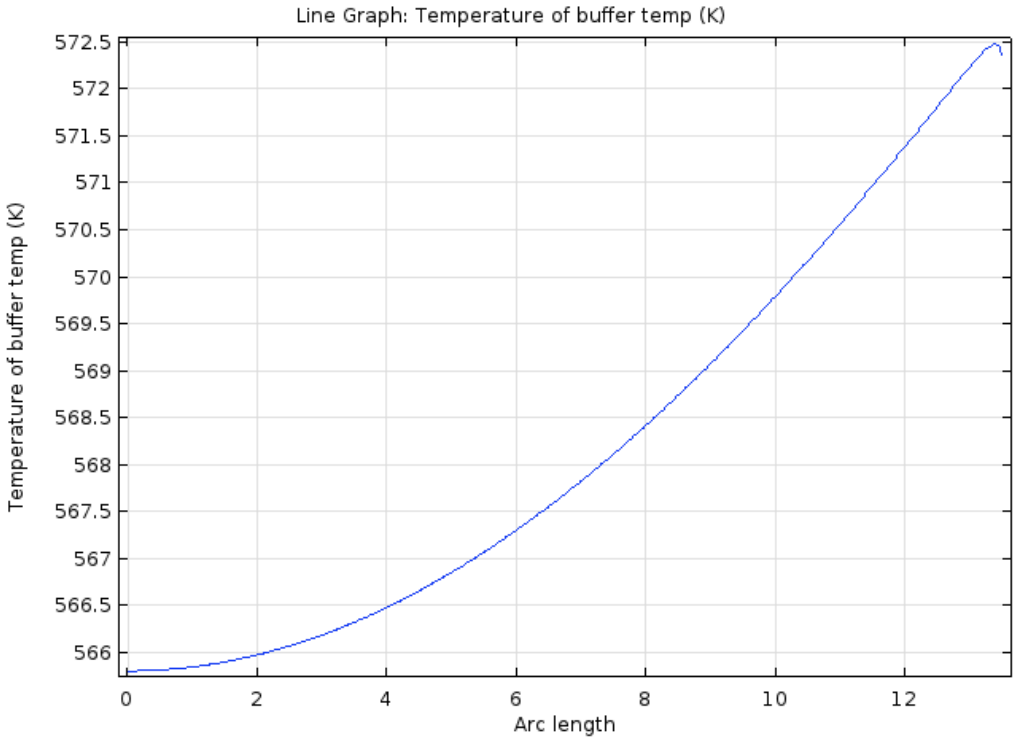

Figure 6.22: Optical fiber and receiver interface concept 3 - temperature of the buffer surface

From all the above results in this section it can be concluded that concept 3 looks the most promising coupling interface with the ability to bring down the tip temperature to 690.14 K and buffer layer temperature to 572.5 K. Further, the length of the quartz collet can be increased to achieve lower buffer temperature as desired and that would add more mass to the system.

Table 6.3: Optical fiber - receiver coupling concepts comparison table

Fiber - Receiver Coupling Concept	Concept 1 (Baseline Design)	Concept 2	Concept 3
Optical Fiber Tip Temperature [K]	1089.7	1062.5	690.14
Buffer Temperature (Max.) [K]	1089.7	758.5	572.5
Mass [g]	0	1.2	0.5642

6.3. Verification of the Analytical model

The table 6.4 presents the temperature data generated from the Matlab analytical model and the Comsol numerical model. The difference between the models are mainly due to transient heat transfer considered in the Matlab model and steady-state assumption for the numerical analysis in Comsol.

Table 6.4: Verification of the thermal model

Parameter	Matlab Model	Comsol Model	Difference
Cavity Wall Temperature (Insulation- without flow) [K]	1249	1240	3.9%
Cavity Wall Temperature (Insulation- with flow) [K]	1112	1200	7.9%
Propellant Outlet Temperature [K]	1000	1000	0%
Channel Wall Mean Final Temperature [K]	1260.9	1240	4.8%

In order to verify the analytical thermal model of the heat exchanger and conjugate heat transfer with the numerical time-dependent simulations in Comsol, one of the preliminary study cases is presented in Appendix D. From the test case, it is inferred that the models indicate a difference of 1.28 %.

6.4. Thrust Performance

The thruster efficiency η_{thrust} is defined as the ratio of the jet power to the input power transferred to the propellant and is mathematically expressed in equation 6.4. The wall and cavity temperature reaches to about 1240 K as determined from the numerical thermal model and being the lower value between the two models, it has been considered to generate conservative results. Therefore, the performance parameters of the thruster are determined at a chamber temperature 1240 K and chamber pressure of 5 bar. The thrust, mass flow rate, and exit velocity are calculated including the

losses due to the flow at the nozzle.

$$\eta_{thruster} = \frac{P_J}{P_{prop\ in}} = \frac{0.5 F_{vis} U_e}{P_{prop\ in}} \tag{6.4}$$

Here the power input is the power needed to heat up the propellant to the desired temperature which can be expressed as the product of the mass flow rate due to viscous losses and the change in enthalpy. The $\dot{m}_{viscous\ loss}$ is 2.3150e-04 Kg/s, exit velocity is 2.1236e+03 m/s and change in enthalpy is calculated between enthalpy at 1000 K and 298.15 K. The number of channels has been selected through an iterative process. A value is assumed for the number of channels for a constant channel height, mass flow rate and aspect ratio and is repeated until the desired temperature is reached.

Table 6.5: Thrust performance

H_{ch} **[mm]**	W_{ch} **[mm]**	L_{ch} **[mm]**	**No. of channels [-]**	$\frac{A_e}{A_t}$	**No. of Optical fibers [-]**	**Power (each) [W]**	**Prop Temp [K]**	I_{sp} **[s]**	**Thrust [mN]**	η_{thrust} **[%]**
0.709	0.142	40.23	10	25	8	7.67	1000	216.47	0.4227	50.02

6.5. Final Design Render

The figure 6.23 below shows the entire design render with insulation of 1.2 cm thickness of pyrogel. Given the channel width of 0.142 mm and minimum wall thickness of 0.45 mm, the total cavity width is 6.37 mm. The minimum cavity width must be more than 3 times that of the nozzle width 2.1267 mm and hence, this criteria is fulfilled . From the heat flux density figure 6.3 it can be observed that for a cavity height of 4.5 mm 6.3(d) (and cavity width) the flux is more evenly distributed compared to a larger height which has spots of lower density deposited at the center of the wall surface. The optical fibers can be seen in blue with the collect tube for the optical fiber and receiver coupling in maroon. The surrounding off-white block around the thruster and heat exchanger is the insulation.

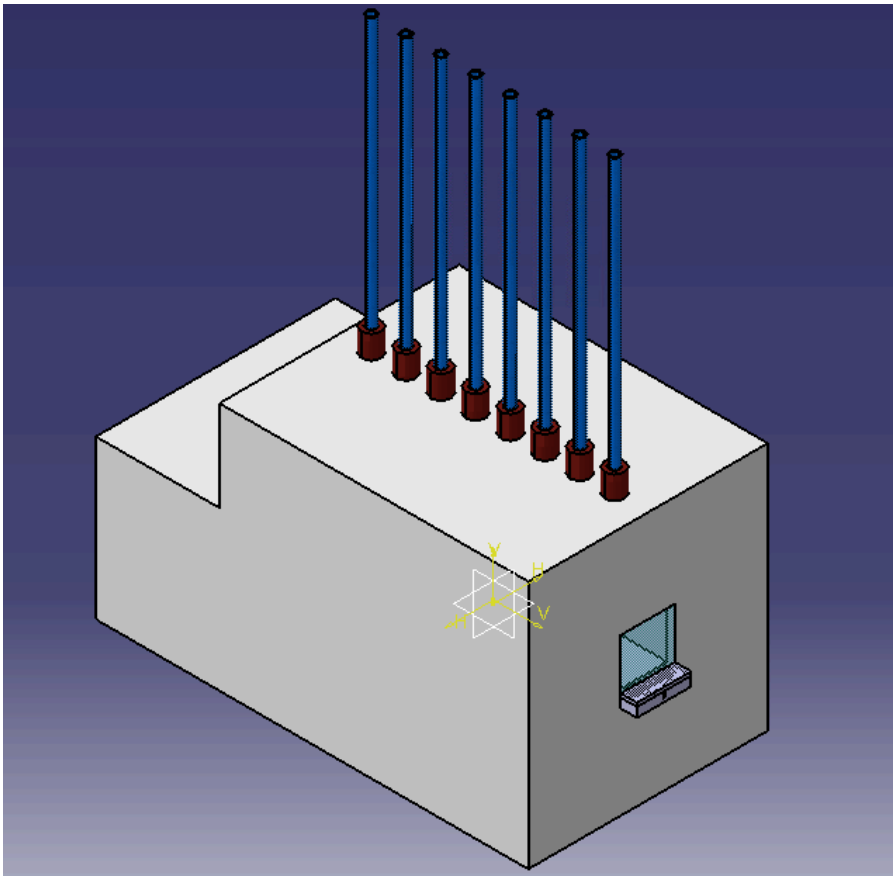

Figure 6.23: Final design render with insulation isometric view

The figure 6.24 depicts the optical fiber and receiver interface. The lens radius is the same as the collect radius at 1.35 mm. The lenslet (in yellow) dimension has not been studied in depth and further analysis is required to optimize the coupling interface.

The figure 6.25 illustrates the inlet manifold. The uniformly stepped manifold has been integrated in order to obtain uniform flow distribution through the microchannels. This preliminary design leads to a varying flow rate branching into the reduced area of the manifold segment which in turn ensures that identical flow distribution is achieved in each channel [70]. A detailed trade-off of varying the inlet position of the manifold and step dimension can be carried out for future work.

The figure 6.26 shows the top view of the design. The green and surrounding blue section is the core having a diameter 1 mm and jacket having a diameter of the 1.4 mm of the optical fiber respectively. The nozzle section has a divergent angle of 20.42 degrees and a convergent angle of 15 degrees with a nozzle width of 0.7089 mm. The depth of the entire nozzle section is constant at 0.7089 mm.

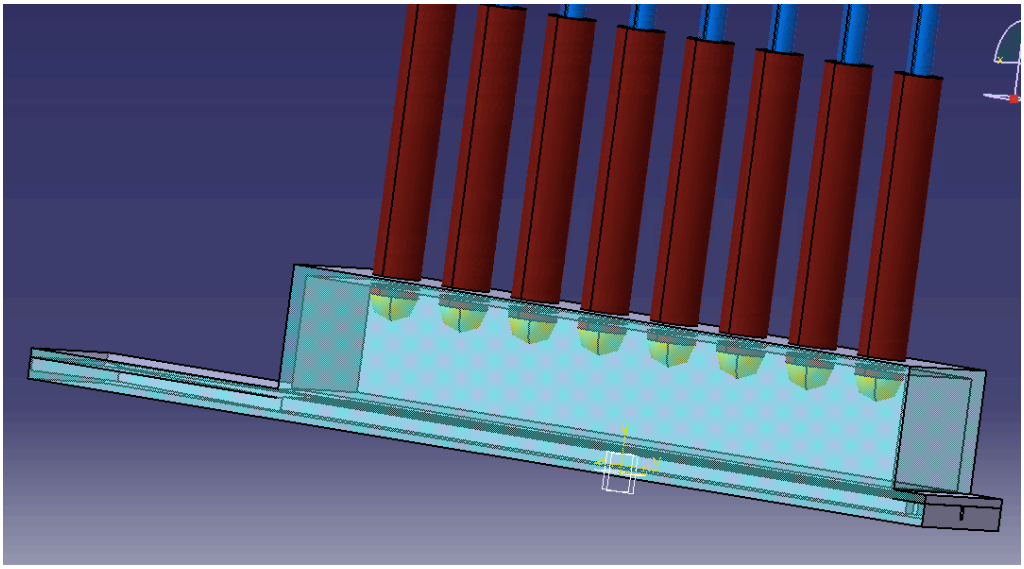

Figure 6.24: Final design render without insulation isometric view

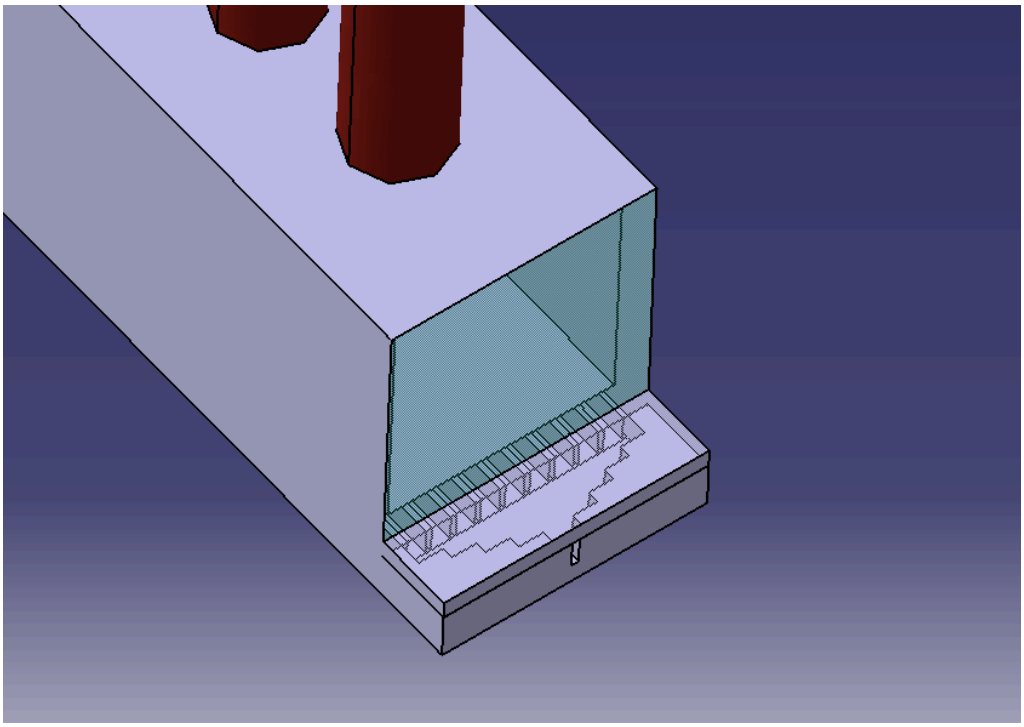

Figure 6.25: Final design render - inlet manifold

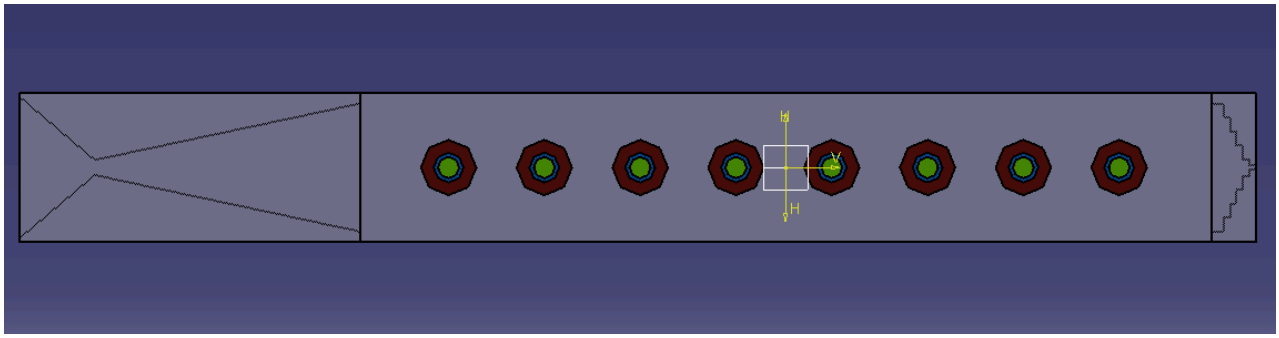

Figure 6.26: Final design render top view

Several geometries for propellant tanks have been used and studied over the past years for various propulsion systems and satellites. The most optimal propellant tank shape is spherical as it been researched to offer lowest structural mass for a given volume and smallest wall thickness [71]. But since we are dealing with cubical units of CubeSats, the most sensible geometry of the tanks is a cuboid or rectangle for integration with the CubeSat frame. Although, the practical comparisons between a rectangular tank and a cylindrical tank show that the former can withstand considerably lower pressures for the same wall thickness and is, therefore, less efficient [72]. But considering the geometrical constraints for the interface of the tank and the CubeSat, a rectangular tank seems to be the best available option. The available volume for the propellant tank has been approximated to be 2U of CubeSat volume which consists of propellant mass of 1.84 Kg + 10% margin. The margin is applicable considering the ”existing technology with minor modifications” margin philosophy for sub-systems [61]. The available volume for the remaining components of the propulsion system after deducting the propellant tank volume (2U of CubeSat volume) is 2U which is about 2000 cm^3. The entire thruster - exchanger system (minus the optical fibers) can fit within a volume envelope of 7.3 cm x 3 cm x 3 cm - (58.5 cm^3), the dimensions being the length, height and width of the system with insulation respectively.

To provide a conclusive STP system mass and volume occupied in the 12U CubeSat, the figures 6.27 and 6.28 depict a pie chart respectively. The mass budget illustrate in the figure has been generated based on table 4.10. The volume of the heat exchanger, thruster and insulation have been determined based on the final design. For optical fibers, while there can be several stacking configurations, the volume is computed such that the fibers fit within 1U side length, i.e the bend radius would be 5 cm. In case of coiled stacking of 1 m long fibers with 8 loops, the volume occupied by each fiber is 3.173 cm^3. The packaging ratio of the inflatable concentrator has not been computed in this thesis and therefore a linear estimation of packaging volume is done based on literature [20]. Remaining sub-systems that include the inflation system, concentrator deployment system, ADCS propulsion system, pumps, and valves are unknown and are shown to have an available volume of 500 cm^3 after deducting 20% margin from the total volume.

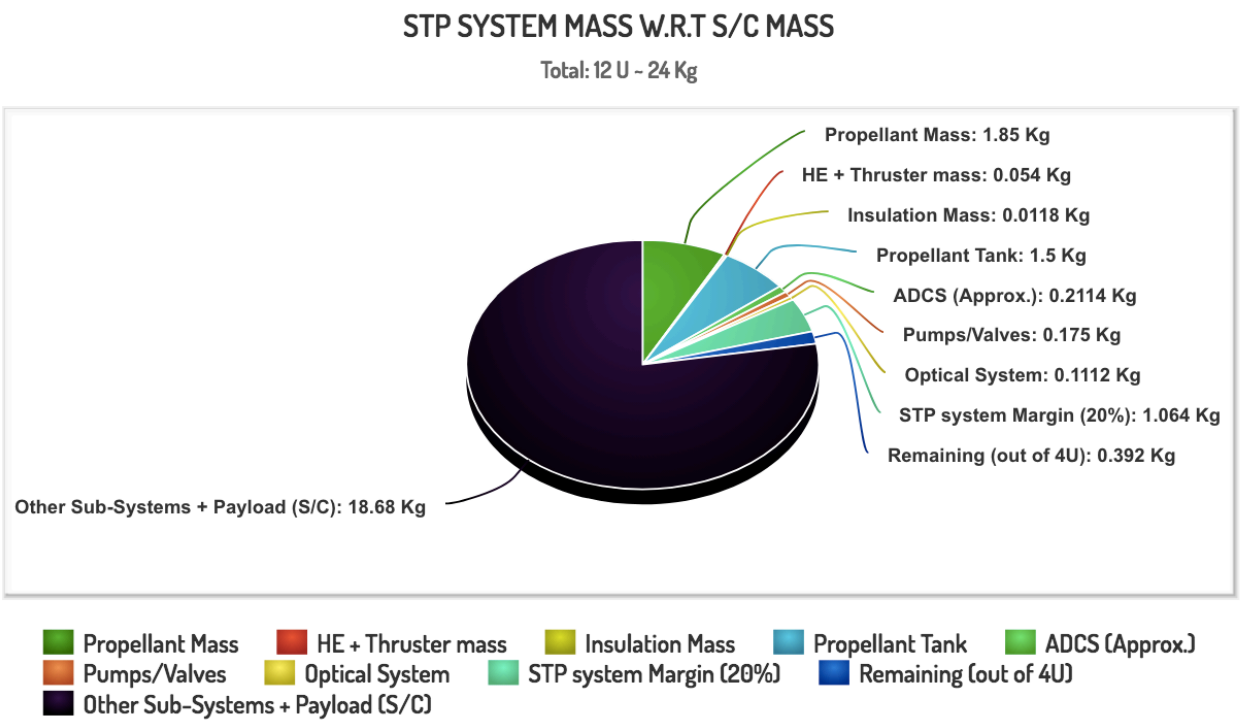

Figure 6.27: STP System Mass w.r.t S/C Mass

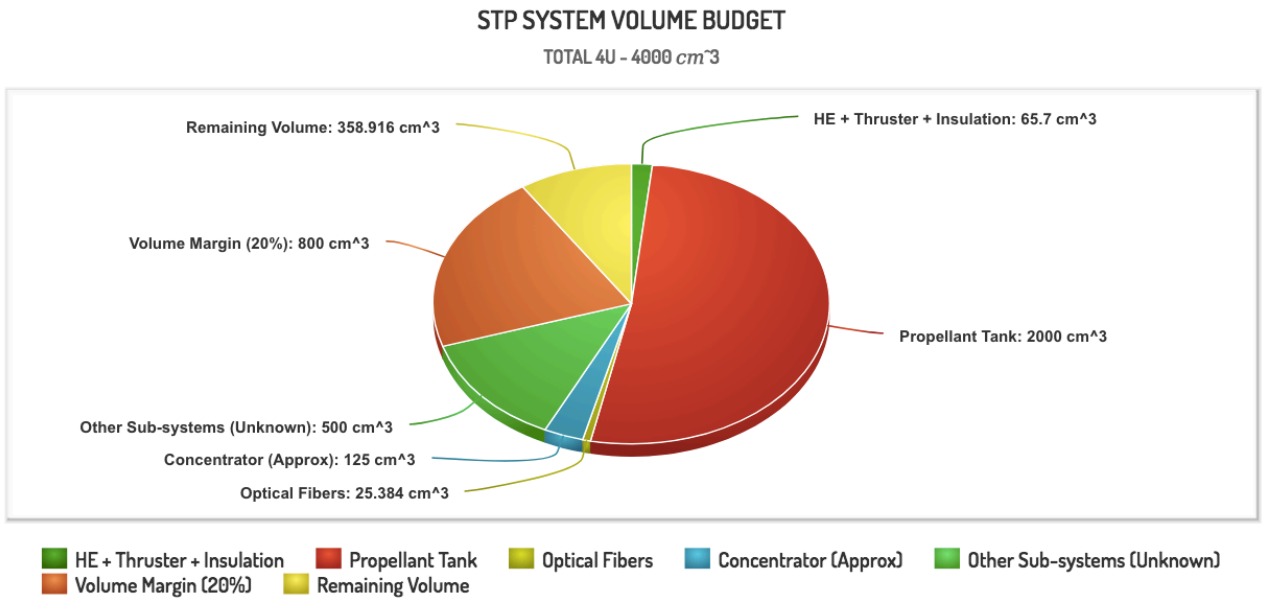

Figure 6.28: STP System Volume Budget

6.6. System Requirements Verification

Verification is defined as the proof of compliance with design solution specifications and descriptive documents. It is accomplished at each level of the system architectural hierarchy. Verification is performed to ensure the product complies with requirements and may be determined by test,

analysis, demonstration, inspection or a combination of these [73].

Table 6.6: System requirement verification

ID	Requirement	Lunar mission	Verification with Analysis (complete) and Rationale	Verification required
RE-STP-01	Operating pressure	System operating pressure shall be below 5 bar	The pressure reaches 4.9 bar during analysis.	Testing
RE-STP-02	Propulsion sub-system Volume	The subsystem shall not exceed 4U of CubeSat volume	System integration figures 6.27 6.28	Demonstration
RE-STP-03	Propellant mass	The propellant mass shall not exceed 15 % of the satellite mass	The propellant mass is 1.85 Kg which is at 7.7% of the satellite mass.	Design review, Testing
RE-STP-04	Thrust Range	The system shall have a thrust range of 0.4 mN to 1N	The thruster offers a thrust of 0.4227 N	Demonstration, Testing
RE-STP-05	ΔV	The system shall generate a total budget of 160 m/s	The delta V requirement is maintained during analysis.	-
RE-STP-06	Propellant temperature	The propellant temperature shall be limited to 1000 K	The propellant temperature reaches upto 1000 K with 4.023 cm channel length.	Testing
RE-STP-07	Wet mass	The wet system mass shall take up a maximum of 40 % of the total S/C mass budget [50]	The propulsion system takes less than 23.12% of the total S/C mass (24 Kg)	Design review, Testing
RE-STP-08	Total Impulse	The min total impulse shall be 3.908 KNs	The total impulse is estimated to be 3.659 KNs	-

Table 6.6: System requirement verification

ID	Requirement	Lunar mission	Verification with Analysis (complete) and Rationale	Verification required
RE-STP-09	Power Required (Electrical)	The power consumption shall not be greater than 15 W	The thruster itself does not consume any electrical power. (optical system + heat exchanger)	Testing
RE-STP-10	Mission Duration	The system shall provide at least 1 year of mission	-	Design review, Analysis

7

Conclusions and Recommendations

Conclusions

This thesis presents a design of the solar thermal thruster and deals with the investigation of its performance for flight on board a 12U CubeSat. The chapters in this thesis aim at answering the formulated research question: ***How can a MEMS solar thermal thruster be designed such that it fits within a 1U CubeSat volume and offers proper integration for a concentrator/STP system aboard a 12U CubeSat?*** After a brief introduction and literature study reported in chapter 2, the thesis continues with establishing a final design of the thruster following an iterative process between the thruster model and the thermal model of the system.

Chapter 3 answers research question ***1. Can the STP thruster for the selected mission be integrated with the system based on MEMS?*** To answer the first question, the selection of sub-components of the STP and materials adhering to the temperature requirement focuses on feasible geometries that can be produced using micro-fabrication technologies and or meso-scale manufacturing methods such that it can offer achievable integration with a system based on MEMS. The final design STP thruster presents challenges in the field of manufacturing and coupling of the optical fiber with the receiver cavity. Both these issues need to be addressed in detail for future work.

Chapter 4 answers research question ***2. What are the performance parameters, geometrical and material characteristics of the proposed design?*** Considering a power input efficiency of 73% from the concentrator to the output end of the optical fiber, the required power is 55.25 W to ensure heating of the propellant flowing through the heat exchanger. The sub-questions are further discussed in chapter 5 where the heat loss associated with the selected closed rectangular cavity and the parametric study of the channel dimensions with respect to temperature is investigated. A total channel length of 4.023 cm has been achieved to heat up the propellant to 1000 K. Some general observations of the parametric study are as follows,

- For a constant aspect ratio, channel length, and no.of channels, the final flow temperature reduces as the channel height is increased. This is attributed to the higher Reynolds number for smaller channel height which characterizes a turbulence flow which in turn implies greater heat transfer efficiency.
- For a constant channel height, channel length, and no. of channels, the propellant takes longer to vaporize with decreasing order of aspect ratio (aspect ratio is defined as $H_{channel}/W_{channel}$

in this context). This observation can be explained by considering insufficient heating or comparatively lower heating of the fluid particles at the top layer as the mass flow rate remains independent of the aspect ratio and is equally distributed through the channels.

Chapter 4 also addresses ***3. What are the challenges and design constraints with developing a MEMS solar thermal thruster especially at the thruster nozzle?*** The ideal and real thruster performance have been studied taking into account all known losses at the nozzle throat. A parametric study of the nozzle throat dimension has been conducted to observe the change in performance and losses associated, keeping the nozzle throat area constant. The heat exchanger channel height is constrained w.r.t to the nozzle depth to ensure same depth throughout the thruster. An optimum depth of the nozzle throat has been selected after an iteration between the nozzle performance and analyzing the efficient heat transfer via convection in the channels and its flow properties.

Some sections in chapter 2, chapter 5 and chapter 6 answers research question ***4. What is the most efficient method of heat transfer to the propellant?*** Indirect heating of the propellant using corrugated and plain closed cavity surface has been studied and no significant difference was observed. Hence, to reduce manufacturing complexity, a plain surface rectangular cavity was deemed feasible.

- In the thermal model, it can been noted that the temperature of the entire heat exchanger is more or less homogeneous except at the propellant channel inlet. Which means that the cavity geometry doesn't affect the heat transfer except the fact that increase in mass would lead to more stored energy and slower discharge of energy once the power source is shut.
- High temperatures of the optical fiber tip are observed when it comes in contact with the cavity and thus attention is given to receiver-cavity coupling concept.
- The results of the analytical model and the numerical model in Comsol do not completely match due to insufficient mesh quality used for the analysis for the ray heating model. This resulted in a diverging-converging convergence plot which characterizes the problem. However, the results of the Matlab model and conjugate heat transfer model show a difference of 4.8%. The numerical model shows proper convergence and, therefore, in this case, the difference is attributed to the steady state heat transfer model used for the latter. But an example present in the appendix, verifies the Matlab model with the Comsol time-dependent model.

The thruster offers lower total impulse than requirement specified (**RE-STP-08**) which has varied since the initial analysis conducted during the literature study which was based on 20% more propellant mass required for the mission. The final design has been shown to have dimensions that will fit within 1 U of CubeSat volume as well as adhere to the mass budget available as concluded in chapter 6. The STP system offers a chamber temperature of about 1240 K that is capable of heating the propellant to a temperature of 1000 K. The thruster system incorporates optical fibers for the transmission of heat energy to reach the cavity of the heat exchanger. The heat exchanger requires an insulation of 1.2 cm thickness on either side to maintain low surrounding temperature. The final design of the solar thermal thruster offers a thruster efficiency of 50.02%. It can thus be concluded that an STP thruster for a lunar mission is beneficial over existing propulsion systems given it complies to the system requirements that have been formulated to offer competitive performance levels.

Recommendation

1. An additional support structure for the optical fiber needs to be designed such that it is structurally strong and lightweight if the quartz collet at the fiber-receiver coupling interface proves to be insufficient to provide the required structural integrity.
2. Support structure for holding the bundle at the focal point of the concentrator has to be designed and analyzed.
3. Verification of the design by testing post re-evaluation of the design and analysis done in this thesis.
4. For the given geometry, the manufacturing of the cavity and the heat exchanger channel and the nozzle can be split into two using MEMS manufacturing technique for etching the channels and nozzle shape and meso-scale manufacturing techniques for the cavity. The two parts can then be bonded based on available bonding methods. Alongside, other channel geometries can be studied.
5. The pumping power required for the propellant feed system must be determined along with the manifold design for the propellant inlet section.
6. Extensive thermal analyses through simulations must be performed with improved meshing quality.
7. Detailed designing and structural analysis of the concentrator, inflation system and deployment mechanism need to be carried out.

Appendices

A

Optical Fiber Specifications Sheet

The plot shown in figure A.1 is the attenuation graph for an optical fiber with a core diameter of 1 mm and is characterized by a numerical aperture of 0.5 over the wavelength range of 200 t0 2000 nm.

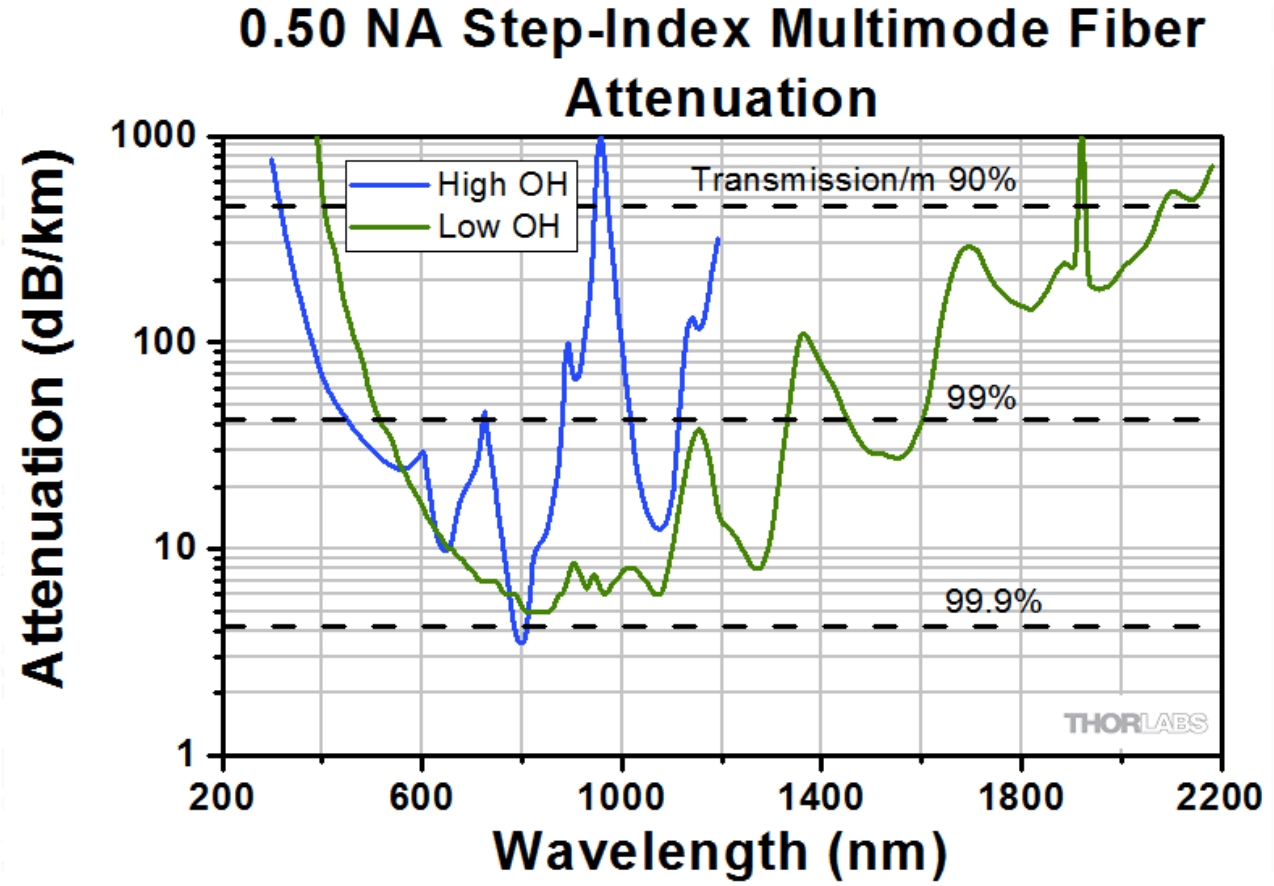

Figure A.1: Attenuation graph of 0.50 NA Hard Polymer Clad Multimode Fiber [4]

THORLABS

0.50 NA Hard Polymer Clad Multimode Fiber

Description

FP1000ERT

Thorlabs' 0.50 NA hard polymer-clad, multimode, step-index fibers offer high numerical apertures to suit a broad range of applications, from remote illumination to photodynamic therapy. This high quality fiber offers easy termination with no pistoning effect and is a cost effective alternative to silica / silica fiber.

Specifications

FP1000ERT	
Transmission Region	400 - 2200 nm (Low OH Content)
Core Diameter	1000 ± 15 µm
Cladding Diameter	1035 ± 15 µm
Coating Diameter	1400 ± 50 µm
Core / Cladding Material	Pure Silica / Hard Polymer
Operating Temperature (Tefzel Coating)	-40 to 150 °C
Numerical Aperture (NA)	0.50
Attenuation	12 dB/km @ 810 nm (Max)
Proof Test Level	≥100 kpsi
Max Core Offset	10 µm
Bend Radius	40 mm (Short Term) 80 mm (Long Term)
Recommended Stripping Tool	M44S63

Performance Plot

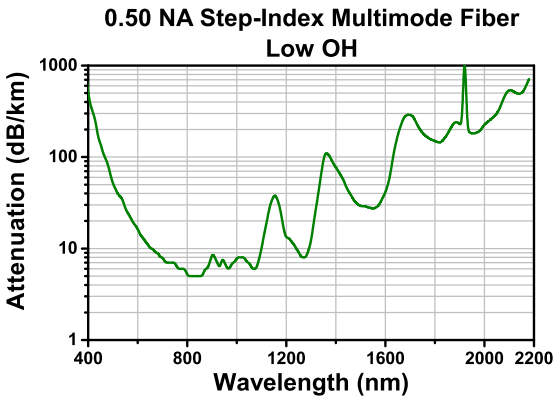

Figure A.2: Data sheet of 0.50 NA Hard Polymer Clad Multimode Fiber [4]

B

Advanced Ceramics Property Sheet

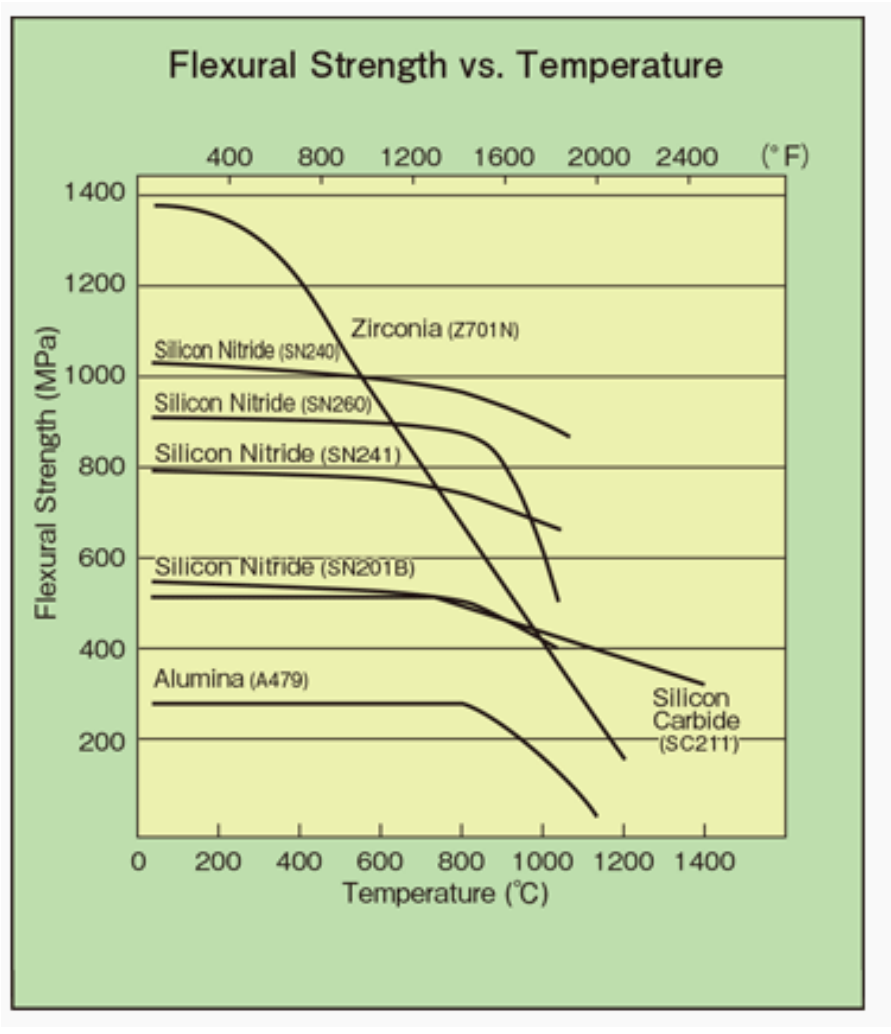

Figure B.1: Flexural strength vs. Temperatue of advanced ceramics [7]

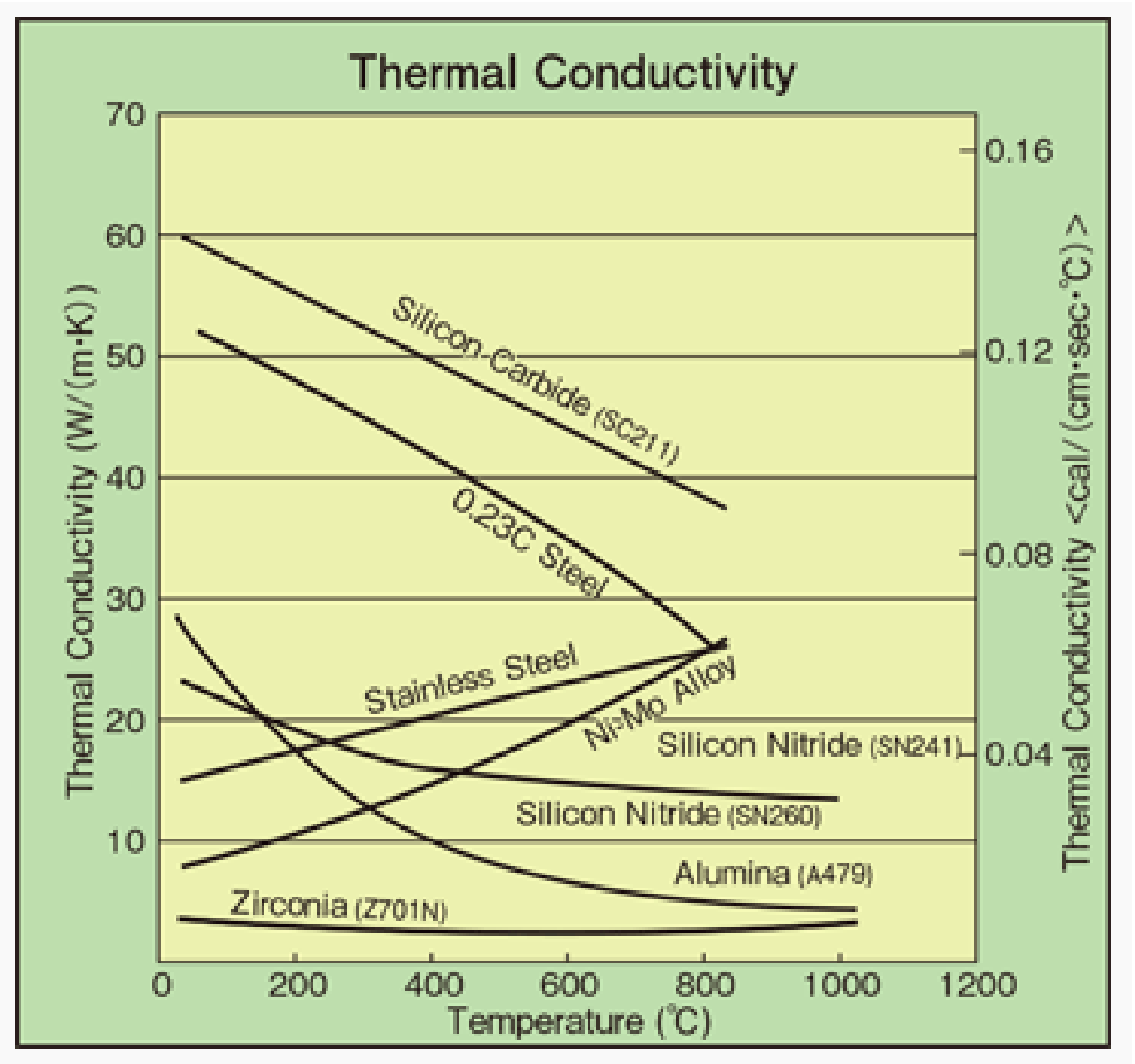

Figure B.2: Thermal conductivity of advanced ceramics [7]

C

Nusselt Number of Three Side Heated Walls

As discussed in sub-section 4.3.1, the figure C.1 depicts the local Nusselt number over the channel length for a 3D rectangular microchannel with 3 sides heated walls with water flow.

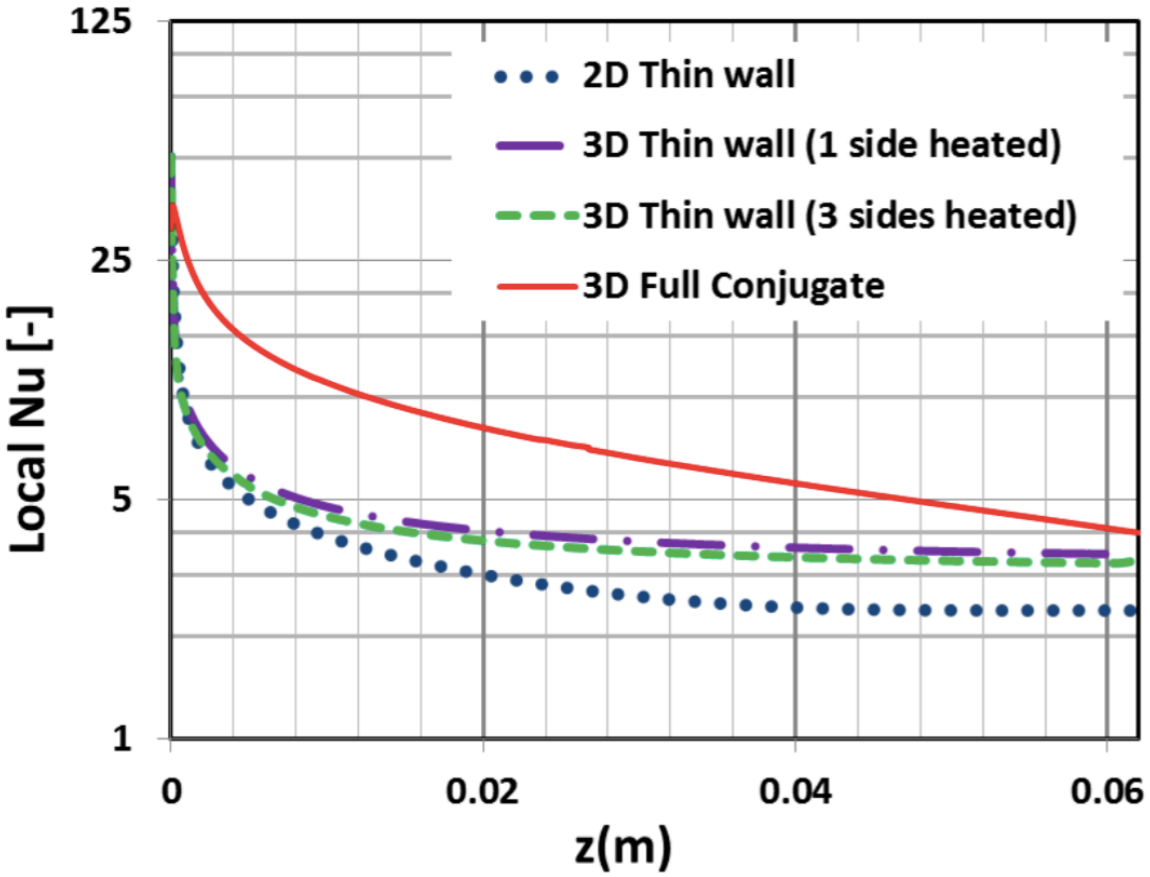

Figure C.1: Variation of Nusselt number along the channel length [8]

D

Verification of Analytical and Comsol Model

The following test case was modelled in Comsol and in Matlab to compare the results

Channel height [mm]	Channel width [mm]	Channel Length [mm]	No. of channels [-]	No. of Optical fibers [-]	Power (each) [W]
0.4	0.4	30	9	8	7.671

Table D.1: Dimension for test case

The plot D.1 shows the maximum cavity wall temperature with needed insulation of 1.2 cm, followed by reducing the insulation thickness. The insulation thickness used for the analysis is 0.07 cm. A cavity temperature of 710.7 K was computed from the Matlab model. The next plot **??** is the generated wall temperature in comsol for the same geometrical parameters for a time-dependent model. At the final time of 1000 s the wall temperature is seen to gradually increase over the length of 30 mm. The final temperature attained at the end of channel length is 719.8 K with 0.07 cm insulation. Comparing both the models, a difference of 1.28% is observed for the final channel wall temperature. The computational time being 81216 s, the conjugate heat transfer numerical model for remaining cases in Comsol was modelled for steady state instead of time-dependent once the diffusive surface properties of the materials used were included.

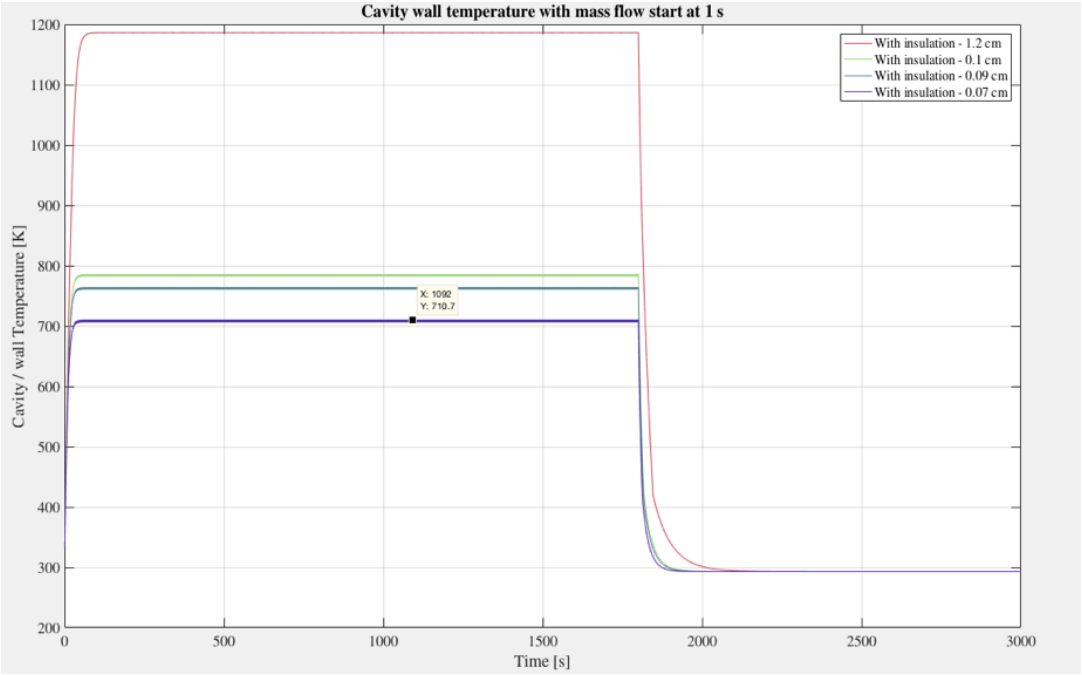

Figure D.1: Channel wall temperature with 0.07 cm thickness of insulation from Matlab model

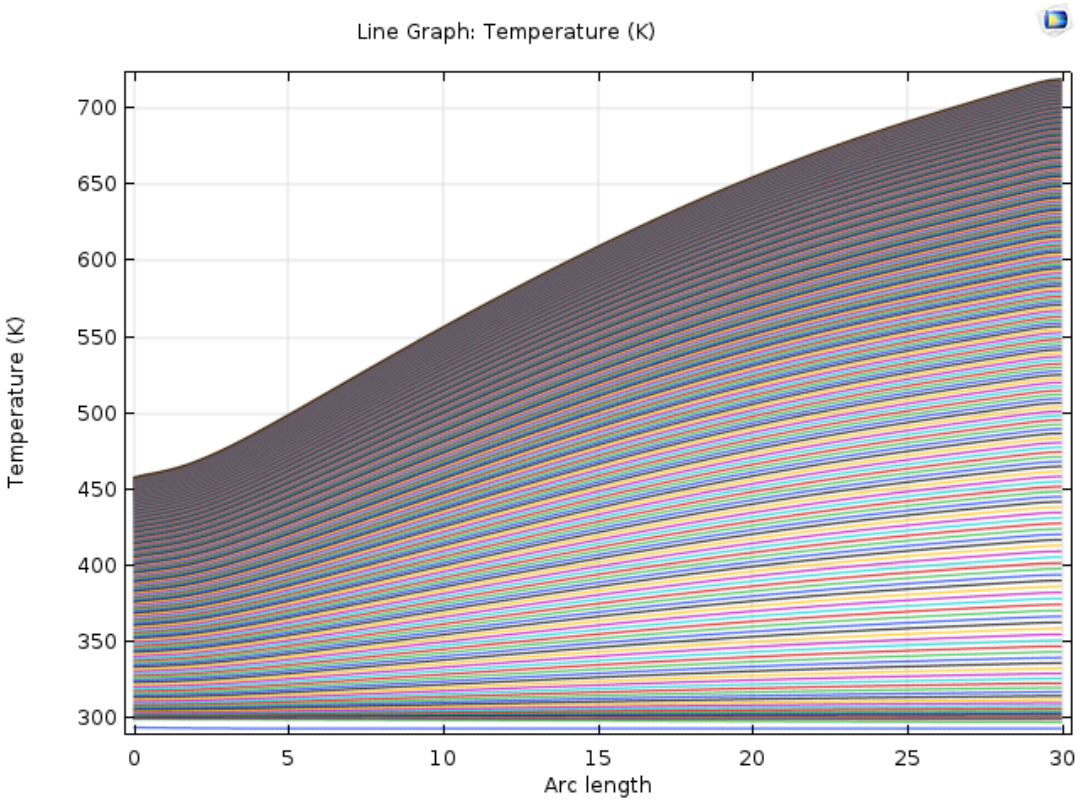

Figure D.2: Channel wall temperature with 0.07 cm insulation from comsol model

Bibliography

[1] B. Y. I. Waki, T. T. Otani, and H. N. Agata, *thermal design of a solar thermal thruster for piggyback satellites*, , 71.

[2] P. R. Henshall, *Solar Thermal Propulsion Augmented with Fiber Optics: - A System Design Proposal*, , 1 (2005).

[3] C. K. Ho, J. M. Christian, J. D. Ortega, J. Yellowhair, M. J. Mosquera, C. K. Ho, J. M. Christian, J. D. Ortega, J. Yellowhair, M. J. Mosquera, C. E. Andraka, and C. E. Andraka, *solar thermal receivers*, **917506** (2018), 10.1117/12.2063152.

[4] Thorlabs, *0 . 50 NA Hard Polymer Clad Multimode Fiber*, , 6647 (2015).

[5] J. K. H. Lin, F. Houfei, E. Im, and U. O. Quijano, *Concept study of a 35-m spherical reflector system for NEXRAD in space application*, 47th AIAA/ASME/ASCE/AHS/ASC Structures, Structural Dynamics and Materials Conference **1**, 62 (2006).

[6] C. Altman, *Microlens array fabrication via microjet printing technologies*, Proc. Workshop Opt. Fabrication Technol , 2 (2007).

[7] K. Global, *Advanced Ceramics Properties*, https://global.kyocera.com/prdct/fc/list/material/zirconia/zirconia.html (2018), [Online; accessed 02-September-2018].

[8] A. M. Sahar, M. R. Ozdemir, M. M. Mahmoud, J. Wissink, and G. Tassos, *Single Phase Flow Pressure Drop and Heat Transfer in a Rectangular Metallic Micro channel*, , 7 (2014).

[9] A. N. Johnson, P. I. Espina, G. E. Mattingly, and C. L. Merklet, *Numerical Characterization of the Discharge Coefficient in Critical Nozzles*, Proceedings of the 1998 NCSL Workshop and Symposium , 407 (1998).

[10] P. Sundaramoorthy, *Micro-satellite engineering course notes (ae4-s10)*, (Space Systems Engineering (SSE), Delft University of Technology, 2017).

[11] A. Cervone, B. Zandbergen, D. C. Guerrieri, M. A. Costa, I. Krusharev, and H. Zeijl, *Green micro-resistojet research at Delft University of Technology: new options for Cubesat propulsion*, CEAS Space Journal (2016), 10.1007/s12567-016-0135-3.

[12] H. C. M. Leenders and B. T. C. Zandbergen, *DEVELOPMENT OF A SOLAR THERMAL THRUSTER SYSTEM*, , 1 (2008).

[13] F. G. Kennedy and P. L. Palmer, *Aiaa 2002-3928*, , 1 (2002).

[14] A. Hutputanasin, A. Toorian, W. Lan, and R. Munakata, *CubeSat Design Specification Rev. 12* (California Polytechnic, State, 2009) pp. 1–21.

[15] W. S. o. M. Engineering, Manufacturing, and Loughborough University, eds., *An Introduction to MEMS* , January (PRIME Faraday Partnership, 2002).

[16] H. P. G. Jr, *Solar Thermal Propulsion at MSFC*, (2016).

[17] F. G. Kennedy, *Solar Thermal Propulsion for Microsatellite Manoeuvring,* (2004).

[18] F. Etheridge, *Responsible Engineer,* (1979).

[19] M. Shimizu, K. Itoh, and H. Sato, *Single crystal mo solar thermal thruster for microsatellites,* International Astronautical Federation Published by Elsevier Science Ltd **44** (1999).

[20] D. M. Pino, *Solar Concentrator Demonstrator for PocketQubes*, Ph.D. thesis, DelftUniversity of Technology (2016).

[21] K. Das, *Literature Study of MEMS Design of a Solar Thermal Thruster,* .

[22] A. Cervone, *Lumio mission - System Design*, Tech. Rep.

[23] J. J. Preijde, *Design of a Solar Thermal Power-Propulsion System for a Small Satellite,* (2015).

[24] M. M. Micci and A. D. Ketsdever, eds., *Micropropulsion for small spacecraft*, June (American Institute of Aeronautics and Astronautics, Inc., 2000).

[25] M. F. Kennedy and U. S. A. Force, *An Analysis of Preliminary Test Campaign Results for a Microscale Solar Thermal Engine,* , 1.

[26] B. Zandbergen, *AE4S01 Thermal Rocket Propulsion* (CRC Press, 2017).

[27] W. Louisos, A. Alexeenko, D. Hitt, and A. Zilic, *Design considerations for supersonic micronozzles,* International Journal of Manufacturing Research **3**, 80 (2008).

[28] X. I. N. G. Baoyu, L. I. U. Kun, H. U. A. N. G. Minchao, and C. H. E. N. G. Mousen, *High Efficient Configuration Design and Simulation of Platelet Heat Exchanger in Solar Thermal Thruster,* **23**, 246 (2014).

[29] Y. F. Hou and W. Q. Liu, *Thermal and Stability Analysis of Formed Platelet in Platelet Transpiration Cooling,* in *Advances in Mechanical Engineering*, Applied Mechanics and Materials, Vol. 52 (Trans Tech Publications, 2011) pp. 859–864.

[30] Y. F. Hou and W. Q. Liu, *Analysis of Formed Platelet Thermal Wrinkling in Platelet Transpiration Cooling,* in *Advances in Mechanical Design*, Advanced Materials Research, Vol. 199 (Trans Tech Publications, 2011) pp. 1590–1594.

[31] M. Akbari, D. Sinton, and M. Bahrami, *Pressure Drop in Rectangular Microchannels as Compared With Theory Based on Arbitrary Cross Section,* Journal of Fluids Engineering **131**, 041202 (2009).

[32] T. Mathew, B. Zandbergen, G. Brouwer, and A. Migliaccio, *Design of a MEMS micro-resistojet*, Ph.D. thesis, Technical university of Delft (2011).

[33] G. Karniadakis, *Microflows and Nanoflows Fundamentals and Simulation,* Springer-Verlag New York **volume 29 of0939-6047** (2005).

[34] D. Cordeiro Guerrieri, *The low-pressure micro-resistojet: Modelling and optimization for future nano- and pico-satellites*, Ph.D. thesis, TU Delft University (2018).

[35] F. L. Torre, *Gas Flow in Miniaturized Nozzles for Micro-Thrusters*, Ph.D. thesis.

[36] S. George P., *Rocket Propulsion Elements (9th Edition),* in *Rocket Propulsion Elements (9th Edition)* (John Wiley Sons, 2017) Chap. 3.

[37] I. Sotome, Y. Ogasawara, Y. Nadachi, M. Takenaka, H. Okadome, and S. Isobe, *Measurement of steam/water ratio in the nozzle jet of an oven system using superheated steam and hot water spray,* Japan Journal of Food Engineering **10**, 163 (2009).

[38] AZoM, *Molybdenum - Mechanical Properties And Material Application,* (2012).

[39] F. N. Blanket and G. Characteristics, *Fibermax Needled Blankets,* .

[40] *Thesis Committee: Professor Xiaodong Sun, Advisor Professor Richard Christensen,* (2011).

[41] R. H. French, J. M. Rodriguez-Parada, M. K. Yang, R. A. Derryberry, M. F. Lemon, M. J. Brown, C. R. Haeger, S. L. Samuels, E. C. Romano, and R. E. Richardson, *Optical properties of materials for concentrator photovoltaic systems,* 2009 34th IEEE Photovoltaic Specialists Conference (PVSC) , 000394 (2009).

[42] T. Q. Corporation, *Typical properties of clear fused silica,* http://www.thequartzcorp.com/en/applications/quartz-glass/quartz-glass-properties.html (2018), [Online; accessed 1-January-2018].

[43] G. Scannell, *Understanding the structure and deformation of titanium-containing silicate glasses from their elastic responses to external stimuli To cite this version : HAL Id : tel-01386572 Garth Scannell Understanding the structure and deformation,* (2016).

[44] J. Jiang, Y. Hao, and M. Shi, *Fluid Flow and Heat Transfer Characteristics in Rectangular Microchannels,* **37**, 197 (2008).

[45] G. L. Morini and I. Università, *Laminar-to-turbulent flow transition in microchannels,* (2013), 10.1080/10893950490272902.

[46] P.-S. Lee, S. V. Garimella, and S. V. Garimella, *Thermally Developing Flow and Heat Transfer in Rectangular Microchannels of Different Aspect Ratios Thermally Developing Flow and Heat Transfer in Rectangular Microchannels of Different Aspect Ratios,* (2006), 10.1016/j.ijheatmasstransfer.2006.02.011.

[47] R. W. Knight, J. S. Goodling, D. J. Hall, and R. C. Jaeger, *Heat Sink Optimization with Application to Microchannels,* IEEE Transactions on Components, Hybrids, and Manufacturing Technology **15**, 832 (1992).

[48] S. G. Singh, A. Kulkarni, S. P. Duttagupta, B. P. Puranik, and A. Agrawal, *Impact of aspect ratio on flow boiling of water in rectangular microchannels,* Experimental Thermal and Fluid Science **33**, 153 (2008).

[49] W. Qu and I. Mudawar, *Flow boiling heat transfer in two-phase micro-channel heat sinks-I. Experimental investigation and assessment of correlation methods,* International Journal of Heat and Mass Transfer **46**, 2755 (2003).

[50] ASME, *sme Boiler and Pressure Vessel Code, Mandatory Appendices,* Asme Boiler and Pressure Vessel Code (2004).

[51] H. Leenders, *Development of a solar thermal propulsion system, MSc Thesis, TU Delft, Aerospace engineering,* (2008).

[52] A. Kribus, O. R. Y. Zik, and J. Karni, *OPTICAL FIBERS AND SOLAR POWER GENERATION,* **68**, 405 (2000).

[53] T. Nakamura, D. Sullivan, J. A. Mcclanahan, J. M. Shoji, R. Partch, and S. Quinn, *Solar Thermal Propulsion for Small Spacecraft,* , 1 (2004).

[54] G. Ghosh, M. Endo, and T. Iwasalu, *Temperature-Dependent Sellmeier Coefficients and Chromatic Dispersions for Some Optical Fiber Glasses,* JOURNAL OF LIGHTWAVE TECHNOLOGY **12** (AUGUST 1994), 10.2514/1.35572.

[55] Polymicro, *FLU : Low -OH SILICA / TEFLON Fibers,* (2011).

[56] J. Blue, *Ultra Low -OH SILICA Optical Fibers,* , 987650 (2014).

[57] S. Cladding and T. O. Coatings, *All Silica Fiber (Low & High OH) Anhydroguide ™ (AFS) & Superguide ™ (SFS) All Silica Fiber (Low & High OH) Anhydroguide ™ (AFS) & Superguide ™ (SFS),* , 1 (2013).

[58] C. Gmbh, *Optran ® UVWFS broadband fiber Silica / silica fibers for applications from UV-C to IR-B,* , 1 (2000).

[59] O. Ultra, *Optran Ultra,* , 0.

[60] C. Wolff, *Parabolic Antenna,* (2018).

[61] S. Ilsen, J. Kuiper, G. Pont, N. Roos, T. Note, and S. D. List, *System Requirements Document - Manned Mission to the Moon,* (2004).

[62] H. J. R. Rohsenow, Warren M. and Y. I. Cho, *Handbook of Heat Transfer*, Vol. 99 (2008) pp. 8–9.

[63] P. M. Teertstra, M. M. Yovanovich, and J. R. Culham, *Conduction Shape Factor Models for Hollow Cylinders with Nonuniform Gap Spacing,* Journal of Thermophysics and Heat Transfer **23**, 28 (2009).

[64] O. Jaramillo, J. Del Río, and G. Huelsz, *Thermal study of optical fibres transmitting concentrated solar energy,* Journal of Physics D: Applied Physics **32** (1999), 10.1088/0022-3727/32/9/310.

[65] S. R and H. J R, *Thermal Radiation Heat Transfer,* New York: McGraw-Hill (1981).

[66] S. A W, *Solar Energy,* (1968).

[67] R. Ferreira, *Development and Testing of a Water Microresistojet*, Ph.D. thesis, delft University of Technology (2008).

[68] N. R. E. L. (NREL), *SolTrace,* `https://www.nrel.gov/csp/soltrace.html` (2018), [Online; accessed 6-July-2018].

[69] P. Henshall, *Fibre Optic Solar Thermal Propulsion Technology Demonstration University of Surrey,* **44** (2006).

[70] S. A. Solovitz, *Analysis of Parallel Microchannels for Flow Control and Hot Spot Cooling,* Journal of Thermal Science and Engineering Applications **5**, 041007 (2013).

[71] R. Poyck, *Design, manufacturing and characterisation of a water fed CubeSat micro-resistojet*, Ph.D. thesis, Delft University of Technology.

[72] M. Starczewski, *Non-circular pressure vessels,* .

[73] D. Gill, *Professor Dr. Eberhard Gill Chair of Space Systems Engineering (SSE)*, Tech. Rep. 4 (Delft University of Technology, 2015).